TURBULENT FLOWS OVER MACRO–SCALE ROUGHNESS ELEMENTS – FROM BIOFOULING BARNACLES TO URBAN CANOPIES

by

Jasim Sadique

A dissertation submitted to The Johns Hopkins University in conformity with the requirements for the degree of Doctor of Philosophy.

Baltimore, Maryland

June, 2016

Abstract

Turbulent boundary layers developing over rough surfaces are frequently encountered in a variety of engineering and geophysical applications. Accurate modeling of boundary layer flow over such rough surfaces remains a challenge; direct numerical simulation (DNS) and wall-resolved large-eddy simulation (LES) are both computationally prohibitive in most cases. In this research a simulation methodology is employed, which uses an integral wall model coupled with a sharp-interface immersed boundary method and a modified rescale/recycle method, to conduct LES of developing turbulent boundary layer flows over surfaces with macro-scale roughness elements. The goal of this study is to develop and enhance our understanding of the effect of the roughness element geometry and arrangement on the mean flow response. The modeling effort is focused on two applications: (1) analysis of the effect of macro-biofouling, specifically acorn barnacles, on ship hulls and (2) study of flow over arrays of cuboidal roughness elements of various aspect ratios and arrangements. Such geometries are often used to explore the effect of atmospheric boundary layers over urban canopies. In addition to performing and analyzing wall-modeled large-eddy simulations of these flows, the re-

ABSTRACT

search also delves into the development of phenomenological models for predicting the drag over such rough surfaces. For many practical problems involving rough surface boundary layer flows, flow simulations might not be feasible. Furthermore, in many practical situations, the primary interest is in predicting gross quantities like drag and not the details of the flow. For these reasons, simpler models and correlations which can predict the effect of the rough surface on the flow are highly attractive. In the current thesis, physics based phenomenological "sheltering" models are extended to high aspect-ratio rectangular–prism roughness elements and an attempt is also made to extend it for more general rough surfaces. These models can predict the drag and aerodynamic features on surfaces with canonical surface roughness elements in the order of 10^0 to 10^2 seconds depending on the surface complexity, and their predictions compare fairly well against the data from existing experiments and simulations and also from the present LES computations.

Advisors: Professor Rajat Mittal, Professor Charles Meneveau

Reader: Professor Michael Schultz

Acknowledgments

I would like to first and foremost thank my advisors, Professors Rajat Mittal and Charles Meneveau, for all the opportunities provided to me during my time at Hopkins. Their guidance, enthusiasm and scientific curiosity have been integral in the successful completion of this thesis. It has been a privilege to take part in discussions and to work with them.

I thank Professor Mike Schultz for insightful discussions and for providing the barnacle specimen scans used in the study. I also thank him for serving on the thesis committee and for his helpful suggestions and thorough review of the thesis.

I would like to acknowledge the Office of Naval Research for funding the work that is part of this research through the ONR grant N00014-12-1-0582. The computational resources for the simulations were provided by the Department of Defense High Performance Computing Modernization Program including the ONR Pathfinder award, NSF XSEDE and JHU's HHPC and MARCC clusters.

Xiang has been the best person I could have asked for to work with me on this research. He has been an amazing source of scientific discussion and also provider of

great help and support both in research and outside of it. I thank Jung-Hee and Vijay for their help in navigating the intricacies of Vicar3D and in battling the dreaded NaNs and segfaults that are the bane of all computational research. I also thank all members of both the Flow Physics and Computation Lab and the Turbulence Research Group, for their help and discussions which have enriched my time here.

Life during PhD can be somewhat of a strange existence and one's friends are truly what keeps one sane. I would like to thank Parastou for being an absolutely amazing friend and a ray of light during some fairly stormy days. Leen, I thank, for her long distance phone based support and for letting me indulge in, and also for enthusiastically partaking in the *'life is a silly thing'* motif. I also thank all my friends old and new, both here at Hopkins and outside, for all the cherished moments.

Mike and other staff members of the Mechanical Engineering Department have been truly excellent in smoothing out and making easy much of the usually odious bureaucratic and administrative procedures.

I would also like to thank all the professors and teachers who have imparted their knowledge and wisdom that I shall always carry with me.

Of course none of this would have been possible without my parents and sister, who have been a source of continuous strength and support. I offer my sincere gratitude to them for always believing in me. I also would like to thank the bevy of aunts and uncles, and gaggle of cousins who are truly the best family one could ask for.

To Ummama and Roshakkakka, and the memories of light and laughter ...

"We, who are formed by little scraps of wisdom."

Contents

Abstract **ii**

Acknowledgments **iv**

List of Tables **xii**

List of Figures **xiv**

1 Introduction **1**

1.1 Rough Wall Boundary Layers 1

1.1.1 Aerodynamic and Geometric Parameters 3

1.1.2 Relating the Rough Wall Morphology to the Flow Response . 7

1.2 Biofouling of Marine Vessels 10

1.3 Neutral Atmospheric Boundary Layer over Urban Canopies 12

1.4 Scientific Objectives and Thesis Outline 14

2 Methodology **18**

2.1 Large–eddy Simulations of Turbulent Boundary Layers over Macro–Scale Roughness Elements 19

2.1.1 The Sharp–Interface Immersed Boundary Method 23

2.1.2 The Integral Wall Model 25

2.1.3 Rescale–Recycle Method for Inflow Generation 30

2.2 An Analytical Model for Predicting the Aerodynamic Properties . . . 32

2.3 Summary 38

3 Boundary Layer Flow over Surface Mounted Acorn Barnacles and Idealized Barnacle Models 39

3.1 Simulations of Flow over Individual Attached Barnacles 39

3.1.1 Barnacle Geometry 42

3.1.2 Solution Setup 47

3.1.3 Grid Refinement 49

3.1.4 Results and Discussion 50

3.1.4.1 Instantaneous Flow Field and Vortex Structures . . . 51

3.1.4.2 Flow and Wake Statistics 56

3.1.4.3 Drag and Lift Forces 59

3.2 Large–Eddy Simulations of Flow over Idealized Barnacle Arrays . . . 62

3.2.1 Simulation Setup 65

3.2.2 Instantaneous and Mean Flow Field 66

3.2.2.1 Velocity Profile within the Canopy 68

3.2.2.2 Aerodynamic Parameters 70

3.3 Summary 72

4 Mean Flow Response to Idealized Urban Canopies 74

4.1 Simulation Setup 75

4.2 Mean Flow within and above the Roughness Layer 79

4.3 Volumetric Sheltering and Analytical Model 85

4.4 Model predictions and Comparisons with Simulation Data 89

4.5 Summary 100

5 An Explicit Analytical Roughness Model for Surfaces with Cuboidal Roughness Elements 103

5.1 A Simplified Approach Relating Flow Parameters to Roughness Morphology 104

5.2 Application to Cubic Rough Surfaces in Various Arrangements 110

5.2.1 Aligned Cubes 110

5.2.2 Fully Staggered arrangement 118

5.2.3 Percent Stagger 122

5.2.4 Orientation 126

5.3 Collapse of Data from Different Cases 128

5.4 Predictions of Friction Velocity u_τ and Canopy Height Velocity U_h . . 130

5.5 Summary 133

6 Thesis Summary **135**

Appendix A A Generalized Shading Model for Macro–Scale Roughness Elements **140**

A.1 Calculation of Geometric and Aerodynamic Parameters 141

A.2 Generalized Shading Model 143

A.3 Comparison of the Equivalent h_s Method to the Full Integration Approach 151

A.3.1 Aligned and Staggered Cubes 151

A.3.2 Arrangements with a Percent Stagger 153

A.3.3 Roughness Element Orientation 154

A.4 LEGO Block Roughened Surfaces 156

A.5 Application to Idealized Biofouled Surfaces 161

A.6 Predicting Drag on Urban Geometries 163

A.7 Summary 166

Appendix B Validation of The General Shading Model **168**

B.1 Aligned and Staggered Cubes 169

B.2 Percent Stagger Arrangement of Cubes 173

B.3 Rectangular Prism – Aligned, Staggered and Percent Stagger Arrangements 173

Appendix C Derivation of Geometric Parameters for a Staggered Ar-

rangement **176**

Appendix D A Techno–Economic Analysis of Biofouling **182**

Appendix E Tabulation of geometric factors **188**

Bibliography **193**

Vita **215**

List of Tables

3.1 Table 1. Measurements from the scanned specimens 46
3.2 Comparison of average drag and lift coefficients for models S and R on two grids. 51
3.3 Location of the significant points for all the cases 56
3.4 Comparison of force coefficients, the Strouhal number, kinetic energy and its production in the near wake region for the cases simulated. . . 60
3.5 The various cases simulated for the idealized barnacle fouled surfaces. 64
3.6 Tabulation of the mean flow response for the cases simulated. 71

4.1 The five sets of cases simulated. AR is the aspect–ratio and stg is the percentage stagger varying between 0 (fully aligned) and 100 (fully staggered). Each set has N cases. ($^{\#}$) The first and last case in LP06PXX–AR2 are the same as LP06A-AR2 and LP06S-AR2 77
4.2 Aerodynamic parameters determined for the four sets of cases with varying aspect ratio. 82
4.3 Aerodynamic parameters for the case of LP06P. 84

A.1 The two sets of cases for the LEGO blocks from Placidi and Ganapatisubramani.[32] CASELF has a constant $\lambda_p = 0.27$ and CASELP has constant $\lambda_f = 0.15$. 157
A.2 Comparison of the data from the model to the fitted LES data. . . . 166

B.1 Comparison of results on various grids for the case of an aligned cubes with $\lambda_f = 0.25$. 171
B.2 The differences between the aerodynamic parameters calculated at each grid with the result from an analytical calculation. 171

D.1 Parameters for the DDG–51 class destroyer. 184
D.2 Estimations of the optimal cleaning time for the two type of assumed biofouling growth rates – linear and logistic 187

E.1 K_G as a function of K_a and compared with a from iterative solution. The superscripts denote the order of correction used for G. $K_G < 0.4$ should be clipped to 0.4 when used in calculations. 190
E.2 K_G and Λ_f as a function of λ_f for aligned cubes. $K_G < 0.4$ clipped to 0.4 when used in calculations. These values are calculated assuming a second order form for G. 191
E.3 K_G and Λ_f as a function of λ_f for staggered cubes. $K_G < 0.4$ clipped to 0.4 when used in calculations. These values are calculated assuming a second order form for G. 192

List of Figures

1.1 Examples of rough surfaces (a) a cut–view of a brass pipe with corrosion,[11] (b) a propeller with cavitation damage,[12] (c) a water–turbine eroded by volcanic ash,[13] (d) a wind–farm situated in a complex terrain,[14] (e) the city of Baltimore[15] – all images are from *Wikimedia Commons*. 2

1.2 Example sketch of the log–law prediction for a fully rough regime along with an observed velocity profile, illustrating both the log region and the deviation due to the outer layer dynamics. 5

1.3 Some geometric parameters of the rough wall. 6

1.4 Sketch showing variation of (a) z_o and (b) d as a function of the frontal area ratio for aligned cubes. 7

1.5 (a) Nauplius larval stage of the barnacle *Elminius modestus*[71] (b) Adult *Chthamalus stellatus* barnacles settled on a surface[72] (c) Bio-fouled hull and propeller of a ship covered with acorn barnacles[73] - (a) and (b) are from *Wikimedia Commons* while (c) is from the archives of the Woods Hole Oceanographic Institute. 12

2.1 Sketch showing the cells used for the sharp–interface immersed boundary method. 23

2.2 A schematic illustrating the integral wall model 26

2.3 Sketches illustrating (a) projection of the immersed boundary area to the cells faces in x and y directions, S_x on face $F1$ and S_y on face $F2$. (b) projection of wall stress τ_w onto components on the cell face $F1$ for implementing the boundary condition. 28

2.4 An illustration of the rescale–recycling method for rough wall boundary layers. 31

2.5 An illustration of the 2–layer canopy model. 33

2.6 Illustration of the (a) volumetric sheltering and shading for (b) aligned (side view) and (c) staggered (top view) arrangements. (d) is equivalent shaded height for a staggered arrangement. 35

3.1 (a) $B1$ and (b) $B2$ are the acorn barnacle geometries used in this study. (c)$B2M$ is a modified barnacle created from $B2$ by removing the protrusion (d) is a top view comparing the base of the barnacle geometries $B1$ and $B2$ along with a superimposed circle (dashed black line). 43
3.2 (a) acorn barnacle specimens collected (b) zoomed in view of a barnacle (c) 3D scans and (d) simplified shape (S) generated. (e) convex hull fitted to the slice at a plane. (f) ridge–depth calculated as the the radial difference between the convex hull and the barnacle surface. (f) cross section of the generated object R incorporating the ridges. . . . 45
3.3 The two simplified representations (a) the smooth frustum S and (b) the frustum with ridges R. 45
3.4 The domain and the boundary conditions used in the simulations. . . 48
3.5 (a) Side and (b) top view of the mesh for GRID1 illustrating the resolution present around the object. (c) and (d) correspond to those for GRID2. 48
3.6 Contours of instantaneous Vortex structures generated behind the objects for the five objects. 52
3.7 Contours of instantaneous ω_z at the mid plane. 53
3.8 Contours of instantaneous ω_y at a location $y/D_1 = 0.32$ 54
3.9 Spectra of the probe velocity for all the cases simulated at a location $x/D_1 = 1.5$ and $y/D_1 = 0.35$ 55
3.10 Mean streamlines in the XY center plane (a-e) and the base (f-j) . . 57
3.11 Contours of k in the XY center plane for the different cases simulated. 58
3.12 Spectra of the lift coefficient for S, R, $B1$, $B2$ and $B2M$, illustrating the peaks in the frequency response 61
3.13 The aligned and staggered arrangement of the idealized barnacles (cases BLP05A ans BLP05S). The repeating tile is shown in light gray with a thick dashed border. 63
3.14 The simulation domain along with the boundary conditions and the $256 \times 64 \times 64$ grid (every other grid point is shown). The rough surface shown is an aligned array of $\lambda_f = 0.02$ (BLP05A) 64
3.15 Instantaneous contours of streamwise velocity for BLP05A and BLP20A at $z/h = 0.625$ 66
3.16 Time averaged U velocity contours for BLP20A and BLP20S at $z/h = 0.625$ 67
3.17 Time averaged streamlines at the mid plane for BLP20A and BLP05A cases. 68

3.18 (a) Spatio–temporal averaged streamwise velocity profile in the rough layer for all the cases along with the exponential fit and (b) the corresponding linear–log plot of the canopy averaged velocity for all the frustum array cases. 68
3.19 Log–linear plot of the mean velocity profile non-dimensionalized with the fitted u_τ and plotted against $(z-d)/z_o$ with model predicted d and fitted z_o for all the cases. Also shown is the log–law prediction using the dotted line. 70

4.1 (a) shows the roughness element with base width w and height h. The arrangement of the elements are visualized using a top view of the repetitive tile. Panels (b) for case LP06A, (c) for case LP11A, (d) for case LP25A display aligned arrangements with different values of λ_p, 0.06, 0.11 and 0.25 respectively while (e) is for the case of LP06S, a fully staggered arrangement with $\lambda_p = 0.06$. Panel (f) shows one particular case of a percentage staggered arrangement ($stg = 38$). . . 76
4.2 Instantaneous iso-surfaces of streamwise velocity inside the roughness layer for LP11A–AR4, ($\lambda_p = 0.11, h = 4w$). The iso-surfaces shown corresponds to $u/U_o \leq 0.26$. 78
4.3 Temporal, spanwise and streamwise averaged velocity profiles for (a) LP06A (b) LP11A (c) LP25A (d) LP06S. (e)-(h) show the corresponding profiles shifted by h and plotted in log–scale. 80
4.4 Simulation results for percentage stagger case LP06P – (a) Temporal, spanwise and streamwise averaged velocity profiles and (b) Canopy height velocity for the different percentage stagger (stg). 83
4.5 Time averaged streamwise velocity contours for the cases of LP06P at a wall normal distance $z/w = 1.625$ at different percentage of staggering. (a) stg = 0 % (aligned), (b) stg = 50 % and (c) stg = 100 % (fully staggered). 83
4.6 Contour plot of streamwise velocity for the case of (a) LP06S-AR6 at $z/w = 0.98$ and (b) for the case of a self similar plane wake. The black lines are the contour levels corresponding to 0.2 and 0.3 times the mean free-stream velocity. The white dashed lines show the linear projections of the simplified shaded region. 87
4.7 The modified sheltering volume for high aspect–ratio elements. 88
4.8 Model predictions of roughness length z_0, displacement height d and relative height $h - d$ for various aspect–ratios ($AR = h/w$) for an aligned arrangement, with $\lambda_p = 0.11$. 90
4.9 Schematic showing the sheltered (dashed) and effectively exposed (dark) frontal area of a roughness element with increasing aspect–ratio, for a surface with aligned elements and a given moderate to high λ_p for which sheltering is important. 91

4.10 (a) Contour map of model z_o prediction as function of λ_p and aspect–ratio for an aligned arrangement of rectangular prism elements. (b) Various horizontal slices from (a) are extracted to better illustrate the variation of z_o with respect to aspect–ratio. Each line corresponds to a different value of the aspect–ratio. (c) Variation of z_o as a function of λ_f for various aspect–ratios. (d) Plan area density at which z_o peaks, λ_p^m as a function of the aspect–ratio. 92
4.11 Log-linear plot of the mean velocity profiles from LES (symbols), normalized with the fitted value of u_τ so all fits (dashed lines) have the same slope of $1/\kappa$. The line's x-intercept ($U/u_\tau = 0$) is $(z_o - d)/w$ using the fitted value of z_o. Profiles are shown for 4 sets at various aspect–ratios: (a) LP06A (b)LP11A (c)LP25A (d)LP06S and also for the $AR = 2$ case for various staggering ratios, shown in (e) case LP06P. 95
4.12 Comparison of z_o between the LES and the model for (a) LP06A, (b) LP11A and (c) LP25A. Symbols are the LES data and the lines are the model predictions. 96
4.13 u_τ comparison – simulation (symbols) and model predictions (lines) for (a)LP06A (b)LP11A and (c)LP25A. (d)-(f) are the corresponding plots for U_h. 97
4.14 comparison between simulation (symbols) and model prediction (line) for LP06S (a)z_o (b)u_τ and (c)U_h. 98
4.15 comparison between simulation and model for LP06P (a)z_o (b)u_τ and (c)U_h. Results of z_o for $AR = 1$ case also plotted for comparison.[142] . 99

5.1 Top view showing the arrangement of roughness elements and side view showing a simple representation of the reduced momentum region. h_s is the height of the sheltered layer 105
5.2 Illustration of repeating tile for an aligned arrangement with a frontal area ratio λ_f and the volumetric shading for this arrangement 111
5.3 Comparison for the fully aligned case of (a) z_o and (b) d predictions from the full iterative solution against measured values from experiments and simulations. 112
5.4 Comparison for the fully aligned case of (a) z_o and (b) d predictions from the full iterative solution with the β correction included against measured values from experiments and simulations. 113
5.5 (a) Comparison of Predictions from the full iterative solution compared against various corrections $a = K_a G$. (b) Comparison of the different forms of the factor G 114
5.6 Comparison for the fully aligned case of (a) z_o from the full iterative solution against predictions from explicit corrections. (b) a measure of the relative difference in the predicted z_o using the correction as opposed to the full iterative solution. 116

5.7 Illustration of the volumetric sheltering for a fully staggered arrangement (a) only spanwise sheltering (b) streamwise sheltering also present when the elements are close. 119
5.8 Comparison for the fully staggered case of (a) z_o from the full iterative solution against predictions from explicit corrections. (b) a measure of the relative error in using the correction as opposed to the full iterative solution. 121
5.9 Comparison for the fully staggered case without clipping of K_G (a) z_o from the full iterative solution against predictions from explicit corrections. (b) a measure of the relative error in using the correction as opposed to the full iterative solution. 121
5.10 Illustration of a percentage stagger arrangement. $stg = 0, \zeta = 0$ is an aligned arrangement and $stg = 100, \zeta = 1$ is a fully staggered arrangement 122
5.11 Variation of $C(\zeta)$ as a function of the percent stagger ζ. 122
5.12 Comparison of (a) z_o and (b) d predictions from the full iterative solution against measured values from experiments and simulations for roughness elements of various percent stagger with $\lambda_f = 0.06$ and 0.11. 123
5.13 Comparison of z_o from the full iterative solution against predictions from explicit corrections for λ_f = (a) 0.06 and (b) 0.11. measure of the relative error in using the correction as opposed to the full iterative solution for λ_f = (c) 0.06 and (d) 0.11. 124
5.14 Illustration of the volumetric sheltering for an aligned arrangement of cubes with orientation α. 125
5.15 Comparison of (a) z_o and (b) d predictions from the full iterative solution against measured values from experiments and simulations for roughness elements of various orientation aligned arrangement with $\lambda_f = 0.06$ and 0.11. 125
5.16 Comparison of z_o from the full iterative solution against predictions from explicit corrections for λ_f^0 = (a) 0.06 and (b) 0.11. measure of the relative error in using the correction as opposed to the full iterative solution for λ_f = (c) 0.06 and (d) 0.11. 127
5.17 Comparison of (a) z_o/h, (b) d/h (c) $z_o/(h-d)$ for different arrangements from LES data[63] 129
5.18 The LES data plotted as function of the geometric parameters and compared against the derived formula for (a) $z_o/(h-d)$ and (b) d/h. 130
5.19 The model predictions for the friction velocity compared against the LES data for (a) aligned and (b) staggered arrangement of cubes while (c) and (d) are the corresponding canopy height velocity for the two arrangements. 132
5.20 Comparison of the effect of the different terms on the friction velocity for (a) aligned and (b) staggered arrangements. 133

A.1 (a) an example of a surface with a random arrangement of roughness elements. (b) illustration of the frontal area A_f and (c) the sectional area $dA_f(z)$. 141
A.2 Dividing the surface into (a) emitter (S_e) and (b) receptor (S_r) Surfaces. (c) is the volumetric shading generated by S_e while (d) is the illustration of a shaded area. 144
A.3 (a) The creation of an elemental edge corresponding to a point P_e. (b) The edge length l_b associated with the point P_b. 145
A.4 (a) Side and (b) Top view of the projection and sweep method to generate the height of the shading volume corresponding to an edge l_b. (c) The top view showing the height of the shading volume for one edge S^b_{sh}. (d) The height of the shading volume for the full surface. The edges used to generate this area are given by the white hatched region. For (c) and (d) the color indicates the height of the shading volume. 146
A.5 Illustration of the shaded height for a cylindrical roughness element. . 148
A.6 Sketch of (a) an example shaded area predicted by the model $H_s h(x, y)$ for staggered cubes and (b) the "equivalent" spanwise constant height shaded area of height h_s. 148
A.7 Example input surfaces $H(x, y)$ for the aligned and staggered case. . . 151
A.8 Comparison of (a) z_o and d for aligned arrangements, obtained from the numerical model via the two methods and also compared against measurements from literature. 152
A.9 Comparison of (a) z_o and d for staggered arrangements, obtained from the numerical model via the two methods and also compared against measurements from literature. 153
A.10 Model comparisons against LES (a) for percent stagger and (b) for roughness element orientation. The points are LES from Ref 142, the solid lines are the A_s method while the dashed lines are the h_s method. 154
A.11 (a) Top view of an example input surface to the model, with the cubic roughness element at an angle ($\alpha = \pi/4$)to the flow. The associated height of the sheltering volume is also shown. (b) Model comparisons against LES for roughness element orientation. The points are LES from Ref 142, the solid lines are the A_s method while the dashed lines are the h_s method. α is plotted in degrees. 155
A.12 LEGO block arrangement for (a)CASELF and (b) CASELP. The flow is from left to right. 156
A.13 The details of the geometry used (a)The LEGO block and (b) RECT geometry obtained by removing the top protrusion from (a). 157
A.14 The model predicted sheltering volume for the CASELF illustrated using contours of the height of the sheltering volume. 158

A.15 The model predicted sheltering volume for the CASELP illustrated using contours of the height of the sheltering volume. 159
A.16 Comparison of (a) z_o (b) d and (c) u_τ for CASELF arrangements. . . 160
A.17 Comparison of (a) z_o (b) d and (c) u_τ for CASELP arrangements. . . 161
A.18 Comparison of (a) z_o (b) u_τ and (c) U_h for the idealized barnacle fouled surfaces. 162
A.19 The region surrounding the *Sperrstrasse* urban canyon in Basel. The region of interest is highlighted. 163
A.20 (a) The converted data–set in the form of $h(x, y)$ which is the input to the shading model. (b) Top view indicating the two wind directions tested – W1 and W2. The coloring is the building height. The grid used has a resolution of 1m in the x and y directions. 164
A.21 The predicted shading colored by the height of the shading volume for (a) W1 and (b) W2 directions. 165
A.22 The LES profiles from Giometto et.al.[83] non-dimensionalized and plotted in log–linear profile using the fitted data. 166

B.1 The top view showing the sheltering region for (a) an aligned and (b) staggered arrangement. The colors indicate the height of the sheltering region. (c) and (d) shows the corresponding sheltered area on the cubes. 169
B.2 z_o prediction for aligned and staggered cubes compared between the analytical model and the general shading model. 170
B.3 Variation of the computation time as a function of the grid size N plotted on a log–log scale. 172
B.4 Comparison of z_o for a percent stagger arrangement of cubes for predictions from the generalized model (solid lines), the analytical model (dashed lines) and the LES (points). 172
B.5 The predicted z_o for aligned arrangement of rectangular–prisms at various aspect–ratios compared between the generalized model (points) and the analytical version (solid lines). 173
B.6 The predicted z_o for two values of λ_f with various values of percent stagger the five sets of cases from Chapter 4. The points are LES results while the solid lines are the predictions from the generalized shading model and the dashed lines those from the analytical model. 174

C.1 Streamwise and spanwise sheltering for a staggered arrangement. (a) Top view of spanwise and streamwise sheltering (b) side view of spanwise sheltering and (c) side view of streamwise sheltering. 177
C.2 Sheltered region on a cube in staggered arrangement and conversion into an equivalent 1D shaded height h_s. 177

C.3 C_ζ^{st} as a function of λ_f for the staggered arrangement. Also shown in the analytical form derived for the high λ_f case. 180
C.4 (a) z_o and (b) d compared for the case of staggered arrangement using a constant C_ζ^{st} and a C_ζ^{st} that varies as a function of λ_f. They are also compared against experimental and simulation results from literature. 181

D.1 The assumed growth of biofouling on the ship hull as (a) linear and (b) logistic curve and the associated drag increase on the surface. . . 185
D.2 The DDG–51 class destroyer of the US Navy (`http://www.navy.mil/management/photodb/photos/030313-N-0115R-077.jpg`) 186
D.3 The costs of biofouling and the optimal cleaning time predicted by the (a) linear and (b) logistic growth curve. 186

Chapter 1

Introduction

1.1 Rough Wall Boundary Layers

Rough wall turbulent boundary layers are ubiquitous in both engineering and geophysical applications – most surfaces of fluid dynamic interest are inherently rough. These include flow through pipes and channels which become rough due to corrosion/pitting,[1,2] propeller blades that undergo cavitation,[3,4] ship–hulls roughened by attached micro– and macro–organisms,[5,6] atmospheric boundary layer flows over complex terrains,[7,8] vegetative[9] and urban canopies[10] etc. Figure 1.1 shows examples of such surfaces. Turbulent flow over rough walls thus have applications in areas as diverse as chemical transport, heat exchangers, turbine blades, wind–farms, numerical weather prediction, etc. Due to the importance and prevalence of such flows, they

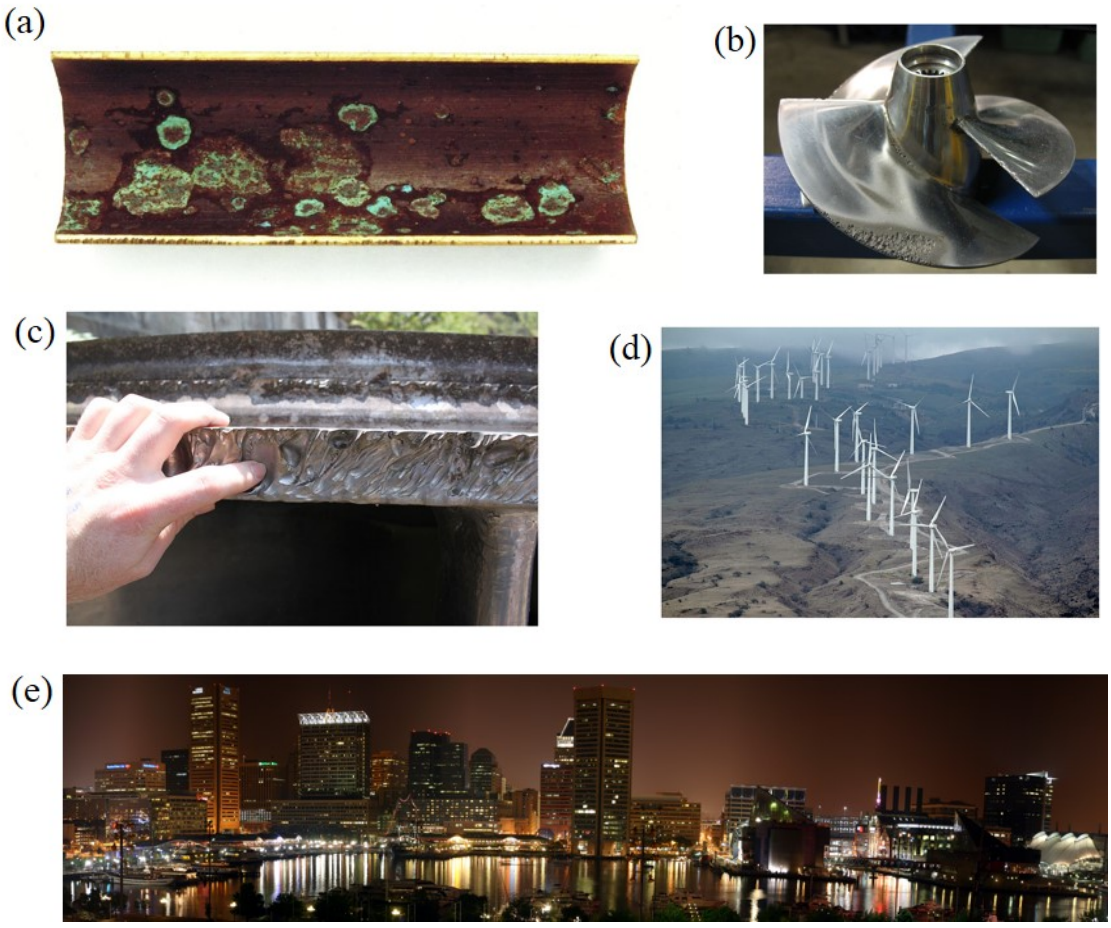

Figure 1.1: Examples of rough surfaces (a) a cut–view of a brass pipe with corrosion,[11] (b) a propeller with cavitation damage,[12] (c) a water–turbine eroded by volcanic ash,[13] (d) a wind–farm situated in a complex terrain,[14] (e) the city of Baltimore[15] – all images are from *Wikimedia Commons*.

have been studied extensively, and in particular, considerable work has been done in the past to investigate the effect of surface roughness on the boundary layer flow and the correlation between roughness topology and surface drag.

1.1.1 Aerodynamic and Geometric Parameters

Some of the earliest studies on rough wall turbulence include those of Nikuradse[16] and Schlichting.[17] Nikuradse[16] studied pressure–loss in flow through pipes whose surfaces where roughened with sand grains and characterized the effect of Reynolds number and roughness height. At high values of the non–dimensional sand–grain height ($k^+ \gtrsim 70$), where k^+ is k_s, the sand–grain roughness height normalized in wall units (ν/u_τ – ν is the kinematic viscosity and u_τ is the friction velocity), he identified that the drag becomes independent of the Reynolds number and depends only on k_s. This is termed the "fully rough regime", while for lower values of k^+ he found that the Reynolds number has an effect on the drag, and this region is termed the "transitionally rough regime".

In the fully rough regime, in the inertial layer away from the roughness, the mean streamwise velocity profile follows a log–law of the form[16,18–21]

$$U^+(z) = \frac{1}{\kappa} \ln \frac{z}{k_s} + B. \tag{1.1}$$

where the superscript + denotes normalization by wall units, z is the wall normal distance, κ the von–Karman coefficient and B is the intercept (This form is also applicable for smooth walls with z^+ instead of z/k_s and the value of $B \approx 5$). The roughness length–scale is parameterized using the equivalent sandgrain roughness height (k_s). An equivalent representation is done using the hydrodynamic roughness

height (z_o),

$$U^+(z) = \frac{1}{\kappa} \ln \frac{z}{z_o}, \tag{1.2}$$

or with a velocity shift (ΔU^+) in the log law,

$$U^+ = \frac{1}{\kappa} \ln z^+ + B - \Delta U^+, \tag{1.3}$$

This representation using the velocity shift is also valid for flows that are transitionally rough. In the fully rough regime these representations are equivalent and each of these forms can be related to the other. For e.g. $k_s \approx z_o \exp(\kappa B)$.[19]

For the case of rough surfaces with macro–scale roughness elements, Eq. 1.2 is commonly used in the form

$$U^+ = \frac{1}{\kappa} \ln \frac{z-d}{z_o}, \tag{1.4}$$

where d is the zero–plane displacement which can be interpreted as the wall normal height at which the drag acts.[22] This form is used in geophysical and urban–canopy applications, while for engineering flows, the equivalent sand–grain roughness height (k_s) or velocity shift (ΔU^+) are characterizations more frequently encountered. Figure 1.2 gives a conceptual sketch of the mean velocity profile in the inertial layer. The actual velocity profile will have a deviation from the log–law in the region near $z \sim \delta$ where δ is the boundary–layer height, due to the effect of the outer–layer dynamics (e.g. intermittency and entrainment). Including this effect, the velocity profile can

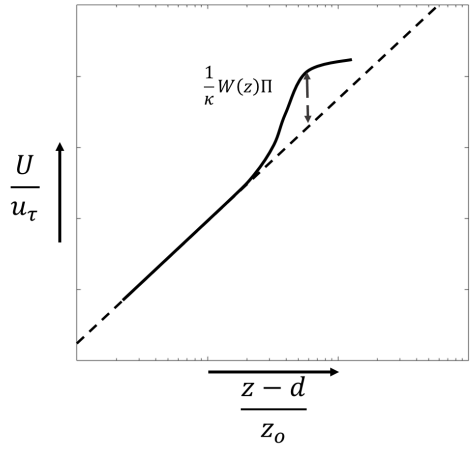

Figure 1.2: Example sketch of the log–law prediction for a fully rough regime along with an observed velocity profile, illustrating both the log region and the deviation due to the outer layer dynamics.

be expressed in the form

$$U^+ = \frac{1}{\kappa}\ln\frac{z-d}{z_o} + \frac{1}{\kappa}W(z/\delta)\Pi, \tag{1.5}$$

where the wake function $W(z/\delta)\Pi$ is used to characterize the deviation with $W(1) = 2$ and Π usually of $O(1)$.[19,23]

In the fully rough regime, these aerodynamic parameters (z_o, d, u_τ, k_s) will be independent of the Reynolds number and will depend only on the surface geometry. Conventionally, the most important rough wall morphometric parameters include the solidity, λ_f and the surface coverage density λ_p. Solidity is defined to be wind-ward projected roughness frontal area per planar area (A_f/A_T), while coverage density is the plan area of roughness element per plan area of the surface (A_p/A_T). These areas are illustrated in the sketch given in Fig. 1.3. To study the rough wall aerodynamic

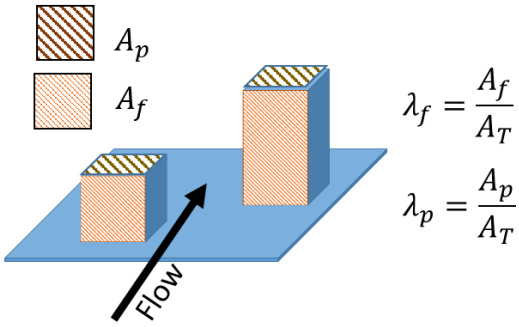

Figure 1.3: Some geometric parameters of the rough wall.

effects (the effect of λ_f, λ_p), one frequently used model is cube roughened walls,[24–26] where $\lambda_f = \lambda_p$. Flow response to varying λ_f has been studied both numerically[27–29] and experimentally.[30,31] The results from these studies have been used to classify the behavior of turbulent flow over cubic arrays as a function of the solidity. A good discussion is found in the review article by Grimmond and Oke.[10] For z_o, it has been found that for sparsely packed cubes, initially z_o increases linearly as λ_f increases; it peaks at around $\lambda_f \approx 0.2$, then decreases as λ_f further increases. At low–values of λ_f, the elements are so far apart that they do not interact with each other and an increase in λ_f leads to more roughness frontal area in a given area leading to a linear increase in drag. However as λ_f increases, the elements start interacting and "sheltering" each other, leading to a reduction in drag generated by the sheltered elements. Further increasing λ_f leads to the elements being very close to each other and much of the frontal area being sheltered, thereby leading to a regime where the drag reduces as λ_f increases. This behavior is illustrated schematically in Fig. 1.4a. The zero-plane displacement (d), meanwhile increases monotonically with λ_p and becomes equal to

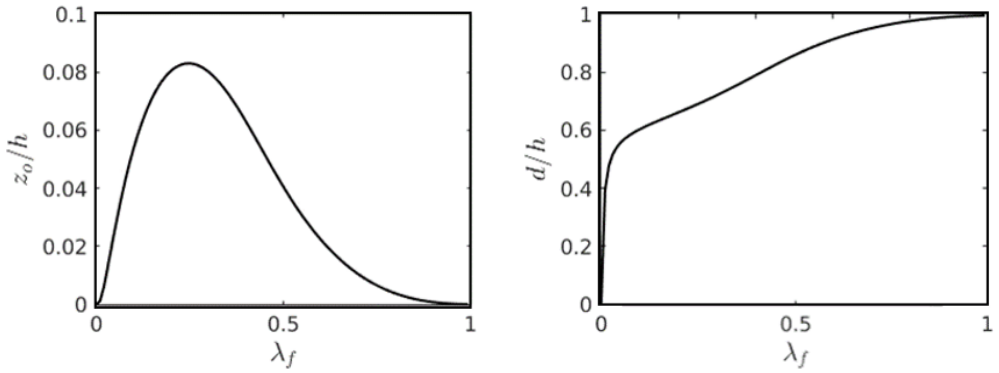

Figure 1.4: Sketch showing variation of (a) z_o and (b) d as a function of the frontal area ratio for aligned cubes.

the roughness element height (h) at $\lambda_p = 1$, which is equivalent to having a new smooth wall at height h (Fig. 1.4b).

Since cubes have $\lambda_f = \lambda_p$, to study the effects of λ_f, λ_p separately, non-cubic roughness elements need to be used. Recently such a study has been carried out by considering arrangements of LEGO blocks in various configurations[32] with $\lambda_f \leq 1.36\lambda_p$.

1.1.2 Relating the Rough Wall Morphology to the Flow Response

An important aspect of understanding turbulent boundary layer flow over rough walls has been to relate the frictional drag on a surface to the roughness geometry. Early efforts include work by Schlichting,[17] who studied surfaces with spherical and conical elements of various packing densities, and Colebrook[33] who investigated transitional and fully rough flows in pipes. This eventually formed the basis for the Moody dia-

gram,[34] which is a widely used tool in engineering design to estimate the pressure loss produced by a rough surface. It should be noted that use of this diagram requires the a-priori knowledge of k_s for a surface. Estimations of the effective length–scale of the roughness is very important both for engineering design and for various applications; an example would be to predict turbine performance degradation in the presence of blade roughness.[35] Another application is in simulations of flow over complex rough surfaces of engineering or geophysical interest, which due to computational cost constraints, require the roughness and the associated near wall effects to be modeled, rather than explicitly resolved. Many such wall modeled approaches require the specification of a roughness length scale.[36–38] The roughness length scale is also used in many engineering models. For example, ones used to predict wind–farm performance in complex terrain require specifications of the roughness length of the terrain.[39–41]

There has been significant effort in the past to investigate correlations of the roughness length scale to the roughness geometry. Thorough reviews of such correlations are found in review articles in the literature.[10,42,43] Many approaches correlate the velocity shift (ΔU^+) or the roughness length–scale to parameters quantifying the solidity and shape of the roughness elements.[44–53] More complex approaches include the use of surface statistics, for example the statistical moments of the surface height distribution,[54] the effective slope[55,56] and the skewness factor[42] to estimate the effective roughness height. Another approach is the so-called "canopy–model" technique where the effect of roughness elements is modeled as a distributed drag force[9,57] and

the spatio–temporal averaged velocity profile is solved for aerodynamic properties of the rough walls.[52,58–60]

Although the past research on rough wall boundary layers is quite extensive, recent new capabilities to perform extensive large-eddy simulations, efficiently provide new opportunities to carry–out detailed analysis on various aspects of the rough surface morphology. These include the effect of various roughness element shapes, arrangements and aspect–ratios (defined as the ratio of the height to the spanwise edge length of the roughness element). Such a study will be useful in developing more accurate physics based practical models for estimating the drag associated with such surfaces. Such an analysis would enable us to enhance our understanding of the effect of geometry and surface morphology on the mean flow properties. The focus of this thesis is then to investigate the mean flow response in the presence of macro–scale roughness elements and to characterize the aerodynamic properties of such rough surfaces as a function of the surface geometry. Detailed investigations are carried out on the effect of roughness–element aspect–ratio, the packing density and also arrangement topology of the roughness elements using numerical simulations, details of which are given in the next chapter in Sec. 2.1. The methodology is based on a sharp–interface immersed boundary method[61,62] combined with an integral wall–model.[38] Along with these large–scale simulations, extensions are also developed for engineering models that enable predictions of the aerodynamic parameters given only the rough surface morphology. This approach is extended from a recently developed

analytical model,[63] whose details will also be presented in the next chapter in Sec. 2.2. The results of this study may in principle be broadly applicable to many types of rough wall boundary layer flows, but in this thesis, the focus will be on two applications in particular – (a) turbulent boundary layer flows over idealized biofouled surfaces and (b) neutral atmospheric boundary layer flow over urban canopies. The former is an example of an engineering application while the latter is a geophysical problem. In the following sections, brief descriptions will be given regarding both of these applications.

1.2 Biofouling of Marine Vessels

Biofouling is the accumulation of micro-organisms, plants, algae, or animals like barnacles, and mussels on wetted surfaces. Exact estimates are hard to come by, but studies indicate that the economic impact of biofouling on the maritime industry runs in the billions of dollars annually, and it is also a costly problem for the US Navy.[64,65] This expenditure is mostly associated with additional fuel costs resulting from increased drag on hulls of oceangoing vessels as well as the cost of remediation and cleaning of biofouling. There are various strategies employed to combat biofouling on surfaces – including chemical treatment, surface micro–structures that discourage initial bio–film formation etc. This thesis considers the problem of predicting drag on surfaces that are already fouled by agents like barnacles and utilizes such predictions to aid in developing remedial strategies.

Among the various biological organisms implicated in biofouling, acorn barnacles are a major agent of hard or calcerous biofouling. Acorn barnacles start out as a larval stage known as nauplius, which evolves into the cyprid larva, which is the last larval stage.[66,67] In this stage it is freely swimming and seeks out suitable surfaces for eventual settlement. Once a suitable site is identified, the organism attaches to the substrate and cements itself to the surface.[68,69] The cyprid then undergoes metamorphosis to become a juvenile barnacle. The barnacle surrounds itself with hard calcified plates as it grows. The attachment strengths of these barnacles are very high,[70] and the calcerous plates remain attached to the hull, resulting in increased drag, even after the barnacle ceases to live. Fig. 1.5 shows examples of the larval and adult stage of different acorn barnacle species and also an example of a barnacle fouled ship hull and propeller.

In this thesis, computational studies on both the detailed flow over individual barnacle geometries (Sec. 3.1) and also flow over arrays of idealized barnacles (Sec. 3.2), which represent an idealized biofouled surface, will be carried out. A predictive model will also be developed for the drag produced by these idealized biofouled surfaces (Sec. A.5). Using the results from phenomenological models, an example techno–economic analysis will also be demonstrated, which can identify the optimal cleaning strategy (specifically, the frequency of cleaning) for biofouled ships.

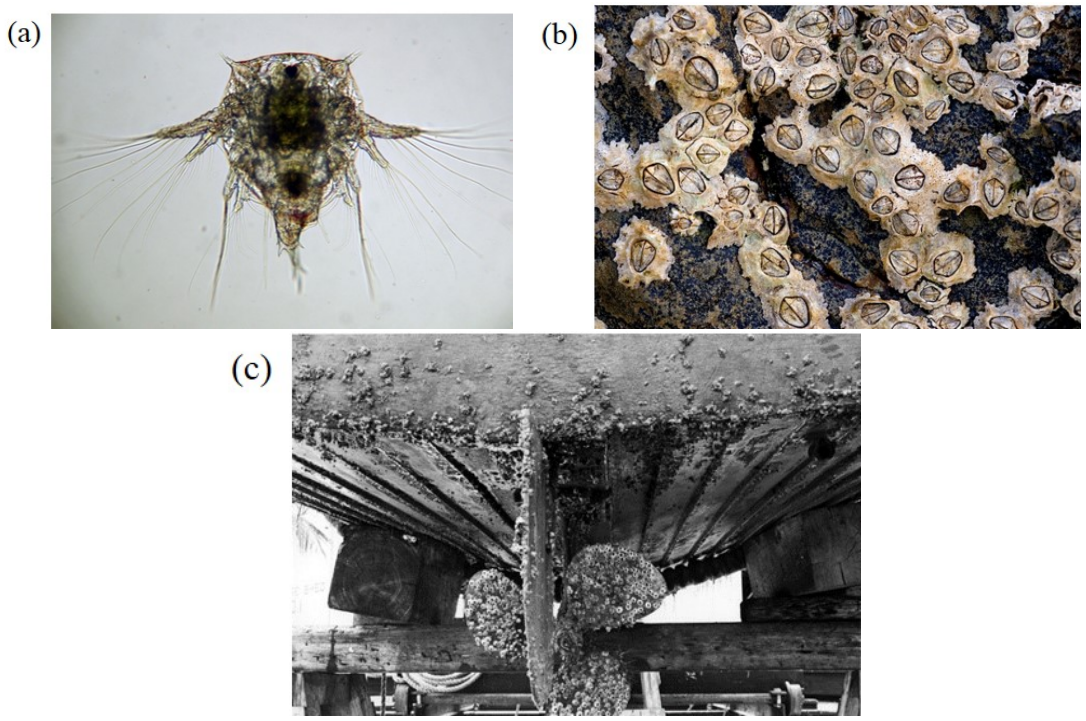

Figure 1.5: (a) Nauplius larval stage of the barnacle *Elminius modestus*[71] (b) Adult *Chthamalus stellatus* barnacles settled on a surface[72] (c) Bio-fouled hull and propeller of a ship covered with acorn barnacles[73] - (a) and (b) are from *Wikimedia Commons* while (c) is from the archives of the Woods Hole Oceanographic Institute.

1.3 Neutral Atmospheric Boundary Layer over Urban Canopies

Flow over urban canopies are important in numerical weather prediction, estimating air quality, dispersion of pollutants and gases and for sustainable urban development.[43,74,75] The urban boundary layer is frequently modeled as either 2D canopies,[76–78] single–scale cubic or rectangular–prism elements[10,24,31] or rectangular–prism elements with random heights.[31,79] There are experimental[80,81] and numeri-

cal[82,83] studies that have considered case-specific urban geometries as well.

A typical urban canopy has been estimated to be composed of roughness elements of aspect–ratios between 1 and 3.[10] However, increasing urbanization and population pressure are leading to ever taller urban structures. High-rise skyscrapers of aspect–ratios up-to 23 are now being built (111 West 57th Street, New York City completion expected in 2016) although a ratio of below 10 is more common for high-rises.[84] Compared to cubic roughness and low-aspect ratio roughness, high aspect–ratio roughness (high, slender elements) has received much less attention. Wind tunnel experiments to study the case of aligned arrays of rectangular roughness of aspect ratio slightly exceeding 1 were conducted by Hagashima et. al.[31] They used arrays of rectangular blocks of aspect–ratio 1–3 in various configurations. They considered uniform arrays of aspect–ratios 1 and 1.5, and mixed arrays with a combination of cubes and rectangular blocks (cases with aspect–ratio 2 and 3 were considered). They observed that the "diamond" arrangement, which corresponds to a 45° flow angle had higher drag when compared to the corresponding aligned arrangement. They also reported that the mixed arrays had a higher drag when compared to uniform arrays at the same values of λ_f and λ_p. A similar trend was also noted in simulations of Yang et. al.[63] For uniform arrays, they noted generally an increase in the drag and z_o scaled by element width w with an increase in aspect–ratio from 1 to 1.5, as well as higher z_o values for staggered arrangements when compared to aligned arrangements.[31] Few systematic studies on the aerodynamic effects of higher aspect-ratio roughness can be

found in the literature.

For high aspect–ratio with moderate-to-high plan-area ratios, it can be expected that only part of the roughness element will be exposed to a vigorous flow while the lower part of the canopy will be more sheltered, and thus may not be affected by the outer flow. As has been noted by many researchers before in the context of flow over cubes with high values of λ_f, mutual sheltering between the elements leads to portions of roughness elements being shaded from the flow (see for e.g. the discussion in Refs 52, 85, 86 etc.). At high values of frontal area-ratios, the flow becomes similar to a driven cavity,[19,87] although it should be noted that such a scenario might not hold for sparse canopies and for staggered arrangements where the flow can penetrate into the rough layer. These effects will be described in Chapter 4 where rectangular–prism roughness elements with varying aspect–ratios and arrangements are considered.

1.4 Scientific Objectives and Thesis Outline

Connecting the roughness morphology to the mean flow response for a general rough surface is a very important endeavor and a field of active research, with applications in a wide variety of fields and covering a large range of spatial scales. The aim of this thesis is to add to the knowledge in this area by quantifying and parameterizing the relationship between rough surface morphology and the flow response. The scope of this thesis is restricted to the fully rough regime where the response is independent of the Reynolds number and depends only on the geometry. Further, much of the

analysis is carried out on single–scale roughness elements and fairly canonical geometries and arrangements. Even with these simplifications, the parameter space is fairly daunting and an attempt has been made to traverse as much of this parameter space as feasible, using both high-fidelity simulations and phenomenological models. The method and tools employed are described in more detail in the next chapter. From there we begin by investigating the problem of biofouling and its effects in Chapter 3. In Sec. 3.1, a detailed analysis of flow over individual acorn barnacles is presented. Simplified representations of the acorn barnacles, which are more amenable for parametric studies, are also generated, and the flows over these simplified representations are compared against those over the actual barnacle geometries. Next, using arrays of these elements, idealized biofouled surfaces are generated, and simulations conducted so as to parameterize the flow behavior as a function of the roughness element density (Sec 3.2).

A stated goal of this study is to provide a quick and accurate engineering tool that can predict the drag on such surfaces. This requires more in–depth knowledge on the effect of roughness–element aspect ratio and arrangement on the mean flow response. To further develop such knowledge, as a first step it is more convenient to consider simpler element geometries, namely rectangular prisms of various aspect–ratios. Thus in Chapter 4 idealized urban canopies (rectangular–prism elements with varying aspect–ratio and arrangement) are considered. Representative slices are chosen from the large parameter space and simulations are carried out to calculate the

aerodynamic parameters for these configurations. The analytical model of Yang et. al.[63] is extended for high aspect ratio elements, and the predictions from the model are compared to the LES results. These results are also used to attempt a generalized model for predicting the drag for more general rough surfaces presented in the Appendix A. In the penultimate chapter, Chapter 5, a formulation for an explicit relation that connects the rough surface aerodynamic properties to the morphological features is developed. This formulation is currently restricted to rectangular prism or cuboidal roughness elements in specific arrangements, but does show explicitly how the arrangement affects the mean flow response. Using this approach, non–dimensional geometric parameters can be obtained which can collapse the data for various rough surfaces with cubic elements onto a single curve as also predicted by the explicit relation.

Thus a suite of tools are presented – ranging from a methodology for high–fidelity simulations of turbulent flow over complex rough rough surfaces to an explicit relation that can predict the flow properties as a function of the surface parameters (albeit with a restricted applicability regarding the rough surface morphology). Such models are useful since the aerodynamic parameters can be calculated as a function of the geometry, which as discussed, represents an important requirement in many practical applications. An example application of such an approach is shown in Appendix D where the relation of drag to the geometry is leveraged to carry out a techno–economic analysis of the cost of biofouling for a class of naval vessels. This is a somewhat simple

analysis with many assumptions but shows the potential of a predictive drag model and also illustrates how we can start from a fundamental study and create tools of engineering relevance. Finally the thesis concludes with Chapter 6, summarizing the results of the preceding chapters and offering future directions.

Chapter 2

Methodology

This chapter will describe in detail the various tools and methods employed in the rest of the thesis. First, the high–fidelity technique for modeling spatially growing boundary layers over rough walls will be discussed in Sec. 2.1. This large–eddy simulation methodology provides a versatile tool to solve accurately the flows over complex rough geometries that are encountered in many practical applications. These large–scale computations are complemented by analytical flow models for predicting the aerodynamic parameters of a given rough surface. The analytical models are developed via extending the analytical model of Yang et. al.[63] which will be discussed briefly in Sec. 2.2.

2.1 Large–eddy Simulations of Turbulent Boundary Layers over Macro–Scale Roughness Elements

Numerical simulations of high Reynolds number spatially growing turbulent boundary layer flows over rough–surfaces have a number of challenges, including issues related to resolving or modeling the near wall geometry and gradients, specifying realistic inflow conditions etc.

Direct numerical simulations (DNS)[26,88] and wall–resolved large–eddy simulations (LES)[89,90] have been used to study the problem of rough wall boundary layers. However, the grid estimate scales as $Re^{1.8}$ for resolving the inner layer[91,92] and the total cost is $Re^{2.4}$ when considering the cost of time advancement.[92] Thus for wall bounded flows at high Reynolds numbers the wall resolved simulations will have very high grid requirement, and the cost would be very high especially if required to do a parameter sweep with a number of simulations. Thus a wall–modeled LES approach is frequently employed,[37,92] wherein the near wall gradients are modeled rather than resolved.

The current study uses the in–house code Vicar3D, which has capability to perform both DNS and wall-modeled LES. The many components of Vicar3D will be explained briefly in the following sections. Vicar3D solves the filtered incompressible Navier–Stokes equations, including a sub–grid scale model for the unresolved velocity scales,

coupled with the Sharp–Interface Immersed Boundary method[61,62] (described in Sec. 2.1.1) to resolve the macro–scale roughness elements. An integral wall model[93] is used to impose the wall–stress (presented in Sec. 2.1.2) along with a modified rescale–recycle method[93] to generate the turbulent inflow (Sec. 2.1.3).

The grid–filtered version of the incompressible Navier–Stokes equations can be written in the conservative form as

$$\partial_t u_i + \partial_j \left(u_i u_j \right) = -\frac{1}{\rho} \partial_i p + \nu \partial_j \partial_j u_i - \partial_j \tau_{ij} \tag{2.1}$$

where u_i is the grid–filtered velocity, p is the grid–filtered pressure, ν the viscosity and τ_{ij} is the subgrid stress tensor. The deviatoric part of τ_{ij} is usually modeled using an eddy–viscosity concept as

$$\tau_{ij} - \frac{1}{3} \delta_{ij} \tau_{kk} = -2 \nu_T S_{ij} \tag{2.2}$$

where S_{ij} is the grid–filtered strain–rate tensor $1/2(\partial_j u_i + \partial_i u_j)$, and ν_T is the sub–grid scale eddy viscosity. There are many approaches to model the eddy viscosity with their associated advantages and drawbacks.[94–98] The approach used for the current study follows the dynamic version of the Vreman–type model proposed by You and Moin.[99] The Vreman type model expresses the eddy diffusivity in the form

$$\nu_T = C_v \Pi^g \tag{2.3}$$

where Π^g is a quantity that depends on the velocity gradients, and it has the property that it becomes zero for cases where the eddy-viscosity is required to vanish.[98,99] The details of the exact form of Π^g and the implementation of the dynamic version are provided in Ref. 99. This method requires a test filtering to be done on the velocity which uses a box filter of size $2\Delta^g$ where Δ^g is the grid size.

Using Eq. 2.2 we can express the filtered Navier–Stokes equation, Eq. 2.1 as

$$\partial_t u_i + \partial_j \left(u_i u_j\right) = -\frac{1}{\rho}\partial_i p + \partial_j \left(\nu_{MT}(\partial_j u_i + \partial_i u_j)\right) \tag{2.4}$$

where $\nu_{MT} = (\nu + \nu_T)$ includes both the molecular and the eddy viscosities. The grid–filtered velocity field also satisfies the divergence free condition

$$\partial_i u_i = 0, \tag{2.5}$$

and these equations (Eq. 2.4 and 2.5) have to be solved along with suitable boundary conditions. The numerical solution of these equations is carried out on a collocated Cartesian grid (all variables are stored at cell-center), using a second order fractional step method,[100] where we first solve for an intermediate velocity field u_i^*. This intermediate field is not divergence free and is used to calculate the pressure from a Poisson equation for pressure. Finally the pressure gradient is used to correct u_i^* to obtain the final divergence free velocity field u_i. The equations to be solved are given below in the discretized form using a forward Euler method for easier discussion of

the method, while Vicar3D uses a 2^{nd} order accurate Adam–Bashforth scheme for the convective term and a 2^{nd} order accurate implicit Crank–Nicholson scheme for the viscous terms (for relaxed stability criteria). The first step in the fractional–step method is then to solve for u_i^* and then for p using

$$\frac{u_i^* - u_i^n}{\Delta t} = -\left[\frac{\delta}{\delta x_i}\left(U_j u_i\right)\right]^n + \left[\frac{\delta}{\delta x_j}\left(\nu_{MT}\left(\frac{\delta u_i}{\delta x_j} + \frac{\delta u_i}{\delta x_j}\right)\right)\right]^n \tag{2.6}$$

$$\frac{\delta}{\delta x_i}\frac{\delta p}{\delta x_i} = -\frac{1}{\Delta t}\left[\frac{\delta U_i^*}{\delta x_i}\right] \tag{2.7}$$

where $\delta/\delta x_j$ is the central differencing operator. Thus the spatial derivatives are also second order accurate. The pressure Poisson equation is solved using a geometric multi–grid solver with a Gauss-Siedel method as a smoother. Note that the implementation uses a face–centered velocity U_i for the convective derivative and also to calculate the divergence. Zang et. al.[100] showed that separate updating of the face–centered and cell-centered velocities would achieve discrete mass conservation, while avoiding the problem of pressure–velocity decoupling for collocated grids. The face– and cell–centered velocities are updated thus

$$u_i^{n+1} = u_i^* - \Delta t\left[\frac{\delta p}{\delta x_i}\right]_{cellcenter} \tag{2.8}$$

$$U_i^{n+1} = U_i^* - \Delta t\left[\frac{\delta p}{\delta x_i}\right]_{facecenter} \tag{2.9}$$

and U_i^* at each face–center is calculated by linear interpolation of u_i^*. To enable

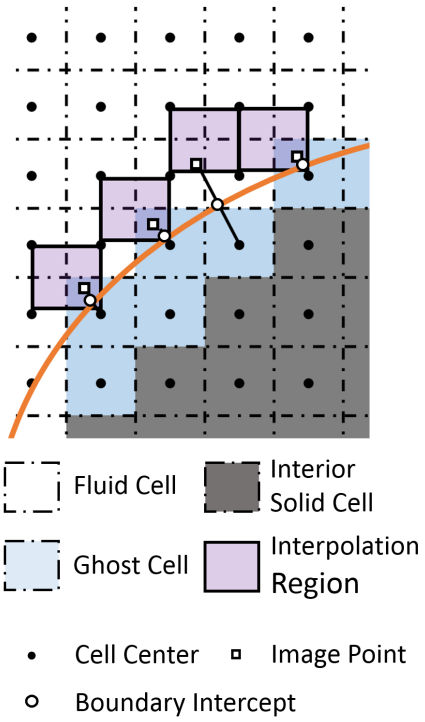

Figure 2.1: Sketch showing the cells used for the sharp–interface immersed boundary method.

solutions for complex geometries, where the body will not conform to the Cartesian grid, the code uses a Sharp–interface Immersed Boundary formulation which will be explained in the next section.

2.1.1 The Sharp–Interface Immersed Boundary Method

The sharp–interface method, illustrated in Fig. 2.1 is used to treat complex boundaries without need for a body–fitted grid. The implementation is based on a ghost–cell method which is locally second order.[61,62,101] The immersed boundary is input in the form of an unstructured triangular mesh immersed in a Cartesian grid. The solution

domain is divided into a solid region and a fluid region based on the presence of the immersed boundary. The solid cells closest to the boundary are termed ghost–cells and are used to implement the boundary conditions on the immersed body. Image points are created by mirroring the ghost cells across the boundary using the normals. The distances to the body–intercept point are kept the same for the ghost and image points to achieve higher order accuracy. The value of the variable at the image point (velocity, pressure) is interpolated using the values from the surrounding grid points and is used to apply the boundary condition. The boundary condition is applied via the ghost cell, such that for a no slip wall the velocity at the boundary intercept is zero (or equal to some imposed velocity). A similar approach is used to impose the Neumann pressure boundary condition. For the wall-modeled simulations the wall stress τ_w at each boundary intercept point is obtained from the Integral wall model as explained in the next section. For wall modeled simulations in lieu of the no–slip condition, the wall stress at the body intercept point is imposed as discussed in the next section.

Note that the value of the variable at an image point can depend on the value of the variables at either its own, or other ghost cells, and as such these interpolations have to be iterated with the set of discretized governing equations at the fluid cells until convergence. More details on the immersed boundary method and the implementation of the current method can be found in Refs 61, 62. The sharp–interface immersed boundary method will be used to apply the no–slip condition on the walls for the

simulations of boundary layer flow over individual barnacles in Sec. 3.1.

2.1.2 The Integral Wall Model

For high Reynolds number turbulent flow simulations, an integral wall model, which is discussed in more detail in Ref. 38, will be used to model the wall stress. This wall model uses a von–Karman Paulhausen method with assumed shape–functions to model the unresolved region near the solid wall. This method has the advantages of a Reynolds number independent cost, while still capturing non–equilibrium effects like flow–acceleration, pressure gradients etc. In this section a brief overview of the method and its coupling with the immersed boundary method is provided.

Consider a rough surface as shown in Fig. 2.2 which has a local coordinate system, x^w parallel to the surface and z^w normal to the surface. The correct stress condition τ_w should be applied at all the boundary intercept points. The velocity profile within a layer extending from the rough surface to the LES sampling point Δ_z away in wall–normal distance, is to be modeled and coupled to the outer LES. This velocity profile is assumed to consist of two layers – (a) an inner layer with a linear profile which is either the viscous (no additional modeled roughness) or the roughness (with additional modeled roughness) layer and (b) a meso–layer where the velocity profile obeys the equilibrium log–law along with a correction term to account for the non–equilibrium effects. The spatio–temporal filtered velocity profile $\langle u \rangle$ is assumed to

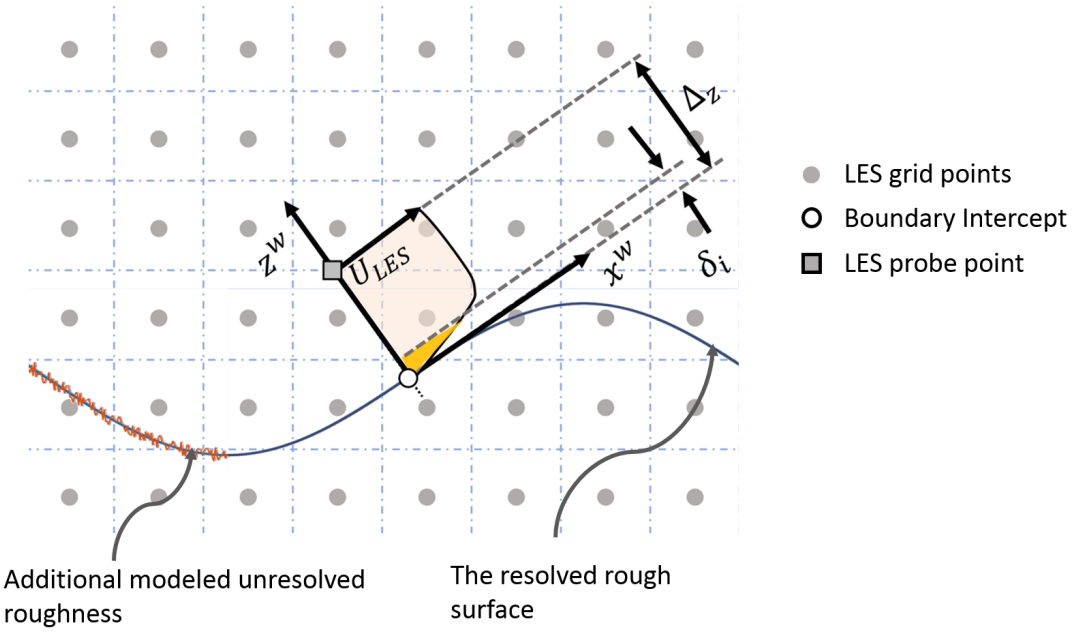

Figure 2.2: A schematic illustrating the integral wall model

follow the ansatz[38]

$$\begin{aligned} \langle u \rangle &= u_\nu \frac{y}{\delta_\nu} && 0 \le z \le \delta_i, \\ \langle u \rangle &= u_\tau \left[C + \frac{1}{\kappa} \log \frac{z}{\Delta_z} \right] + u_\tau A \frac{y}{\Delta_z} && \delta_i < z \le \Delta_z. \end{aligned} \tag{2.10}$$

The spatial filtering is of the order of the LES resolution, and the temporal filtering is an exponentially relaxed filtering to represent the scale–separation between the outer and inner fluctuations (see Ref. 38 for more details). This discussion assumes surface variation only in the streamwise direction, but in reality the code can handle a surface which has both streamwise and spanwise variation.[38] For the specified ansatz, there are 6 unknowns in the assumed shape. There are two velocity scales – the friction velocity u_τ and the velocity scale in the inner layer u_ν; and two length–scales – the

viscous length scale associated with the inner layer, δ_ν and the height of the inner layer in the local wall–normal direction, δ_i. The coefficient 'A' represents the strength of the linear correction that takes into account the non–equilibrium effects and the term C ensures C^0 continuity between the the log–law and the inner layer profiles. To solve for these 6 unknowns, 6 appropriate constraints are used.[38] The first four include velocity continuities at δ_ν and Δ_z and specifications for δ_i and δ_ν. Additionally the velocity scales u_τ and u_ν are related though the wall stress to obtain

$$u_\tau^2 = \tau_w = u_\nu^2 + \int_o^k C_d \alpha_L \langle u \rangle^2 \, dz^w \tag{2.11}$$

where the second term is the additional specified unresolved roughness of height k, having drag coefficient C_d and a leaf area density α_L. Yang et. al.[38] also provides a specification in terms of the roughness height z_o. In the absence of additional roughness this equation reduces to $u_\nu = u_\tau$. The final constraint is provided by the vertically integrated momentum equation within the modeled region $0 < z < \Delta_z$. All of these equations can be expressed analytically and solved in a coupled manner till convergence. More details of the implementation and various tests and validation cases are found in Ref. 38. Note that for the version where the surface variation occurs in both x and z there would be eleven unknowns, but the basic method is the same.[38] This methodology leads to a robust and cost-effective tool that can successfully simulate turbulent flows over macro–scale roughness elements at high

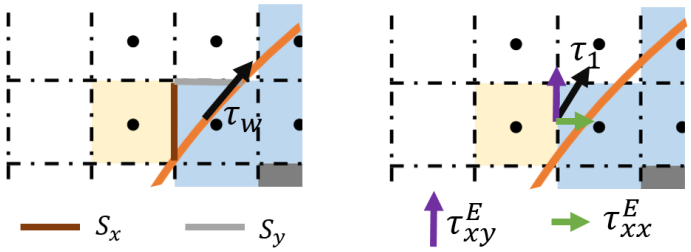

Figure 2.3: Sketches illustrating (a) projection of the immersed boundary area to the cells faces in x and y directions, S_x on face $F1$ and S_y on face $F2$. (b) projection of wall stress τ_w onto components on the cell face $F1$ for implementing the boundary condition.

Reynolds numbers.

To impose the boundary condition in Vicar3D, the wall–stress calculated at each boundary intercept is projected onto the faces as shown in Fig. 2.3. To calculate the stress on the faces, the area of the immersed boundary within a cell, S is first projected onto the x (S_x)and y directions (S_y) (Fig. 2.3a). The wall stress on the faces are calculated using this projected area. (Fig. 2.3b). For example the stress on the face $F1$ is given by

$$\tau_1 = \tau_w \frac{S_x}{S}; \quad \tau^E_{xx} = \tau_1 n_x; \quad \tau^E_{xy} = \tau_1 n_y \tag{2.12}$$

where n_x and n_y are the x and y components of the unit vector in the direction of the stress. These stresses are then imposed directly in the RHS of the momentum equation for the cells which are adjacent to the ghost cell. The RHS term in Eq. 2.6 is modified by incorporating the projected wall stress. Consider the cell with index (I,J,K). The implementation can be explained by considering the v momentum

equation. The RHS for the v momentum equation can be written as

$$\left[\frac{\delta\tau_{yx}}{\delta x}\right]_{(I,J,K)} + \left[\frac{\delta\tau_{yy}}{\delta y}\right]_{(I,J,K)} + \left[\frac{\delta\tau_{yz}}{\delta z}\right]_{(I,J,K)}$$
$$\frac{\tau_{yx}^{E} - \tau_{yx}^{W}}{\Delta x} + \frac{\tau_{yy}^{N} - \tau_{yy}^{S}}{\Delta y} + \frac{\tau_{yz}^{F} - \tau_{yz}^{B}}{\Delta z} \tag{2.13}$$

where E, W, N, S, F, B are the six faces – East, West, North, South, Front and Back. Now for cells which are adjacent to a ghost–cell, the RHS is modified to incorporate the correct stress condition. This can be illustrated using an example as in Fig. 2.3. Consider the highlighted fluid cell in yellow. The stress calculated in Eq. 2.12 is used to obtain

$$\left[\frac{\delta\tau_{yx}}{\delta x}\right]_{(I,J,K)} = \frac{\tau_{yx}^{E} - \tau_{yx}^{W}}{\Delta x} = \frac{\tau_1 n_x - \left[\nu_{MT}\left(\frac{\delta u}{\delta y} + \frac{\delta v}{\delta x}\right)\right]_{(I-1/2,J,K)}}{\Delta x} \tag{2.14}$$

Similarly the other components can also be calculated depending on the face on which the wall stresses are projected to.

The method will be used to apply the wall stress conditions for simulations of turbulent flows over arrays of idealized barnacles (Sec. 3.2) and cuboidal elements (Chapter 4).

2.1.3 Rescale–Recycle Method for Inflow Generation

All the cases simulated in this thesis have a boundary layer that is spatially growing in the streamwise direction. This requires specification of the inflow velocity profile, and to obtain the correct inflow condition a rescale–recycle method for rough walls[93] is used. This method is based on the original recycling method of Lund et. al.[102] but is modified for the case of rough walls, where the fluctuations at a recycle plane located a downstream distance are rescaled and fed back to the inflow. For rough–walls this method is modified to take into consideration the length and velocity scales imposed by the roughness.[93] A sketch of the method is shown in Fig. 2.4. The velocity fluctuations at the recycle plane are scaled based on the ratio of the friction velocities at the rescale and the inlet plane. The wall–normal height of the fluctuations are also scaled by appropriate length scales – the fluctuations in the region outside the roughness sublayer is scaled via the ratio of the boundary layer heights, while within the roughness sublayer they are scaled by the ratio of the length–scale l_d, which is the height of the region in which the roughness heterogeneity has an effect (see Ref. 93 for more details). For the case of homogeneous roughness surfaces, l_d can be expected to be a constant and this ratio becomes 1. A weighting function is also used to smoothly transition between the two regions.[93] These rescaled velocity fluctuations are then fed back into the inlet. The details of the method and implementation can be seen in more detail in Ref 93. Figure 2.4 shows schematically the rescale–recycle method

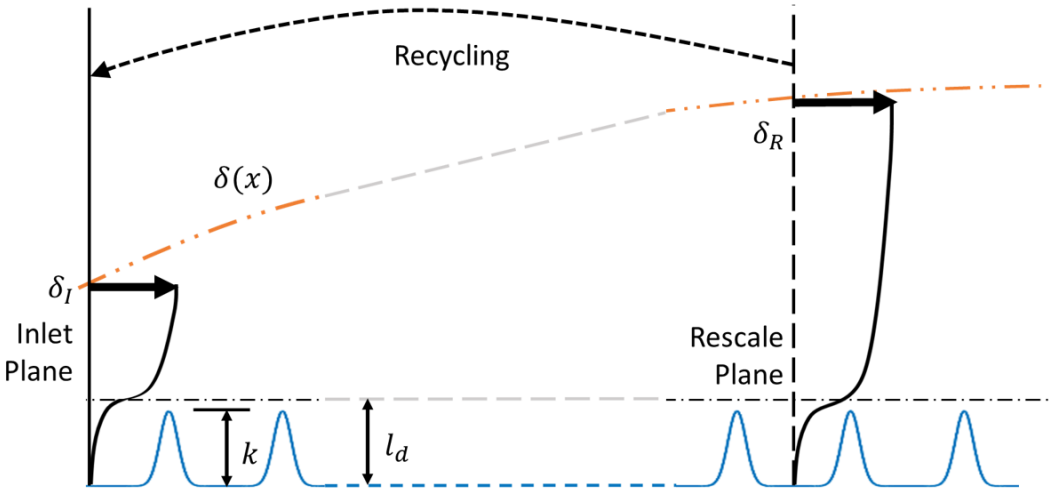

Figure 2.4: An illustration of the rescale–recycling method for rough wall boundary layers.

for rough walls.

The ViCar3D code described in these sections is fully parallelized using MPI. The code has been validated for a variety of cases.[38,61,103,104] A validation that is directly relevant to the present study can be found in Ref. 38, where the LES results are compared with experimental data from Ref. 105 for flow over an array of wall attached cubes. The methodology has also been used to simulate flow over arrays of various types of roughness elements including 2D bars, hemispheres and frustums.[38,63,106]

2.2 An Analytical Model for Predicting the Aerodynamic Properties

As discussed in the introduction there have been many studies exploring physics based predictions for the rough–surface aerodynamic properties, particularly the approach of "canopy models" where the effect of the roughness element is treated as a distributed drag force. One such model which will be extended in this study is the analytical model of Yang et. al.[63] The basis of the model is the classic von-Karman Polhausen approach that assumes shape functions for the wall–normal variation of the streamwise velocity. The rough wall boundary layer is modeled as comprising of two regions - the inertial logarithmic layer and an exponential velocity profile within the roughness sub-layer (Fig. 2.5). The assumed shape function is expressed according to:

$$\begin{aligned} U &= U_h \exp\left[a\left(z/h-1\right)\right], && 0 < z < h; \\ U &= u_\tau/\kappa \left[\ln\left(\frac{z-d}{z_o}\right) + W(z/\delta)\Pi\right], && h \leq z < \delta; \end{aligned} \tag{2.15}$$

where κ is the von–Karman constant and δ is the boundary layer thickness. There has been some discussion in the literature regarding the universality of the log–law, and the value of κ is measured to be between 0.37-0.41 for various flow conditions and configurations.[107–109] There have been some recent studies where the value of κ is not taken as a fixed constant but is treated as a parameter to be fitted.[26] In this thesis, the conventional approach is followed, and a fixed value of κ is used for

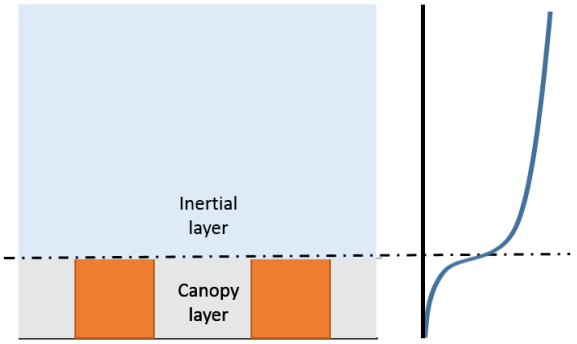

Figure 2.5: An illustration of the 2–layer canopy model.

both the model and the log–law fit of the LES. The value used is 0.4 in this study, and it should be noted that a different value of κ would still result in similar trends that are reported here albeit with a difference in the measured and predicted values of the aerodynamic parameters. The wake function $W(z/\delta)\Pi$ is used to characterize the deviation from the log–law due to outer–layer dynamics with $W(1) = 2$ and Π is $O(1)$.[19,23] For the velocity profile inside the canopy, the exponential profile has been shown to be a fair representation.[63] Note that a point–by–point accuracy for the velocity profile is not required, but rather the aim is to capture the integral effects. For example there is a shear –layer region near the canopy height with a much sharper velocity gradient[26,110] which is not captured by this profile. Another point to note is that for the assumed shape function in this model, the region immediately above the roughness element where there could be possible deviations from the log–law due to the effect of the roughness element[18,111] is not considered. Instead it is assumed that the log–law is valid all the way down to the roughness height h.

There are five unknown parameters in the model: the effective roughness height

(z_o), the zero-plane displacement (d), the friction velocity (u_τ), the canopy height velocity (U_h) and the exponential layer attenuation coefficient (a). It is straightforward to obtain four constraints by matching velocities at the canopy height ($z = h$) and the boundary layer height ($z = \delta$), and by applying the momentum balance and the equation for zero-plane displacement from Ref. 22. For applications to cuboidal and other roughness elements with a constant sectional projected frontal area dA_f independent of the wall normal distance z (e.g. $dA_f = wdz$ for cuboidal elements), the model expresses z_o and d purely in terms of the unknown attenuation coefficient as

$$\frac{z_o}{h} = \left[1 - \frac{1}{1-\exp(-2a)} + \frac{1}{2a}\right] \exp\left[-\kappa/\sqrt{\frac{1}{2a}C_d\lambda_f\left(1-e^{-2a}\right)}\right] \tag{2.16}$$

$$\frac{d}{h} = \frac{1}{1-\exp(-2a)} - \frac{1}{2a} \tag{2.17}$$

To calculate the friction velocity u_τ from z_o and d Eq. 2.15 can be used taking $z = \delta$ and $U = U_o$. As discussed earlier at $z = \delta$, $W = 2$ and the streamwise velocity at $z = \delta$ is given by

$$\frac{U_o}{u_\tau} = \frac{1}{\kappa}\ \ln\left(\frac{\delta - d}{z_o}\right) + \frac{2\Pi}{\kappa}. \tag{2.18}$$

This provides a way to calculate u_τ with a specified value of the wake correction (Π).

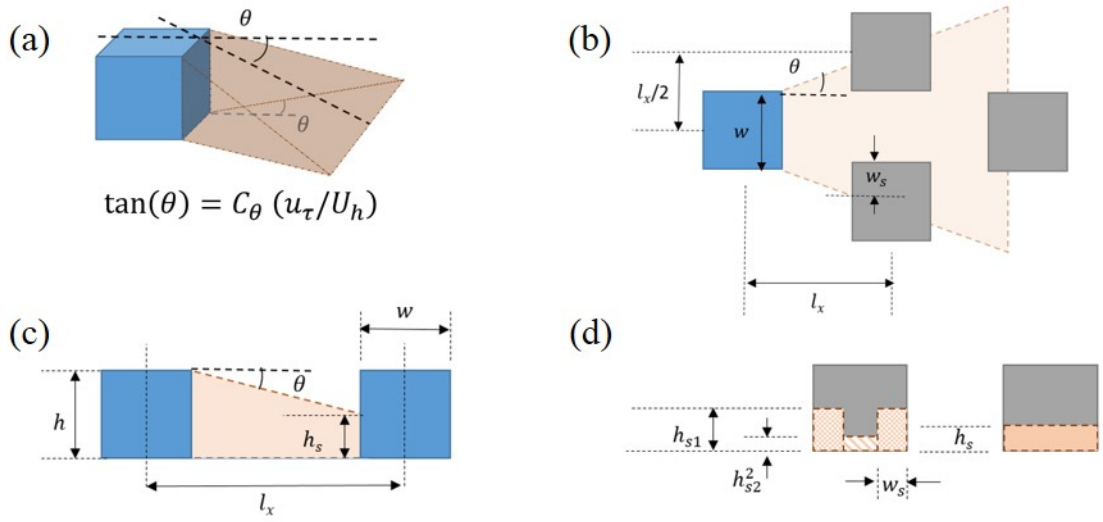

Figure 2.6: Illustration of the (a) volumetric sheltering and shading for (b) aligned (side view) and (c) staggered (top view) arrangements. (d) is equivalent shaded height for a staggered arrangement.

With this value of u_τ, the canopy height velocity U_h is

$$\frac{u_\tau}{U_0} = \frac{\kappa}{\ln\left(\frac{\delta - d}{z_0}\right) + 2\Pi} \tag{2.19}$$

$$\frac{U_h}{u_\tau} = \sqrt{\frac{1}{C_d \lambda_f}}\left[\frac{2a}{1 - \exp(-2a)}\right]. \tag{2.20}$$

Note again that these equations hold only in the case of roughness elements having constant sectional frontal area $dA_f(z)$. For more general elements one would need to know the distribution of $dA_f(z)$ and integrate the equations to obtain expressions for these unknowns.[63]

To determine the unknown attenuation coefficient Ref. 63 used a volumetric shading model which is a phenomenological description of the low momentum region

behind the roughness elements. This low momentum region "shades" other roughness elements downstream, leading to a shaded area as illustrated in Fig. 2.6. This geometrically obtained shaded area is converted into an equivalent shading height h_s (Fig. 2.6d). Using the momentum balance over the unsheltered region, the following expression for a as a function of h_s can be obtained

$$a = \frac{a_o}{1 - h_s/h} \tag{2.21}$$

with the value of $a_o = 0.4$ valid for rectangular roughness elements.[63] The model assumes that the spreading rate in the streamwise and spanwise directions is determined by the ratio of the turbulent velocity scale u_τ to the convective velocity scale U_h (Fig. 2.6) and the spreading angle is expressed as

$$\tan\theta = C_\theta \frac{u_\tau}{U_h}, \quad \text{where} \quad C_\theta = \left[\frac{2h}{3w} + \frac{1}{3}\right], \tag{2.22}$$

so that C_θ depends explicitly on the roughness element aspect–ratio h/w as noted. This model was shown to work well for moderate to low-aspect–ratio cases ($h \leq w$) in Ref. 63. However as discussed in that paper, the model is not suitable for high aspect–ratio roughness elements, i.e. when $h >> w$. For high aspect–ratios this model gives a very high value for C_θ, which leads to a shaded region which spreads excessively in the spanwise direction, a behavior that is not physically reasonable. In Sec. 4.3 this method will be extended to be applicable to high aspect–ratio elements.

A method will also be shown to obtain an explicit relation for given arrangement of cuboidal roughness elements from this model in Chapter 5.

Note that these simple expressions for z_o and d (Eqs. 2.16 and 2.17) hold true only for the constant $dA_f(z)$ case. The expressions for z_o and d for a more general element are,[63]

$$\frac{u_\tau}{U_h} = \sqrt{\frac{C_d}{A_T}\int_0^h \exp[a(z/h)-1]dA_f(z)} \tag{2.23}$$

$$\frac{z_o}{h-d} = \exp\left[-\frac{\kappa}{u_\tau/U_h}\right] \tag{2.24}$$

$$\frac{d}{h} = \frac{\int_0^h \exp[a(z/h)-1]zdA_f(z)}{\int_0^h \exp[a(z/h)-1]hdA_f(z)} \tag{2.25}$$

The expression for the attenuation coefficient (Eq. 2.21) will also no longer hold true and a full integral balance in the unsheltered region has to be carried out according to

$$C_{DH}U_h^2\int_{h_s}^h dA_f(z)dz = C_d\int_{h_s}^h [u(z)]^2\, dA_f(z). \tag{2.26}$$

In Appendix A this framework will be used along with a generalized shading model to develop a methodology to predict the aerodynamic properties of a general rough surface.

2.3 Summary

In this chapter the tools that will be used to study the problem of turbulent boundary layer flow over marco–scale roughness elements have been presented. These tools include both the high–fidelity numerical simulation tool and also an analytical phenomenological flow model. These tools will be employed in understanding and quantifying the effect of rough surface morphology on the mean flow response.

Chapter 3

Boundary Layer Flow over Surface Mounted Acorn Barnacles and Idealized Barnacle Models

3.1 Simulations of Flow over Individual Attached Barnacles

Acorn barnacles are a significant agent of biofouling on marine vessels. The flow and drag force induced by these organisms protruding from the surface is important since it can affect the vessel operation costs. Not much data are available in the literature

on flow over such barnacles. A recent study[112] has been carried out on flow over pairs of barnacles of the species *Amphibalanus amphirite*. In this study detailed Particle Image Velocimetry measurements of turbulent flow over the attached barnacles (single and pair) were performed to investigate the flow characteristics. Barnacle geometries similar to the ones used in this previous study will be used in the current research to investigate, using simulations, the hydrodynamics of flow over isolated (single) acorn barnacles.

This setup can be considered to be a special case of flow past a surface mounted obstacle, and a number of past studies have examined such flows for canonical shapes such as cylinders,[113–116] rectangular prisms,[117–120] hemispheres[121] and pyramids.[122] From these studies, it is known that such flow depends on flow parameters like the Reynolds number, boundary layer thickness as well as the geometry. In particular, previous studies[113] have shown that for low-aspect ratio (defined as the ratio of the object height to base-width) objects, which are relevant to the current study, one can expect a symmetric type of shedding around the body rather than the anti-symmetric Karman-type shedding usually observed for larger aspect-ratio (i.e. slender) objects. For shapes such as cylinders, this switch occurs at an aspect-ratio of about 2.5.[113]

Studies of flow over pyramids,[122,123] which have some general similarity to acorn barnacles, have found that for these shapes, the flow structure depends on the cone angle as well as the incidence angle. They noted that periodic shedding is absent for pyramids of large cone angles ($> 75^o$). In another relevant study, Castro et. al.[124]

carried out experiments and computations for stratified flow past surface mounted cones and compared their results with those for non-stratified flows. They found that in non-stratified flows, three-dimensional effects increased as the taper of the cone was reduced, while the reverse was true for stratified flows. Okamoto and Yagita[125] performed experiments on flow past a surface mounted cone and examined the flow structures and separation points for this flow.

The objective of the current study is to examine flow past surface mounted acorn barnacles using barnacle geometries derived directly from collected specimens. In addition, two additional canonical barnacle geometries are synthesized from the collected specimens and we compare the flow past these canonical geometries against those for the actual barnacle. These comparisons are used to examine the key features of the barnacle wake and the degree to which these features can be recovered in the flow simulations with the canonical geometries. For the current study both the boundary layer thickness and the Reynolds number of the flow are fixed. The boundary layer thickness (δ) is chosen such that at a location x downstream where the body is located it has a height $\delta/h = 1.4$. The Reynolds number based on the base diameter is 2000. The Reynolds number is large enough so as to generate a unsteady wake that is characteristics of practical situations, while still being resolvable. The chosen boundary layer thickness reduces the grid requirements and ensures a rich interaction between the boundary layer vorticity and the barnacle wake. The simulations are run in DNS mode - i.e. a no–slip wall is imposed on the solid surfaces

and no model is used either for the wall stress or the eddy viscosity. On an actual ship the barnacles would face various boundary thicknesses depending on their location and also various Reynolds numbers depending on the ship speed and barnacle size.

3.1.1 Barnacle Geometry

Well resolved barnacles geometries for two distinct barnacles used in a recent experimental study on flow over acorn barnacles[112] were obtained from Prof. Mike Schultz (US Naval Academy) and were provided by Dr. Eric Holm of the Naval Surface Warfare Center, Carderock Division. They are shown in Fig. 3.1a,b and designated as $B1$ and $B2$. These scans were carried out by While these two barnacle geometries have a number of similarities, one key difference between the two is that $B2$ has a more significant upward protrusion of the ventral opening plates when compared to $B1$. Both barnacle surfaces have characteristically corrugated or ridged surfaces with ridges running from the bottom to the top of the shell, although the ridges are more pronounced in $B1$. The above represent some typical variations observed in such specimens. Along with $B1$ and $B2$, a modified barnacle geometry $B2M$ is derived from $B2$ by removing the protrusion (Fig. 3.1c), to investigate the effect of the protrusion on the flow response. The basal geometry of the $B1$ and $B2$ are compared in Fig. 3.1d, and it is seen that $B2$ has a base that is close to circular by comparison against the circumscribed circle (black dotted line), while $B1$ has some deviation from the circular shape in the fore part which faces the flow, while the aft is

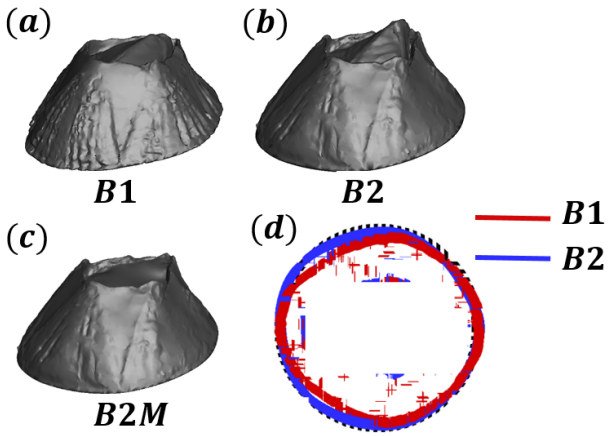

Figure 3.1: (a) $B1$ and (b) $B2$ are the acorn barnacle geometries used in this study. (c)$B2M$ is a modified barnacle created from $B2$ by removing the protrusion (d) is a top view comparing the base of the barnacle geometries $B1$ and $B2$ along with a superimposed circle (dashed black line).

more circular. With regard to the canonical barnacle geometries, acorn barnacles are usually characterized as cones (cylindrical or elliptical) or frustums of a cone[126] and we also employ a frustum of a cone to represent the acorn barnacles. Specimens are selected from a rock with attached barnacles (see Fig. 3.2a) collected on the North-east American Atlantic shoreline. The rock was brought into the lab and individual barnacles attached to the rock were scanned using a 3D scanner with a resolution of 0.1 mm. While there were over a hundred barnacles ranging from a few millimeter to a few centimeters on the rock, seven moderate to large size barnacles were chosen for a detailed geometric analysis. Fig. 3.2b shows one typical scan of a barnacle, and it shows that the scanning procedure is capable of resolving some fine features on the barnacle shells.

The conical frustum geometry is defined by three parameters: the basal and apical

diameter (D_1 and D_2 respectively) and frustum height (H). The shape can therefore be expressed in terms of the two non-dimensional shape parameters (D_2/D_1) and (H/D_1). For each of the seven barnacles, the scans were first used to estimate these parameters. Table 3.1 shows these values for the seven selected barnacles (Fig. 3.2c). The average values of the shape parameters are $D_2/D_1 = 0.34$ and $H/D_1 = 0.37$ which are within the range measured by Spivey.[126] These values are used to create the smooth frustum geometry S (Fig. 3.2c). The corresponding values of these parameters for barnacle $B1$ are $D_2/D_1 = 0.39$, $H/D_1 = 0.32$ and for B2 are $D_2/D_1 = 0.44$ and $H/D_1 = 0.37$.

To characterize the ridges on the barnacles a 2D slice of the barnacle near the base is taken (Fig. 3.2e), and a convex hull is fitted onto it. The mean difference between the two surfaces is calculated to obtain the mean ridge depth (Δ) which is then used to model the ridges as a sinusoidal disturbance on the base shape (circle) by the equation

$$R(\theta) = \frac{D_1}{2}\left[1 + \frac{\Delta}{2D_1}\sin(M\theta)\right] \tag{3.1}$$

where M is the number of ridges on the surface (Fig 3.2g). The value of M is determined by inspection for each specimen, and the difference from the surface to a fitted convex hull is used to the extract the ridge depth. Based on the analysis of seven barnacles, the average value of ridge depth is found to be $\Delta/D_1 = 0.05$ and a large variation in the number of ridges on the barnacles is found (15-30). No other published data on ridge depth could be found for comparison of these parameters.

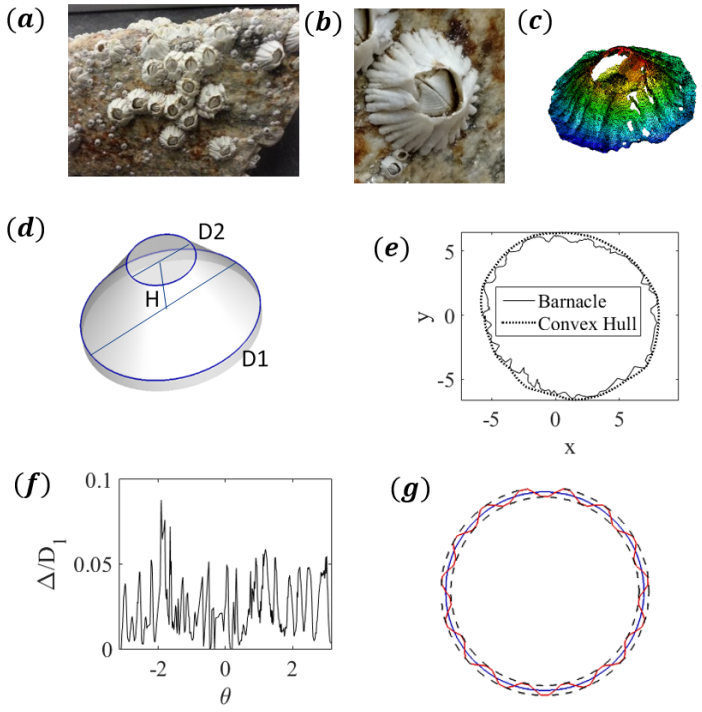

Figure 3.2: (a) acorn barnacle specimens collected (b) zoomed in view of a barnacle (c) 3D scans and (d) simplified shape (S) generated. (e) convex hull fitted to the slice at a plane. (f) ridge–depth calculated as the the radial difference between the convex hull and the barnacle surface. (f) cross section of the generated object R incorporating the ridges.

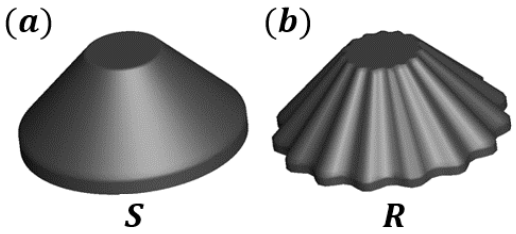

Figure 3.3: The two simplified representations (a) the smooth frustum S and (b) the frustum with ridges R.

Table 3.1: Table 1. Measurements from the scanned specimens

	Diameter Ratio D_2/D_1	Aspect Ratio $AR(H/D_1)$	Ridge Depth Δ/D_1	No. of ridges M
Specimen1	0.32	0.39	0.03	28
Specimen2	0.35	0.37	0.03	30
Specimen3	0.40	0.38	0.04	17
Specimen4	0.32	0.35	0.04	18
Specimen5	0.32	0.34	0.05	21
Specimen6	0.31	0.37	0.07	15
Specimen7	0.40	0.42	0.06	15
Mean	0.34	0.37	0.05	21

Based on the above analysis, two canonical conical frustum barnacle geometries were generated; the first was a smooth barnacle without ridges (designated as S), that had the shape parameters given by the average values in Table 3.1. The second was a ridged barnacle (designated as R), that was generated by superimposing the modeled ridges on S. The ridged barnacle is created in the following manner - the radius at a height y for S is $R(y)$ which is modified using the form of Eq. 3.1 to obtain the shape of the ridged frustum in the form of $R(y, \theta)$ at a height y. This is done for all values of y from 0 to H and for $\theta = 0$ to 2π which gives a frustum with ridges superimposed. For creating the ridges, the average value obtained from the analysis for the mean ridge depth $\Delta/D_1 = 0.05$ is used along with $M = 15$ for the number of ridges. These frustum shapes are shown in Fig. 3.3. The five models $B1$, $B2$, $B2M$, S and R form the basis for the simulations and analysis in the rest of this chapter.

3.1.2 Solution Setup

The solution methodology is given in detail in Sec. 2.1, and for this case, since the flow is fully resolved additional models are not required for the wall stress or the eddy viscosity, i.e. the code is run in DNS mode. Thus the sharp–interface immersed boundary method is used to apply the no–slip condition on the barnacle surface as explained in Sec. 2.1.1. The boundary layer flow past the barnacles is solved in a large cuboidal computation domain of size $L_x \times L_y \times L_z$. The streamwise coordinate is x, the spanwise coordinate is z and the wall–normal coordinate is y. The lower surface of the domain is a no-slip wall, and the boundary conditions at the inflow, lateral and top planes are based on the laminar Blasius boundary layer profile. At the outflow plane, a convective boundary condition is employed that allows vortices to convect out from the domain with minimal distortions. For the current simulations, a domain size of $L_x \times L_y \times L_z = 30D_1 \times 40D_1 \times 20D_1$ is chosen, and the barnacle is placed at a distance of $20D_1$ from the inlet. This large domain size and barnacle placement ensures that the boundary conditions on the outer boundaries do not have any significant spurious influence on the flow in the region-of-interest, which is around the barnacle and in its wake. The simulations in the current study have been carried out on the JHU HHPC clusters and NSF XSEDE machines using 64–384 processors.

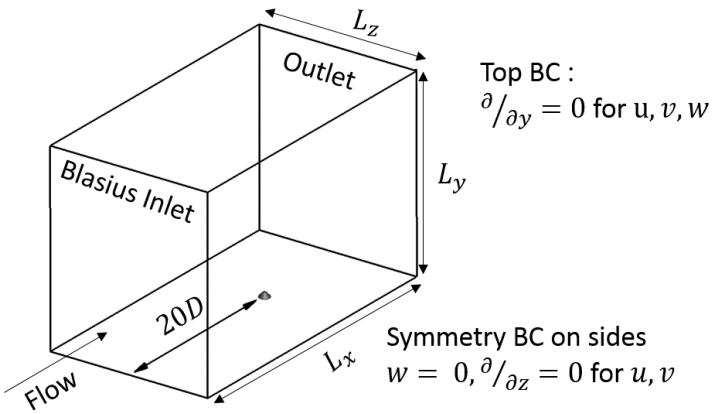

Figure 3.4: The domain and the boundary conditions used in the simulations.

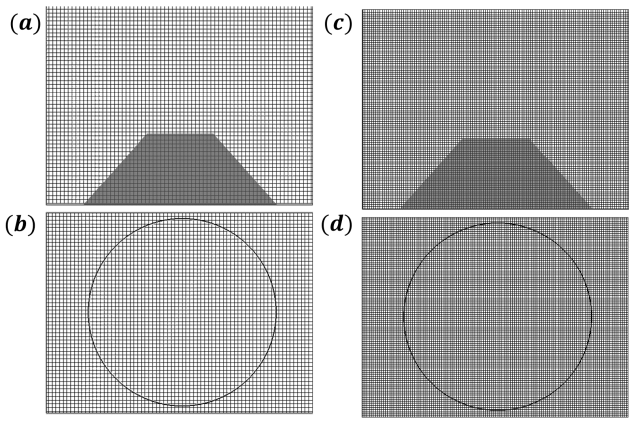

Figure 3.5: (a) Side and (b) top view of the mesh for GRID1 illustrating the resolution present around the object. (c) and (d) correspond to those for GRID2.

3.1.3 Grid Refinement

As stated earlier, a Reynolds number of 2000 based on the barnacle base diameter is chosen and based on experiences in conducting simulations of flows using ViCar3D, a grid (designated as 'GRID1') with $256 \times 64 \times 128$ in the $x - y - z$ directions was chosen, that was considered appropriate for resolving the key features of this flow for all the barnacles at this Reynolds number. In this grid, the region around the barnacle and the near wake was provided the highest resolution (with average grid spacing of $0.02D_1$ as shown in Fig 3.5a,b) and the grid is slowly stretched away from this region in all directions. The time–step used is $\Delta t = 0.01D_1/U_\infty$ which gives a maximum CFL number close to 0.5. The convergence residual error for the advection equation is set at 10^{-8} and for the pressure Poisson equation at 10^{-5} which gives a maximum error in the divergence of the order of 10^{-7}. In order to examine the adequacy of this grid, systematic evaluation of the flow was conducted for the barnacle models S and R for the two grids of differing resolutions: GRID1 and a finer GRID2, which had $384 \times 128 \times 256$ grid points. This represents an overall $6X$ increase in resolution from GRID1 to GRID2 and almost double the resolution around the body and in the near wake (Fig. 3.5c,d). Simulations were conducted for S and R with both grids until the flow reached a stationary state and the average drag and lift coefficient values are compared for both models on the two grids in Table 3.2. The drag and lift coefficients

are defined as

$$C_D = \frac{F_D}{\frac{1}{2}\rho U_\infty^2 A_f}, \quad C_L = \frac{F_L}{\frac{1}{2}\rho U_\infty^2 A_f}. \tag{3.2}$$

where F_D and F_L are the drag and lift forces respectively. These forces are calculated in Vicar3D by first interpolating the pressure and the stresses from the surrounding collocated grid points of the Cartesian mesh onto the centroids of the elements of the unstructured immersed boundary mesh. From these centroid values the force on the body $\boldsymbol{F}$ can be calculated by a numerical integration over the surface of the pressure and the wall stress $\boldsymbol{\tau_w}$, $\mathbf{F} = \int_B (p\hat{\boldsymbol{n}} + \boldsymbol{\tau_w}) dS$, where $\hat{\boldsymbol{n}}$ is the surface normal and dS is the elemental area. The x component of $\boldsymbol{F}$ gives the drag and the y component the lift.

The Table 3.2 shows that differences in the mean values of the drag and lift coefficients are limited to around 6% or less. Given this relatively small difference and the computational cost of the simulations on GRID2 which was $\approx 15X$ more than that for GRID1, it has been retained as the computational grid for the rest of this chapter.

3.1.4 Results and Discussion

Simulations are carried out for a minimum of 25 flow through times to ensure that the flow transients are eliminated. Statistics are accumulated for a minimum of around 10 flow over times which corresponds to 125-140 multiples of the main shedding cycle.

Table 3.2: Comparison of average drag and lift coefficients for models S and R on two grids.

Case		GRID1 $256 \times 64 \times 128$	GRID2 $384 \times 128 \times 256$	Change (%)
S	C_D	0.22	0.23	4.6
	C_L	0.19	0.20	3.1
R	C_D	0.21	0.22	5.6
	C_L	0.18	0.19	4.9

The simulations are run on 64 processors on the JHU HHPC cluster and require an average of 15 hours for 1 flow over time corresponding to a CPU time of 960 hours. The larger GRID2 tests discussed in earlier section used 384 processors and was run using the NSF XSEDE computing resources.

3.1.4.1 Instantaneous Flow Field and Vortex Structures

The instantaneous 3D vortex structures, which are identified using the swirling strength criteria,[127] is shown in Fig. 3.6 for all the cases. For all the cases, upstream of the barnacle, there is a strong steady horse–shoe vortex present, which is a characteristic of junction flows.[128] It has been observed that for cylinders at low Reynolds numbers (of order 1000 with respect to the diameter) there exists a steady horseshoe vortex. This splits into multiple steady horseshoe vortices at higher Reynolds numbers and become unsteady as the Reynolds number further increases.[129,130] Along with the horse–shoe vortex at the front, for the barnacles $B1$, $B2$ and $B2M$, it is noticed that there are also vortices being entrained in the ridges around the body. Such an effect

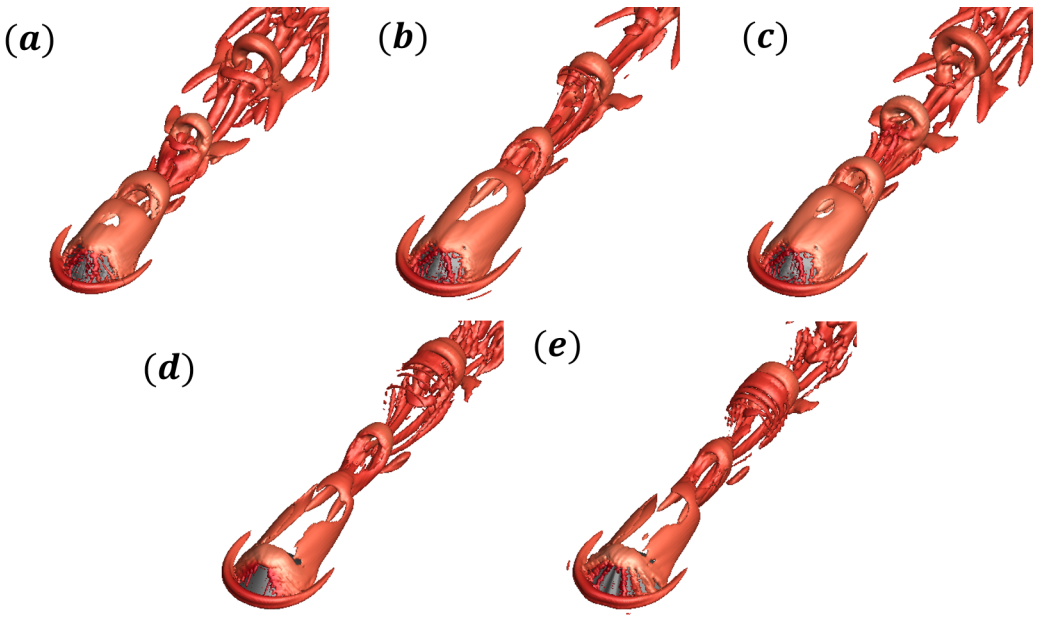

Figure 3.6: Contours of instantaneous Vortex structures generated behind the objects for the five objects.

is also present in the ridged geometry R but is of course absent in the smooth frustum S. Downstream of the object we have the generation of a trail of hairpin vortices. Such vortices are an important mechanism in the transition of the boundary layer and attached objects have been used as a viable mechanism for inducing boundary layer transition.[121, 131, 132]

Overall, for the barnacle geometries, the vortex structures compare well with the simplified shapes although differences are visible in the near wake structure – for example it can be seen that $B1$ generates the hairpin vortices at a location closer to the body as compared to $B2$ and also to S and R. This seems to be the effect of the tilted shape of $B1$ and the lower height at the leeward side as compared to the windward side. For $B2$ the protrusion seems to allay this effect. This can be

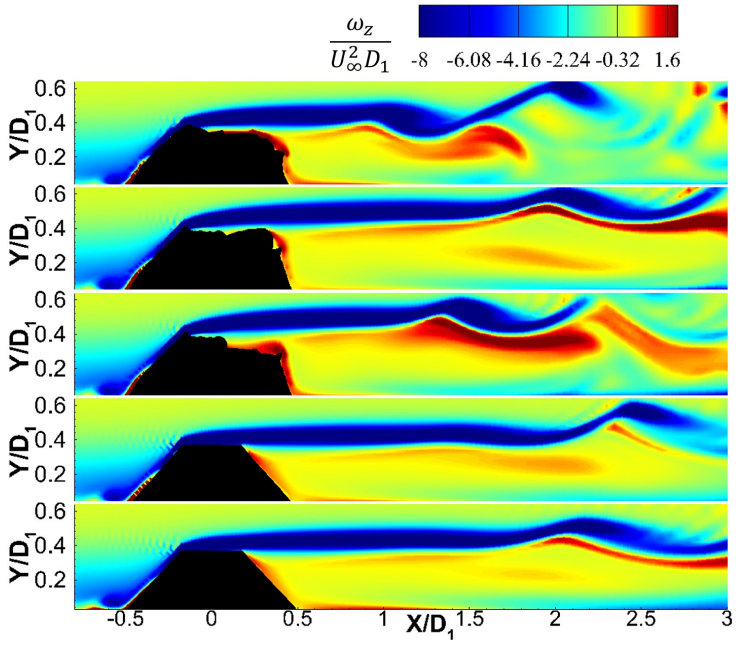

Figure 3.7: Contours of instantaneous ω_z at the mid plane.

confirmed from the results for $B2M$, which has a similar difference in the windward and leeward heights as for $B1$ and which again leads to a behavior similar to that of $B1$. This shows that even though the overall shapes of the vortex structures might be robust, the differences in geometry play a role in determining the detailed mechanics in the near wake. This can also be seen in more detail by comparing the shear layer that forms at the top free edge for the five cases (Fig. 3.7). It is seen that as expected, the shear layer rolls-up and becomes unstable downstream of the object and breaks down as it convects downstream. As discussed earlier, S, R and $B2$ have similar behavior while for $B1$ and $B2M$ the shear–layer instabilities occur earlier than the other cases. It can be seen that for S and R, the shear layer remains attached to the body till the leeward edge, while for $B2$ the protrusion provides some support

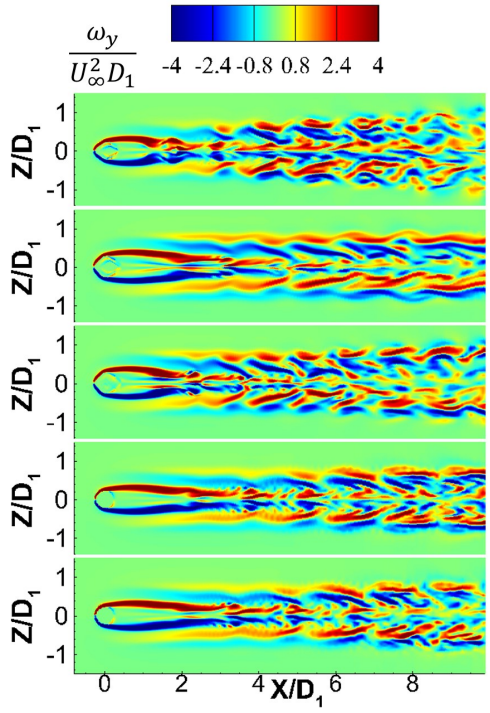

Figure 3.8: Contours of instantaneous ω_y at a location $y/D_1 = 0.32$

for the shear layer as well. Such an effect is absent for $B1$ and $B2M$ where the shear–layer separates from the body soon after the upstream edge, and this cause the instabilities to happen at a smaller distance downstream. For $B1$ and $B2M$, a region of strong positive vorticity is present, which penetrates into the top free edge indicating a strong reverse flow in that region.

It can also be seen that the vorticity is stronger for the actual barnacles as compared to the idealized geometries. The contours of ω_y at $y/D_1 = 0.35$, which is close to the apex height are shown in Fig. 3.8, and these show the symmetric shedding present in all the cases. The earlier occurrence of instabilities in $B1$ and $B2$ are evident in the ω_y contours as well. The structures are very symmetric even for the

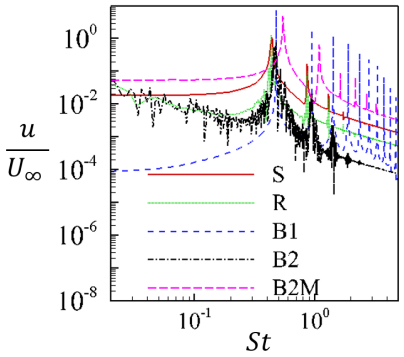

Figure 3.9: Spectra of the probe velocity for all the cases simulated at a location $x/D_1 = 1.5$ and $y/D_1 = 0.35$

barnacles $B1$, $B2$ and $B2M$. For $B1$ and $B2M$ it is also seen that the organized structures start to break down in to smaller scales, indicating a possible transition to turbulence further downstream.

To identify the frequency response of the flow, a velocity probe is used at a location $x/D_1 = 1$ behind the object and at $y/D_1 = 0.35$, which is close to the apex of the object. The strong signature of the wake–shedding is present at a Strouhal number around 0.4-0.5 for all the cases (Fig. 3.9), and it is also evident that $B2$ and R produce a broad frequency response while the other cases still seem laminar at this location with only specific frequencies corresponding to the shedding and its higher harmonics being excited. Interestingly, removing the protrusion from $B2$ leads to suppression of excitations in the other modes and a response more similar to S and $B1$ is recovered.

Table 3.3: Location of the significant points for all the cases

	P1		P2		P3	P4	P5	P6		P7	
	x/D_1	y/D_1	x/D_1	y/D_1	y/D_1	x/D_1	x/D_1	x/D_1	z/D_1	x/D_1	z/D_1
B1	-0.61	0.07	-0.73	0.05	0.20	-0.96	1.49	1.46	0.47	1.46	-0.44
B2	-0.60	0.07	-0.75	0.07	0.22	-1.10	1.78	1.81	0.55	1.83	-0.52
B2M	-0.60	0.07	-0.75	0.05	0.22	-1.10	1.53	1.60	0.51	1.60	-0.49
S	-0.58	0.07	-0.72	0.06	0.21	-0.95	1.77	1.72	0.54	1.72	-0.54
R	-0.59	0.07	-0.73	0.06	0.21	-0.97	1.79	1.73	0.55	1.73	-0.53

3.1.4.2 Flow and Wake Statistics

Flow statistics have been calculated by averaging for a large multiple of the time corresponding to the fundamental shedding frequency as discussed in the beginning of this section. In Fig. 3.10 the mean streamlines are shown in both the mid-plane and near the base. Many features of the flow can be identified and are similar to those seen for flows over rectangular and circular cylinders.[116,133,134] First the side view shows the steady horse-shoe vortex whose center is at the point P1, and P2 is the saddle point in front of the vortex. The point P3 is the saddle point at which the streamlines bifurcate with the bottom part forming a recirculation zone in front of the object. The trace of the horseshoe vortex can also be seen in the bottom plane along with the saddle point P4 which isolates the horseshoe vortex from the outer flow. The locations of P1, P2, P3 and P4 are very similar for all the cases with P1 being at a location X/D_1 close to -0.6 and $y/D_1 = 0.07$ while P2 is located at x/D_1 of close to -0.7 upstream and at a height close to 0.06. The saddle point P3 is close

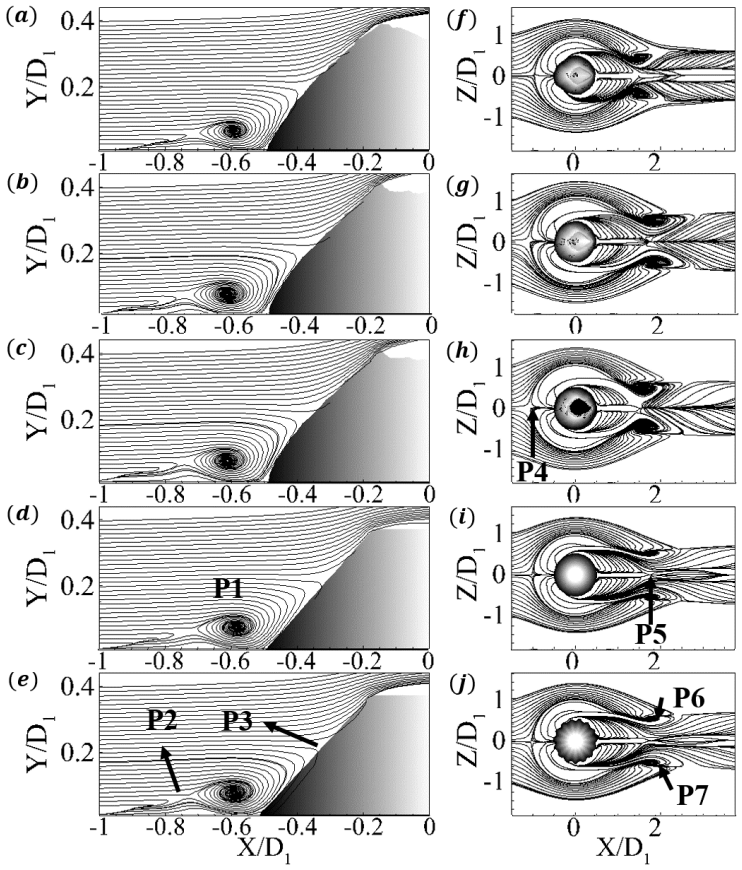

Figure 3.10: Mean streamlines in the XY center plane (a-e) and the base (f-j)

to a height of 0.2 for all the cases, and the point P4 is close to x/D_1 of -1.5 upstream of the object. Downstream of the object the flow separates and a recirculation region is present behind the object and the point P5 identifies the end of the recirculation region. P6 and P7 are the focus of separation,[120,134] points from which the flow moves upward forming spiral vortices. Table 3.3 shows the locations of the significant points for all the cases. They are broadly similar for all the cases with $B1$ and $B2M$ having smaller values for the location of the reattachment point P5 and the focii P6 and P7. The focii are also narrower in spanwise extend for these two cases as compared

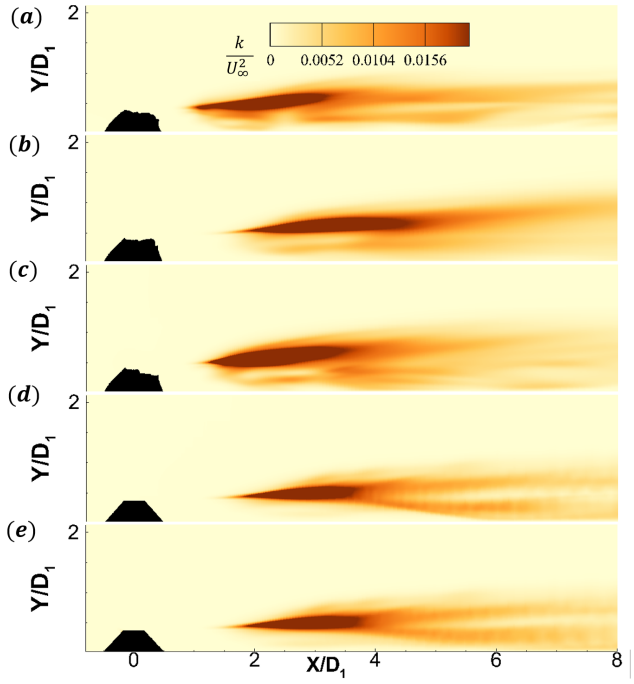

Figure 3.11: Contours of k in the XY center plane for the different cases simulated.

to the other three. The flow appears more or less symmetric for the barnacle cases even in the downstream region with the asymmetries in the significant points being comparable to the grid size.

The mean fluctuation kinetic energy (k) can be used as a measure to characterize the unsteady wake behind the objects. Note that k is calculated considering a decomposition of the flow as composed of a temporal mean and fluctuation. A triple decomposition that could remove the effects of the wake shedding frequency, the dominant mode in the fluctuations especially in the near wake, is not considered here.[135] This is because the aim is not to characterizing the stochastic fluctuations in the near wake, but rather to characterize the overall unsteadiness in the wake. The

k contours at the mid-plane are shown in Fig. 3.11 for all the cases simulated. It can be seen that they start becoming significant around a wall–normal location close to the apex of the body (around $y/D_1 \approx 0.4$) which is the region where the shear layer instabilities are initiated. The streamwise location depends on the object – as was observed from the instantaneous contours, the wake develops earlier for $B1$ and $B2M$ at a location $x/D_1 \approx 1$ downstream, while for the others it is close to a value of 2. To characterize the wake strength, the maximum along the centerline is calculated for each case and can be seen in Table 3.4. The maximum for k (k_c^m) is close to $0.04U_\infty^2$ for all the cases with S and R having slightly lower values than $B1$ and $B2$. $B2M$ has a value of 0.045 which is the highest among the cases tested. A similar behavior is seen for the maximum centerline production of k as well ($\mathcal{P}_c^m$) with $B2M$ having the highest value. The production term is defined as

$$\mathcal{P} = -\overline{u_i' u_j'} \frac{\partial \overline{U_i}}{\partial x_j} \tag{3.3}$$

where u_i', u_j' are the velocity fluctuations and U_i is the mean velocity. Apart from $B2M$, which is an artificial geometry created from an actual barnacle, the other two cases $B1$ and $B2$ have wake strengths similar to the canonical cases.

3.1.4.3 Drag and Lift Forces

The drag and lift forces on the barnacles are important to characterize the impact of biofouling. From Table 3.4 it is seen that the barnacle geometries have a drag coeffi-

Table 3.4: Comparison of force coefficients, the Strouhal number, kinetic energy and its production in the near wake region for the cases simulated.

Case	C_D	C_L	C_L/C_D	St	k_m^c/U_∞^2	$\mathcal{P}_m^c D_1/U_\infty^3$
$B1$	0.25	0.17	0.69	0.48	0.037	0.140
$B2$	0.27	0.14	0.52	0.47	0.039	0.150
$B2M$	0.29	0.17	0.59	0.53	0.045	0.230
S	0.22	0.19	0.86	0.44	0.033	0.094
R	0.21	0.18	0.82	0.44	0.034	0.093

cient 0.25-0.29 which is slightly higher than the 0.22 value for the smooth canonical geometry S. Interestingly, the addition of ridges does not lead to an increase in C_D. The lift coefficient C_L is also important for such geometries as it is important along with the drag, in predicting the chance of barnacles being detached from the surface. The barnacles have a lift coefficient ranging from 0.14-0.17 which is slightly lower than those of the canonical cases. Fig. 3.12 shows the spectra of the lift force. The response is very similar to that for the velocity that was seen in Sect. 3.1.4.1, and the dominant frequency corresponds to the dominant shedding frequency of the vortices and is also the dominant mode for the velocity spectra seen in Sect 3.1.4.1 as well. Similar to the velocity spectra, it is seen that $B1$ and $B2M$ produce well defined peaks at Strouhal numbers similar to that for the frustum S while for $B2$ and R the spectra have a range of scales present, even though there is a peak for St corresponding to the shedding frequency. For the case of R, a peak corresponding to the same Strouhal number as for S is observed (0.44), and R does not seem to exhibit any time scales associated with the ridges. It is interesting to note that $B2M$ has both a higher

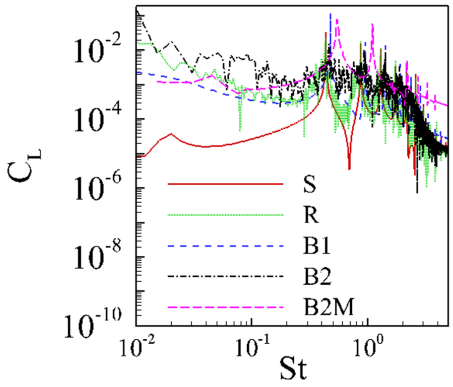

Figure 3.12: Spectra of the lift coefficient for S, R, $B1$, $B2$ and $B2M$, illustrating the peaks in the frequency response

lift and drag coefficient than the case of $B2$, while the shedding frequency also shifts from 0.47 to 0.53. It is seen that the canonical geometry S produces drag and lift coefficients that are close to those of the actual barnacles with much less geometric complexity. The additional drag due to the detailed geometry is not captured via adding organized ridges and might require addition of other geometric details.

The outcome of these detailed analyses is that the simple frustum geometry S could serve as an idealized barnacle, especially considering the significant reduction in the geometric complexity. It reproduces some of the features of the near wake and has wake strengths and Strouhal numbers similar to that of actual barnacles. The drag coefficient is slightly less, and the lift coefficient slightly higher than that of the barnacles, but they are still comparable. Thus S is chosen as the "barnacle" shape and in the next section will be used in the LES study of turbulent flow over arrays of these shapes.

3.2 Large–Eddy Simulations of Flow over Idealized Barnacle Arrays

In this section, the flow over and drag forces on barnacle fouled surfaces will be investigated. To carry out a parametric study of flow over such surfaces, a series of idealized barnacle fouled surfaces will be considered. First, the frustum geometry is chosen as an idealized barnacle shape, and these elements are then arranged on a flat plate in two patterns – aligned and staggered (Fig 3.13). Note that from this point onwards, all the discussions consider the spanwise direction as y while the wall–normal direction as z. The aligned arrangement has the elements in each row arranged in–line with the corresponding elements of the other rows, while for the staggered arrangement the elements in each row are shifted in the spanwise direction by a distance $l_y/2$ with respect to the adjacent rows. The periodic repeating tile in each case is highlighted in the figure can be considered as a "minimal" representation of each surface. The packing density is varied (by changing l_x and l_y) to create surfaces with varying frontal area ratios.

The cases simulated are tabulated in Table 3.5. Note that for these frustums the shape parameters chosen are $D_2/D_1 = 0.5$ and $h/D_1 = 0.5$, which results in $\lambda_p \approx 2\lambda_f$. This geometry gives a highest possible frontal area-ratio of $\lambda_f = 0.38$ and a corresponding plan area ratio of $\lambda_p = 0.79$ when the elements are just touching

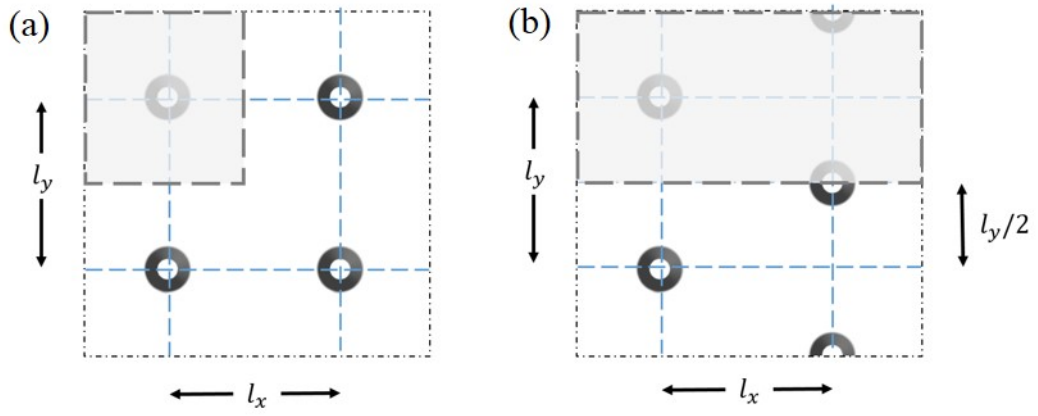

Figure 3.13: The aligned and staggered arrangement of the idealized barnacles (cases BLP05A ans BLP05S). The repeating tile is shown in light gray with a thick dashed border.

each other. First, a range of low and moderate packing densities are considered. Both aligned and staggered cases are simulated for three sets of packing densities corresponding to $\lambda_p = 0.05$, 0.10 and 0.20 and corresponding frontal area ratios $\lambda_f =$ 0.02, 0.05 and 0.09. Then for the aligned cases further simulations of very dense cases of $\lambda_p = 0.35$ and 0.79 ($\lambda_f = 0.17$, 0.38) are also carried out. Thus the whole range of packing densities is studied from a very sparse arrangement to where the elements are just teaching each other. Note that for the $\lambda_p = 0.10$ case $l_x \neq l_y$. So in total there are eight cases, and in the discussion these cases are denoted as BLPXXY, with a plan area ratio $\lambda_p = XX/100$ and an arrangement of the elements either aligned (BLPXXA) or staggered (BLPXXS).

Table 3.5: The various cases simulated for the idealized barnacle fouled surfaces.

Case	λ_p	λ_f	l_x/D_1	l_y/D_1	Arrangement
BLP05A	0.05	0.02	4	4	A
BLP05S	0.05	0.02	4	4	S
BLP10A	0.10	0.05	4	2	A
BLP10S	0.10	0.05	4	2	S
BLP20A	0.20	0.01	2	2	A
BLP20S	0.20	0.01	2	2	S
BLP35A	0.35	0.17	1.5	1.5	A
BLP79A	0.79	0.38	1	1	A

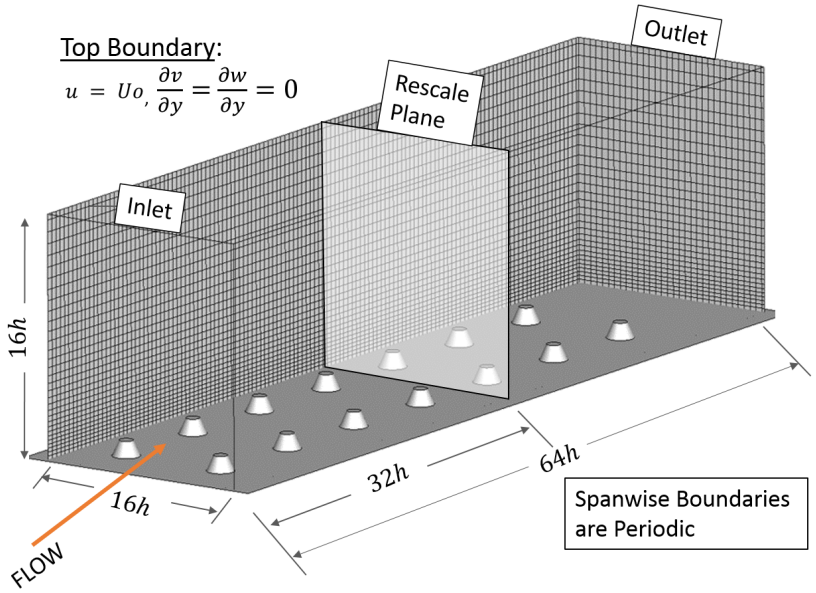

Figure 3.14: The simulation domain along with the boundary conditions and the $256 \times 64 \times 64$ grid (every other grid point is shown). The rough surface shown is an aligned array of $\lambda_f = 0.02$ (BLP05A)

3.2.1 Simulation Setup

The simulations are carried out using the methodology laid out in Sec. 2.1. The dynamic Vreman model[99] is used for the sub–grid stresses and the integral wall model[38] (Sec. 2.1.2) to apply the wall stress. No additional unresolved roughness is specified for these simulations. The modified rescale–recycle method[93] is used to generate the inlet turbulence (Sec. 2.1.3). An example simulation setup is shown in Fig. 3.14 for the case BLP05A. The domain size is $L_x = 64h$ in the streamwise direction, $L_z = 16h$ in the spanwise direction and $L_y = 16h$ in the wall–normal direction. The mesh size used is $256 \times 64 \times 64$, and the simulations are carried out at a Reynolds number of 10^5 based on the frustum base diameter and free stream velocity. The inlet boundary layer thickness is chosen to be $\delta/h = 4$, and the Reynolds number based on friction velocity (u_τ) and the boundary layer thickness is found to be in the range of 1 – 1.5×10^4. The rescale plane is chosen to be at a location $32h$ downstream. For the case of BLP35A, $L_y = 12h$ is chosen to ensure periodicity of the arrangement (and correspondingly the mesh size used is 48 in the spanwise direction for that case). That same domain is used for the simulation of BLP79A as well. The simulations are run on the DOD HPC clusters and require about 250000-300000 CPU hours for each simulation.

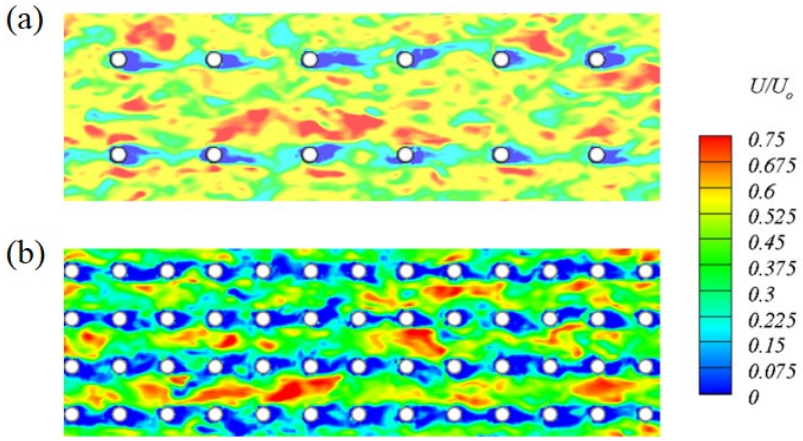

Figure 3.15: Instantaneous contours of streamwise velocity for BLP05A and BLP20A at $z/h = 0.625$

3.2.2 Instantaneous and Mean Flow Field

Figure 3.15a,b shows the instantaneous velocity field at the barnacle height for aligned configurations BLP05A and BLP20A. The latter is four times as densely packed as the former. The low–momentum region behind the roughness elements can be identified by blue contours. For BLP05A, the elements are far enough apart that the reduced momentum region behind one element does not seem to have much effect on the downstream element as compared to BLP20A. In between the roughness element rows, the presence of high speed streaks can be observed. To compute the mean flow, the simulations are carried out for close to 75 flow-over times, and statistics are collected after the first 35 flow-over times to ensure that the transients are washed away and the statistics are converged. Figure 3.16 shows the time averaged profiles of streamwise velocity for the case of frontal area ratio of BLP20A and BLP20S which

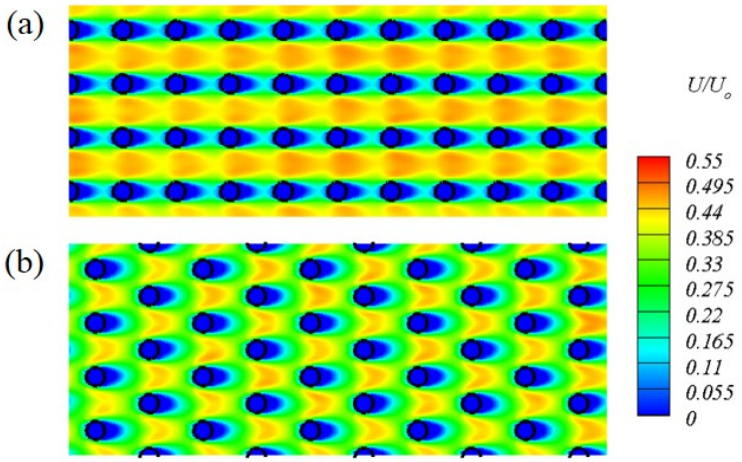

Figure 3.16: Time averaged U velocity contours for BLP20A and BLP20S at $z/h = 0.625$

have the same packing density but differing arrangement. The contours are plotted at a height of $z/h = 0.0625$ from the base. For the aligned case, the flow is accelerated in between the columns as observed in the instantaneous results as well, while for the staggered case, these streaks are broken up by the arrangement, and the elements are expected to generate increased drag since they are more exposed to the mean flow. Figure 3.17 shows the time averaged streamlines in the mid plane of a row of elements for the aligned cases BLP05A and BLP20A. For BLP20A case, the flow below the roughness height is more isolated from the outer flow while the outer flow interacts more with the roughness elements for the BLP05A case. An illustration of this is the point P3, and the saddle point where the streamlines bifurcate is closer to the apex for BLP20A as compared to BLP05A. When that point is at the apex, the inner flow is completely isolated from the surface, and this is called a "d–type roughness" or a "skimming" flow[19,136]

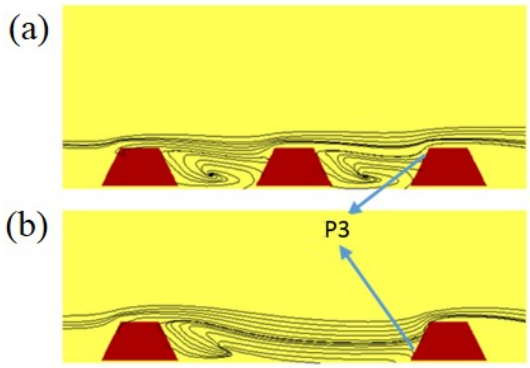

Figure 3.17: Time averaged streamlines at the mid plane for BLP20A and BLP05A cases.

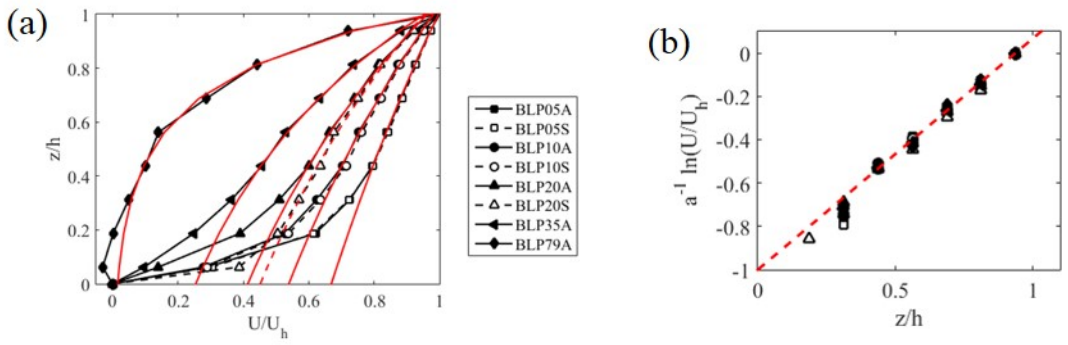

Figure 3.18: (a) Spatio–temporal averaged streamwise velocity profile in the rough layer for all the cases along with the exponential fit and (b) the corresponding linear–log plot of the canopy averaged velocity for all the frustum array cases.

3.2.2.1 Velocity Profile within the Canopy

As has been stated in Sec. 2.2 the spatio–temporal averaged velocity profile within the roughness layer is frequently employed in physics–based models of the effect of roughness. An exponential profile is expected in this distributed drag model if constant values are assumed for C_d and the mixing length[57] and has been shown experimentally and numerically to be a good approximation for cubic elements.[52,58,63] In this section

such profiles are presented for the frustum arrays to examine how they vary within the canopy. As stated, these profiles are averaged in time and in the streamwise and spanwise directions within two rows, which corresponds to two repeating tiles for the aligned simulations and one for the staggered cases. The averaging domain does not exclude the region inside the roughness elements, where the velocity is zero, to ensure continuity of the profiles at $z = h$. These profiles are shown in Fig. 3.18a for all the cases simulated – the solid lines are the aligned cases and the dashed lines the staggered data. Black lines are from the LES, and the red is the corresponding exponential fit. The exponential fit is obtained in a manner similar to that in Yang et. al.[63] by fitting the profile in the region from $z = h/2$ to h for the attenuation coefficient a. It can be seen that the exponential profile provides a good approximation in the top $70 - -75\%$ of the canopy with the profiles deviating from this profile in the near–wall region. It is also seen that for the BLP05(A/S) and BLP10(A/S), the profiles are very similar between the aligned and staggered arrangements indicating that the arrangements do not have as much effect at these moderate coverage densities. Differences can be seen for the case of $\lambda_p = 0.2$ cases with the aligned arrangement BLP20A profile indicating a steeper decline as compared to BLP20S the staggered case. This is an indication of the difference in sheltering effects with the staggered case having roughness elements being less sheltered than the aligned case as is expected. The validity of the exponential assumption can be seen further in the representation in Fig. 3.18b where all the cases are plotted in linear–log scale

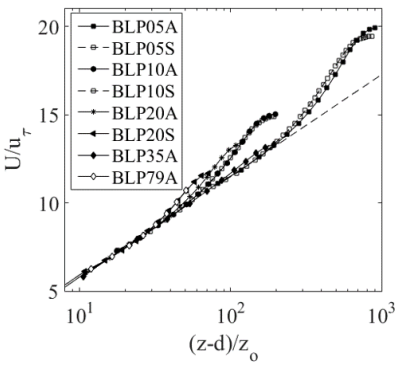

Figure 3.19: Log–linear plot of the mean velocity profile non-dimensionalized with the fitted u_τ and plotted against $(z-d)/z_o$ with model predicted d and fitted z_o for all the cases. Also shown is the log–law prediction using the dotted line.

along with the exponential fit. This shows that away form the near wall region, the exponential profile serves as a good representation of the velocity profile, similar to the observations made for the cuboidal geometries.[52,58,63]

3.2.2.2 Aerodynamic Parameters

To calculate the aerodynamic parameters, as in Sec. 3.2.2.1, the time-averaged velocity is averaged in the span and streamwise directions. The streamwise averaging is done within two rows and at a streamwise location such that the boundary layer heights are the same for all the cases. The details of the procedure will be explained in more detail in Sec. A.5 where the values are compared against model predictions. The log–laws from the fit are shown in Fig. 3.19 for all the cases simulated. In this section, the values obtained for the various cases are tabulated to illustrate quantitatively the effect of the packing density and arrangement. It is seen that at low values of λ_f, i.e. for the cases BLP05A/S, BLP10A/S, the arrangement does not have much

Table 3.6: Tabulation of the mean flow response for the cases simulated.

Case	λ_p	λ_f	$z_o/h(\times 10^{-}2)$	$u_\tau/U_o(\times 10^{-}2)$	U_h
BLP05A	0.05	0.02	0.7	5.0	0.54
BLP05S	0.05	0.02	0.8	5.1	0.54
BLP10A	0.10	0.05	4.6	6.6	0.46
BLP10S	0.10	0.05	4.7	6.6	0.46
BLP20A	0.20	0.01	5.2	7.4	0.42
BLP20S	0.20	0.01	6.4	7.8	0.38
BLP35A	0.35	0.17	6.9	8.5	0.37
BLP79A	0.79	0.38	5.7	9.7	0.34

effect on the mean flow. The values of z_o, u_τ and U_h are virtually the same between the aligned and staggered arrangement. This observation is similar to that for the case of cubic roughness elements.[10,26] The arrangement has an effect when λ_p is increased to 0.2 with the aligned case BLP20A having a lower z_o and u_τ, and a higher U_h as compared to the staggered case BLP20S. A similar result is seen in the case of cuboidal geometries as well, with the staggered arrangement producing a higher drag than the corresponding aligned arrangement. A generally trend of increasing z_o and u_τ is also observed. For cubes at high values of the frontal area ratio ≈ 0.2 the sheltering causes drag to start decreasing, however this effect is not clearly discernible here. More simulations might be required to clearly identify the trend at the high packing density limit.

3.3 Summary

The effect of laminar boundary layer flow over attached acorn barnacles is investigated, and it is seen that the flow response has various characteristics that have been identified in the literature for more canonical geometries. The flow characteristics are also compared to flows over simplified geometrical representations created from statistical analysis of scanned barnacle geometries – a smooth frustum (S) and a frustum with ridges (R). Broadly, both the mean flow and the unsteady response are similar between all the cases. A prominent symmetric type vortex shedding is noted with a Strouhal number St ranging from 0.4 to 0.5. Some geometrical features do have very noticeable effects on the flow: for example, the ridges of R and the protrusion of B2 generate a broader range of excitations in the near wake, although prominent signature of the shedding is still seen in the spectral response of the velocity and the forces. While the averaged flow response is similar, the height asymmetry (or tilt) in the streamwise direction for the barnacles does have some influence on the flow response as evidenced from $B1$ and $B2M$. Such an effect is difficult to characterize however, and does not cause much difference in the force coefficients and the shedding frequency. The simplified frustum S can serve as a good representation for the barnacle geometries, and adding ridges (R) does not lead to any additional benefits in obtaining a more realistic model. The drag predicted by the simplified shapes is slightly lower than the actual barnacle geometries. For purposes of capturing the drag

caused by acorn barnacles and the averaged flow effects, a simple frustum can serve as an idealized shape, especially considering the reduction in geometric complexity.

This frustum model is chosen as the idealized barnacle and wall–modeled LES of turbulent boundary layer flows are carried out over arrays of such elements. The instantaneous and mean flow fields are used to identify qualitative features and the effect of packing density and arrangement. The effect of the rough surface on the mean flow is quantified via the aerodynamic parameters z_o and u_τ. It is seen that for low values of λ_f the aligned and staggered arrangements have a similar response and in these regions, the effect of λ_f seems more important than that of the specific arrangement, which might be due to the large distance between the elements. At $\lambda_f = 0.1$, it is seen that the aligned case BLP20A has a lower z_o and u_τ as compared to BLP20S, the staggered case. This is similar to results obtained for the cubic case and is due to the reduced sheltering present for the staggered case as compared to the aligned case. To gain more insight into these qualitatively similar, but even simpler flows, and to characterize the effect of roughness element geometry better, a more canonical setup is chosen in the next chapter. It focuses on simulations of various aspect–ratio rectangular–prism roughness elements, frequently encountered in urban canopy configurations. The understanding gained from those simulations will be used to extend the phenomenological flow model to high aspect ratio rectangular elements in Chapter 4. A method is shown to extend it to more general rough surfaces in Appendix A where the barnacle fouled simulations will also be revisited.

Chapter 4

Mean Flow Response to Idealized Urban Canopies

As stated in Sec. 1.3 urban canopies are frequently modeled as arrays of rectangular–prism roughness elements. Flow over such canopies are important as rapid urbanization is leading to creation of structures of higher and higher aspect–ratios. However systematic studies that have quantified the effect of varying aspect–ratio on the mean flow response are lacking in the literature. In this chapter wall modeled LES on arrays of rectangular–prism roughness elements of various aspect ratios and arrangements are carried out with a view to characterizing the flow properties as a function of the geometric parameters. The parameter–space for such a study is vast – since there can be variations in the plan area density, the aspect–ratio and also the arrangement.

This problem is tackled by picking representative points from the parameter space for carrying out the large–eddy simulations. These simulations are augmented by a predictive model which is an extension of the analytical model of Yang et. al.[63] to high aspect–ratio elements.

The chapter is organized as follows: in Sect. 4.1, the LES setup is briefly described. LES results are presented in Sect. 4.2. This is followed by a generalization of the analytical roughness and sheltering model in Sect. 4.3. Finally the generalized model predictions and LES results are compared in Sect. 4.4, followed by summary in Sect. 4.5.

4.1 Simulation Setup

The details of the numerical method are discussed in Sec. 2.1. The surfaces of the roughness element are assumed to be smooth and no sub-grid roughness is imposed. Simulations of flow over rough surfaces are often carried out in channel geometries,[26,88,137–139] and there have been recent advances in using minimal channels for rough wall simulations.[140] In order to include interactions with a non–turbulent outer flow, in the present study spatially growing boundary layer flows are simulated over the rough surfaces. The methodology is similar to that used for the frustum array simulations in Sec. 3.2 and presented in Sec. 2.1.

The main objective of the simulations to be carried out for this study is to quantify the effect of roughness element aspect–ratio on the mean flow. For this purpose five

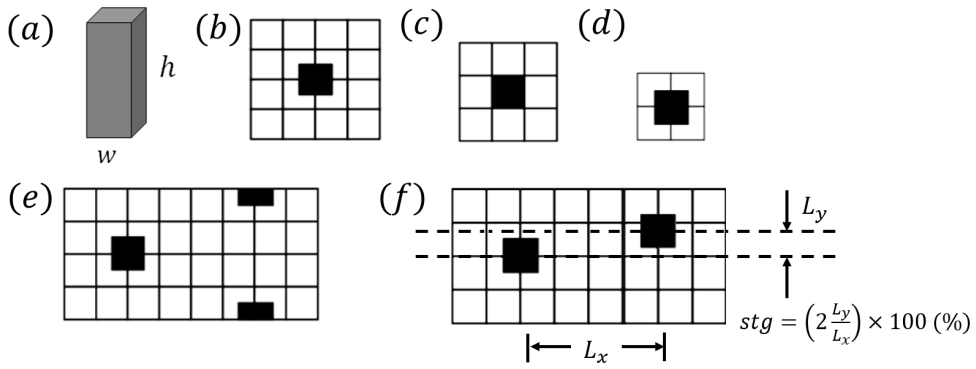

Figure 4.1: (a) shows the roughness element with base width w and height h. The arrangement of the elements are visualized using a top view of the repetitive tile. Panels (b) for case LP06A, (c) for case LP11A, (d) for case LP25A display aligned arrangements with different values of λ_p, 0.06, 0.11 and 0.25 respectively while (e) is for the case of LP06S, a fully staggered arrangement with $\lambda_p = 0.06$. Panel (f) shows one particular case of a percentage staggered arrangement ($stg = 38$).

sets of cases are used with variations in the plan area ratio (λ_p) from 0.06 to 0.25 and also different arrangements from fully aligned to fully staggered as shown in Fig. 4.1. The different cases and the associated geometric parameters are shown in Table 4.1. The case names are in the form LPNNC–ARX where LPNN implies a plan area ratio λ_p of NN percentage while ARX denotes a roughness element of aspect–ratio $AR = h/w = X$. The arrangement of the roughness elements are encoded in C with A for fully aligned and S for fully staggered. For the percent stagger arrangement is named in the fashion LPNNPYY–ARX, where PYY is used to denote an arrangement with percent stagger $stg = YY$, where the percent stagger is given by $stg = (2L_y/L_x) \times 100$ (see Fig. 4.1f). The first three cases LP06A, LP11A, LP25A (Fig. 4.1b–d) are aligned cases with different values of $\lambda_p = 0.06$, 0.11 and 0.25 respectively while LP06S (Fig. 4.1e) is the fully staggered arrangement

Table 4.1: The five sets of cases simulated. AR is the aspect–ratio and stg is the percentage stagger varying between 0 (fully aligned) and 100 (fully staggered). Each set has N cases. ($^{\#}$) The first and last case in LP06PXX–AR2 are the same as LP06A-AR2 and LP06S-AR2

	AR	λ_p	λ_f	stg	N
LP06A–ARX	X=1,2,3,4	0.06	0.06–0.25	0	4
LP11A–ARX	X=1,2,3,4,5,6,7	0.11	0.11–0.77	0	7
LP25A–ARX	X=1,2	0.25	0.25,0.5	0	2
LP06S–ARX	X=1,2,3,4,5,6	0.06	0.06–0.38	100	6
LP06PXX–AR2	2	0.06	0.12	XX=($00^{\#}$), 12, 25, 38, 50, 62, 75, 88, ($100^{\#}$)	7

with $\lambda_p = 0.06$. The last set of cases, LP06P, shown in Fig. 4.1f has fixed aspect–ratio ($AR = 2$) and plan area (λ_p=0.06) while the percentage stagger (stg) is varied from fully aligned ($stg = 0$) to fully staggered ($stg = 100$). Figure 4.2 shows the simulation domain and boundary conditions which are common for all the cases along with the rough surface geometry and instantaneous streamwise iso–velocity surfaces inside the roughness layer for one of the cases of the set LP11A, namely LP11A–AR4 with aspect–ratio 4 ($h/w = 4$). The simulation domain is chosen to be $64w$ in the streamwise, $24w$ in the spanwise and $32w$ in the wall-normal direction, where w is the width of the roughness element and a grid size of $256 \times 128 \times 96$ is used for all simulations. The roughness elements are resolved using the immersed boundary method, and the incoming boundary layer height is set at $(\delta - h)/w = 5$ for all cases. This choice of δ will be justified later in Sect. 4.2. For the case of cubes ($AR = 1$) this gives an inlet value of $\delta/h = 6$, which is similar to the value used in Ref. 63. For the largest aspect ratio considered ($AR = 7$), this gives $\delta/h \approx 1.7$ but as will be seen,

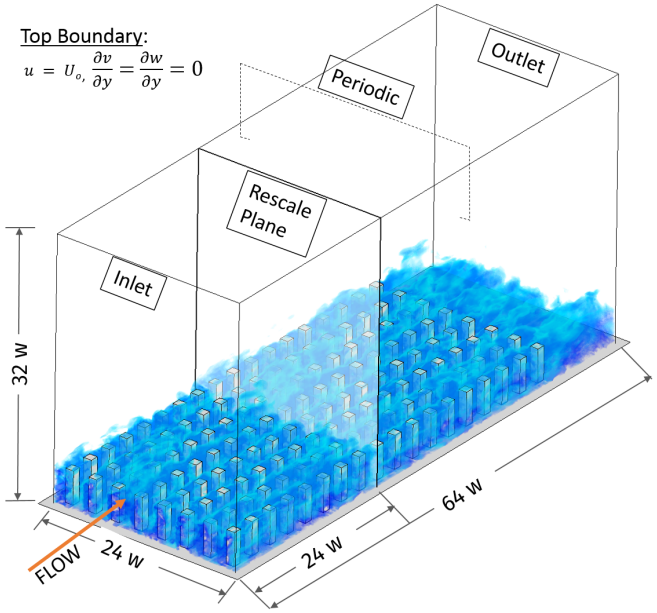

Figure 4.2: Instantaneous iso-surfaces of streamwise velocity inside the roughness layer for LP11A–AR4, ($\lambda_p = 0.11, h = 4w$). The iso-surfaces shown corresponds to $u/U_o \leq 0.26$.

in such cases the zero-plane displacement is quite large. Thus only the top part of the roughness elements interact with the flow such that δ is then still significantly larger than the "exposed" portions of the elements. The Reynolds number based on the width of the roughness element w and the free–stream velocity U_o is $Re_w = 10^5$ while that based on the inlet boundary layer thickness Re_δ is of the order of 10^6. This is high enough for the flow to be in the fully rough regime and the corresponding frictional Reynolds number, Re_τ, is of the order of 10^5.

4.2 Mean Flow within and above the Roughness Layer

In this section the mean flow velocity profiles are compared for the various sets of simulations. The averaged profiles within and outside the canopy provide a qualitative illustration of the effect of roughness element aspect–ratio and arrangement on the mean flow. Also presented are the tabulation and comparison of the values of z_o, d, u_τ and U_h for all the cases. The details of the fitting of the log–law and determination of the parameters are discussed later in Sect. 4.4, where the parameters are also compared against predictions from an analytical model. Figure 4.3a-d shows the temporally and spatially (in streamwise and spanwise directions) averaged velocity profiles inside the roughness canopy for the different cases. The simulations are run for 100 domain flow-through times (based on the free stream velocity U_o), and the temporal averaging is done for the last 50 flow-through times. The streamwise averaging is done within a region extending for two rows which corresponds to one repeating tile for the staggered case and two for the aligned case. The streamwise location is chosen so as to obtain similar boundary layer heights for the different cases and the region chosen is within the region extending from $x = 24w$ to $x = 51w$ from the inlet. Furthermore when averaging the velocity inside the canopy, both the solid (with zero velocity) as well as the fluid region are included in order to avoid

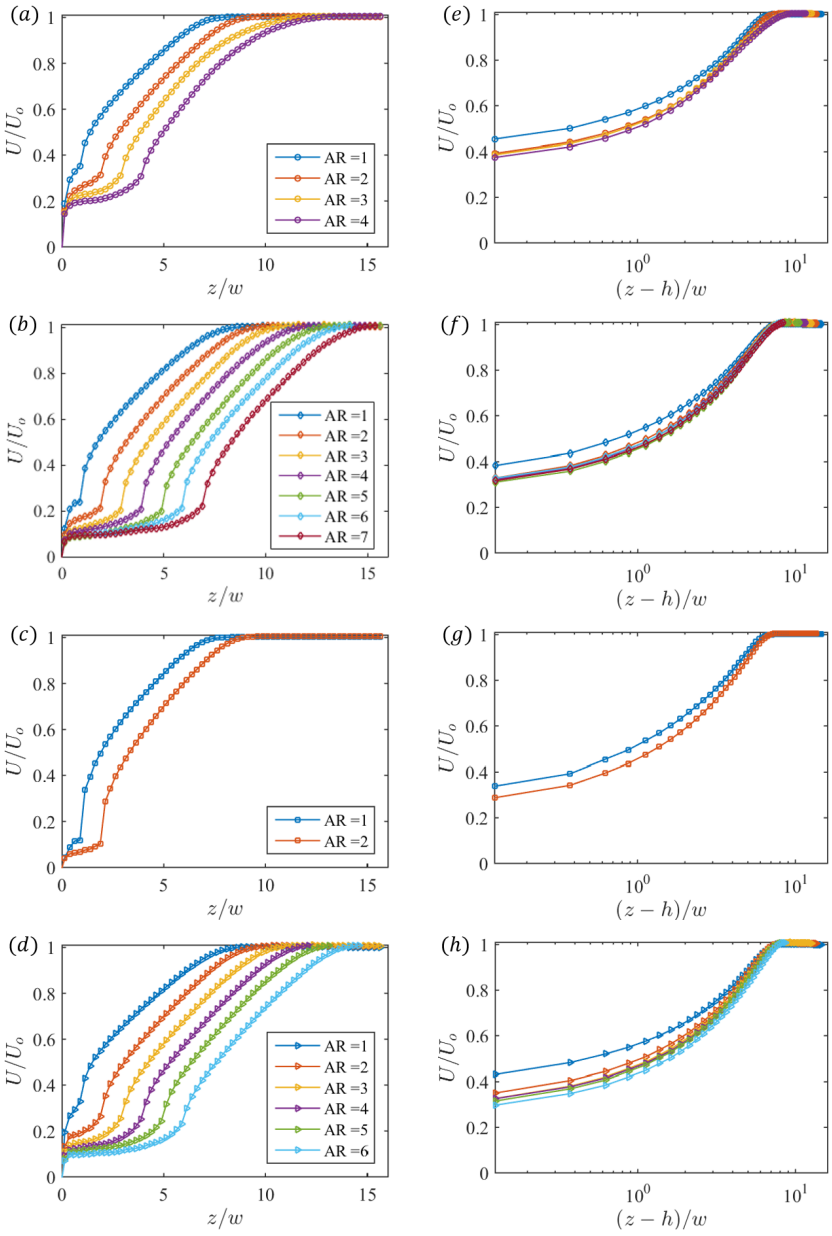

Figure 4.3: Temporal, spanwise and streamwise averaged velocity profiles for (a) LP06A (b) LP11A (c) LP25A (d) LP06S. (e)-(h) show the corresponding profiles shifted by h and plotted in log–scale.

discontinuities of the resulting mean velocity at the canopy height. Note also that although the streamwise direction is not homogeneous due to the growing boundary layer, within the range that is being averaged the growth in the boundary layer thickness is insignificant ($< 1\%$), and it is thus valid to do the averaging in the streamwise direction. It can be seen that the velocity quickly attenuates inside the canopy, and this provides support for the idea that due to mutual sheltering the "active" part of the roughness element can be significantly smaller than h. These observations justify the use of $(\delta - h)/w = 5$ instead of the more restrictive requirement of having δ being a fixed multiple of h. This will be shown to adequately enforce the desired separation of scales for the cases addressed in this chapter.

The velocity profiles for the four sets of cases in Fig. 4.3a-d illustrate the effect of element aspect–ratio. It can be seen that as the aspect–ratio increases, most of the variation of velocity in the canopy region seems to occur within a height of order w below the canopy height. Afterwards there is a region of almost constant velocity within the canopy. The effect of the element aspect–ratio on the outer–layer is illustrated in Fig. 4.3e-h wherein the origin is shifted to the roughness element height h. The effect on the mean velocity seems to be highest as AR goes from 1 to, 2 and the profiles do not show much difference for higher aspect ratios, at least for the aligned cases. For the staggered case (Fig. 4.3h) the outer profiles do seem to still be affected by the element aspect–ratio even at the higher aspect–ratios. This can be seen quantitatively in the values of the aerodynamic parameters for the first four

Table 4.2: Aerodynamic parameters determined for the four sets of cases with varying aspect ratio.

	AR	z_o/w	d/w	u_τ/U_o	U_h/U_o
LP06A	1	0.02	0.62	0.05	0.43
	2	0.08	1.38	0.07	0.38
	3	0.13	2.24	0.08	0.38
	4	0.16	3.17	0.08	0.37
LP11A	1	0.04	0.64	0.06	0.34
	2	0.12	1.44	0.08	0.30
	3	0.16	2.35	0.08	0.29
	4	0.17	3.32	0.08	0.30
	5	0.18	4.31	0.08	0.29
	6	0.16	5.31	0.08	0.32
	7	0.17	6.31	0.08	0.31
LP25A	1	0.06	0.70	0.07	0.26
	2	0.10	1.62	0.07	0.23
LP06S	1	0.03	0.57	0.06	0.39
	2	0.21	1.13	0.09	0.32
	3	0.47	1.70	0.12	0.30
	4	0.73	2.26	0.14	0.30
	5	1.07	2.83	0.17	0.29
	6	1.43	3.40	0.19	0.27

sets of cases given in Table 4.2. For the aligned cases with increasing aspect–ratio d increases rapidly while z_o and u_τ increase at first and then seem to reach a plateau. This behavior is not evident for the staggered case where the increase in d is much slower and both z_o and u_τ increase in the range of aspect–ratios considered.

The effect of varying arrangement for a fixed aspect–ratio can be seen for the case of LP06P (Fig. 4.4). The velocity is higher for the aligned case and decreases monotonically as the percentage stagger increases, reaching a minimum for the fully staggered case. With increased staggering, the reduction in sheltering causes an

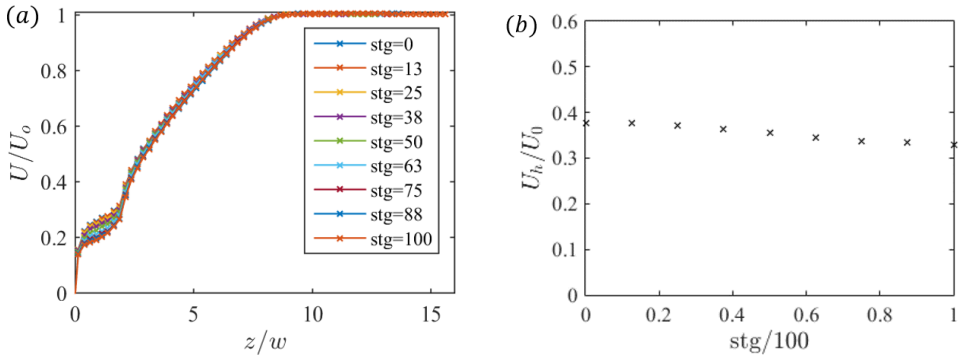

Figure 4.4: Simulation results for percentage stagger case LP06P – (a) Temporal, spanwise and streamwise averaged velocity profiles and (b) Canopy height velocity for the different percentage stagger (stg).

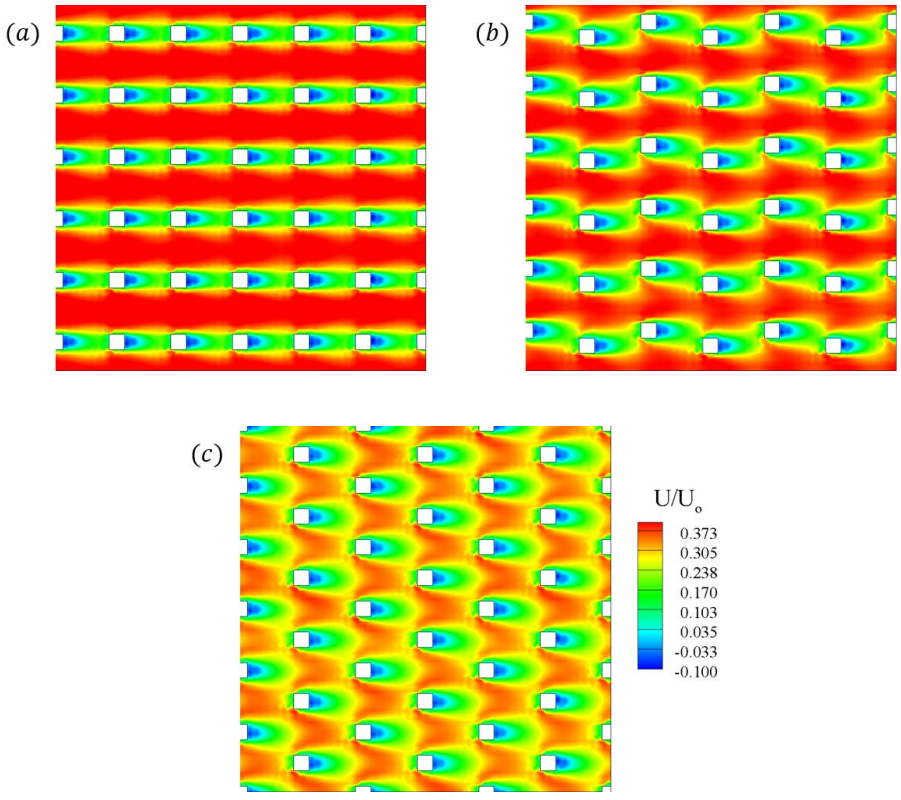

Figure 4.5: Time averaged streamwise velocity contours for the cases of LP06P at a wall normal distance $z/w = 1.625$ at different percentage of staggering. (a) stg = 0 % (aligned), (b) stg = 50 % and (c) stg = 100 % (fully staggered).

Table 4.3: Aerodynamic parameters for the case of LP06P.

stg	z_o/w	d/w	u_τ/U_o	U_h/U_o
0	0.10	1.38	0.08	0.38
12	0.10	1.38	0.08	0.38
25	0.10	1.38	0.08	0.37
38	0.12	1.33	0.08	0.36
50	0.16	1.26	0.09	0.36
62	0.19	1.20	0.09	0.35
75	0.22	1.17	0.10	0.34
88	0.23	1.14	0.10	0.33
100	0.24	1.13	0.10	0.33

increase in the momentum loss to the roughness elements, which leads to an increase of surface drag and reduction of the mean velocity. As the percentage of stagger is increased from 0 % through 100 % (Fig. 4.5) it is seen that the downstream roughness elements move out of the low-momentum region of the upstream element. The high speed channels which exist in between the columns are disrupted for the fully staggered case, and a higher velocity impinges on the roughness elements for this arrangement thereby increasing the drag for the same λ_p. The values for the aerodynamic parameters are shown in Table 4.3 where it can be seen that z_o and u_τ increase as the arrangement changed from an aligned to a staggered one, while the value of d decreases.

4.3 Volumetric Sheltering and Analytical Model

Simulations covering a wide range of parameters such as the ones conducted in this study are computationally intensive, with the current study using more than 1 million CPU hours on various High Performance Computing platforms. While they are becoming more affordable, for many practical applications such as numerical weather prediction, carrying out such simulations at these resolutions might not be a feasible approach. As summarized in Sect. 1.1, this has led to the development of simpler models that can predict the aerodynamic properties of rough surfaces based only on the geometric properties of the roughness, without having to resort to simulations or experiments. A recent such model[63] will be extended below to include applicability to high aspect–ratio roughness elements. A brief description of the model is provided in Sec. 2.2. It was shown that the aerodynamic parameters can be expressed as

$$\frac{z_o}{h} = \left[1 - \frac{1}{1-\exp(-2a)} + \frac{1}{2a}\right] \exp\left[-\kappa/\sqrt{\frac{1}{2a}C_d\lambda_f\left(1-e^{-2a}\right)}\right] \tag{4.1}$$

$$\frac{d}{h} = \frac{1}{1-\exp(-2a)} - \frac{1}{2a} \tag{4.2}$$

$$\frac{u_\tau}{U_0} = \frac{\kappa}{\ln\left(\dfrac{\delta-d}{z_0}\right) + 2\Pi} \tag{4.3}$$

$$\frac{U_h}{u_\tau} = \sqrt{\frac{1}{C_d\lambda_f}}\left[\frac{2a}{1-\exp(-2a)}\right] \tag{4.4}$$

$$a = \frac{a_o}{1-\dfrac{h}{h_s}} \tag{4.5}$$

with the value of C_d, κ, δ and Π as the inputs. The shaded height h_s is computed geometrically using a parameterization of the low momentum region behind a roughness element (see Sec 2.2 and Ref. 63). This shape is controlled by the ratio of the turbulent velocity scale u_τ to the convective velocity scale U_h, and the angle of the shading volume is parameterized as $\tan\theta = C_\theta u_\tau / U_h$. For low aspect–ratio elements, the shape of the shaded region is controlled by the vertical mixing, whereas for the high aspect–ratio elements it is expected that the horizontal mixing will dominate. This will lead to a spanwise expansion of the sheltering region behind the element followed by a contracting region as the deficit reduces in magnitude. This is illustrated using the velocity contour plot in Fig. 4.6a from the simulations and also evaluation of a self-similar velocity distribution of a classic 2–D plane wake in Fig. 4.6b. The plane wake solution[141] is given by

$$\begin{aligned} \frac{U}{U_\infty} &= 1 - \frac{U_s}{U_\infty} \exp\left[-0.637\left(\frac{y}{L_o}\right)^2 - 0.056\left(\frac{y}{L_o}\right)^4\right] \\ \left(\frac{U_\infty}{U_s}\right)^2 &= A\frac{x - x_o}{2\theta}, \quad \left(\frac{L_o}{\theta}\right)^2 = B\frac{x - x_o}{2\theta} \end{aligned} \tag{4.6}$$

where U_∞ is the freestream velocity, U_s is the center-line wake deficit, L_o is the half-width (where $U = U_\infty - 0.5U_s$), while x_o is the virtual origin of the wake and θ is the momentum thickness. The value of A and B are taken from Ref. 141 for a cylinder. Note that this self–similar solution is not strictly applicable for the near wake but does show qualitatively the behavior in this region. The black lines (corresponding to levels

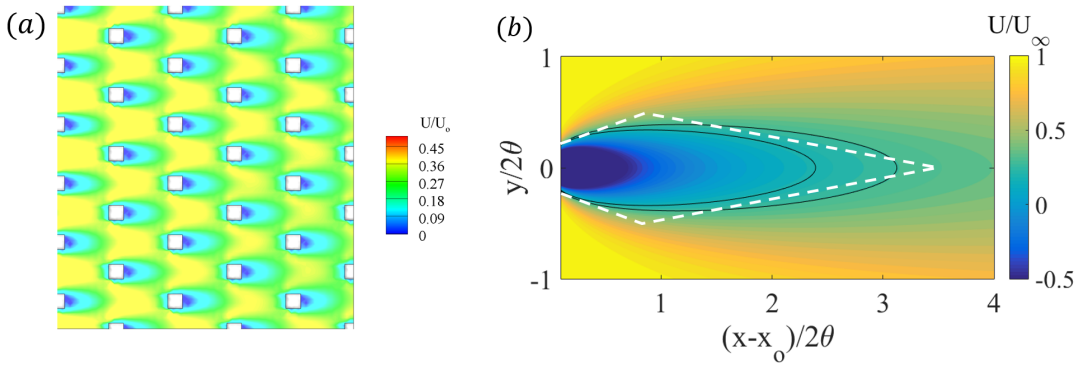

Figure 4.6: Contour plot of streamwise velocity for the case of (a) LP06S-AR6 at $z/w = 0.98$ and (b) for the case of a self similar plane wake. The black lines are the contour levels corresponding to 0.2 and 0.3 times the mean free-stream velocity. The white dashed lines show the linear projections of the simplified shaded region.

of U/U_∞ of 0.2 and 0.3) illustrate qualitatively a boundary between low–momentum regions in the wake and higher momentum regions whose precise location will depend on the threshold. To perform analytical evaluation of the sheltering region, as a next step, the region is approximated using a piece-wise linear description, shown as the rhomb-shaped region using the white dashed lines in Fig. 4.6b. In order to select the appropriate length scales of the rhomb-shaped region, it is assumed that the extent of spanwise spread is on the order of the cross-section scale w. i.e $l_w = cw$ where c should be of $O(1)$. By requiring a match with the aspect–ratio 1 case we obtain $c = 1$, giving $l_w = w$. This further determines $l_c = 1.5 l_e$.

For simplicity, it is assumed that for large aspect–ratios, the parameter C_θ is simply set to $C_\theta = 1$, that is to say, that the growth-rate of the sheltered region is given by the ratio of prevailing turbulence velocity as measured by u_τ, and the prevailing horizontal advection velocity U_h. For low-aspect–ratios ($h < w$), it was

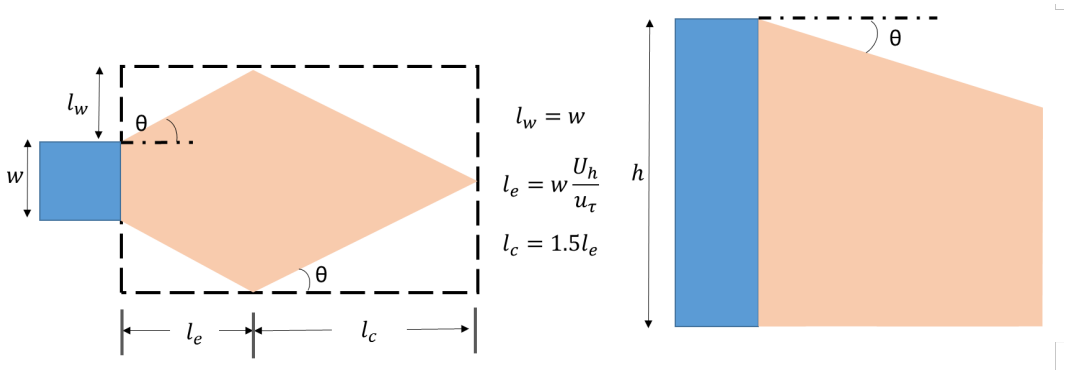

Figure 4.7: The modified sheltering volume for high aspect–ratio elements.

argued that the coefficient should be decreased[63] due to reduced vertical mixing near the wall according to Eq. 2.22. Combining both trends, the following model is used for the growth parameter:

$$C_\theta = \max\left[\left(\frac{2h}{3w} + \frac{1}{3}\right), 1\right] \tag{4.7}$$

so that it is valid for any aspect–ratio. With this value of C_θ this modified model also matches the earlier model for the cube giving a model that is now continuous with the variation of aspect–ratio and is applicable for any aspect–ratio.

This shading model is now used in conjunction with the arrangement of the roughness elements to calculate the shading height which allows determination of the attenuation coefficient using Eq. 2.21. This value of attenuation coefficient can then be substituted in Eqs. 2.16 and 2.17 to obtain the model predictions for z_o and d. With these known, U_h and u_τ can be calculated using Eqs. 2.19 and 2.20 thus predicting the full mean flow response for the given arrangement of the roughness elements on

the surface. In the next section the predictions from the model will be discussed, along with some connections between the arrangement and the flow behavior. The predictions will also be compared against the simulation results.

4.4 Model predictions and Comparisons with Simulation Data

In order to explore model behavior and trends as a function of roughness element aspect–ratio, model predictions for the case of aligned cubes at one particular λ_p of 0.11 are shown in Fig. 4.8. The model uses a value of $C_d = 1$, and the boundary layer thickness is not a required input for predicting z_o and d. From the model results, it can be seen that z_o/w increases rapidly with an increase in the aspect–ratio (AR) as expected (Fig. 4.8a) because of the additional drag produced by the increased height of the elements. However these taller elements also cause an increased sheltering effect leading the z_o/w growth to saturate around an aspect–ratio of 6. This means that after this point the canopy is very deep, and a further increase in the depth is no longer felt by the flow above the canopy. A related trend is observed in the zero–plane displacement d. It can be seen that d/w at high aspect–ratios scales linearly with height h while the relative scaled height $(h - d)/w$ plateaus similar to the behavior seen for z_o/w. This effect as predicted by the model can be illustrated for a moderate or large λ_p case using the sketch in Fig. 4.9. The lighter hatched region is the shaded

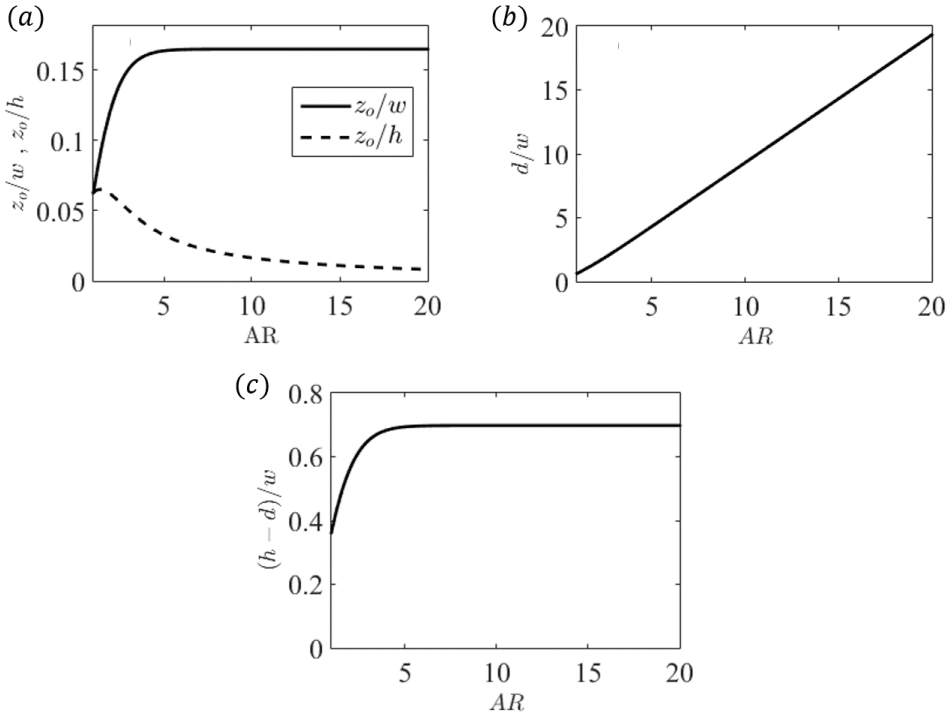

Figure 4.8: Model predictions of roughness length z_0, displacement height d and relative height $h-d$ for various aspect–ratios ($AR = h/w$) for an aligned arrangement, with $\lambda_p = 0.11$.

or "inactive" area while the darker solid region is the unshaded area. As aspect–ratio increases, initially the unshaded area increases as compared to the lower aspect–ratio cases, and this leads to an increase in z_o. However after a point, the increase in shading means that any further increase in aspect–ratio will not lead to an increase in the "active" area (i.e. exposed to the flow, contributing to drag). This means that for the outer flow, the roughness is in effect similar to a shorter roughness element on a higher virtual ground. This suggests that for high aspect–ratio roughness elements, h may not be an appropriate measure to determine the effects of roughness elements on the mean flow, but that $(h - d)$ should be used instead.

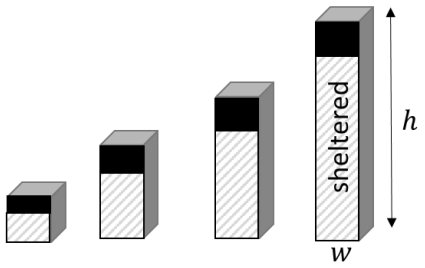

Figure 4.9: Schematic showing the sheltered (dashed) and effectively exposed (dark) frontal area of a roughness element with increasing aspect–ratio, for a surface with aligned elements and a given moderate to high λ_p for which sheltering is important.

The effect of aspect–ratio can be clearly seen by running the model for the parameter space between aspect–ratios 1-20 and λ_p from 0.01 to 1 for the aligned case. Figure 4.10a shows the predicted z_o as a contour plot. Figure 4.10b are slices at constant aspect–ratio extracted from Fig.4.10a. From the contours, it is evident that at higher λ_p, the sensitivity to increase in AR is reduced. This is because high λ_p arrangements are highly sheltered even at low aspect–ratios, and the plateau in z_o occurs rather quickly. This can also be seen in Figs. 4.10a and b. Beyond $\lambda_p > 0.4$ there does not seem to be any effect of aspect–ratio. For values of $\lambda_p < 0.2$ the aspect–ratio has an appreciable effect but not beyond $AR > 7$. Plotting z_o as a function of λ_f, produces no apparent collapse of the profiles (Fig.4.10c). This implies that in the model the frontal area ratio is not an appropriate parameter to characterize the response even if the arrangement remains the same. At high aspect–ratios the "effective" frontal area scales with λ_p as discussed earlier and is the reason the collapse of the profile for the high aspect–ratio cases occurs in Fig 4.10c. Another interesting effect in increasing

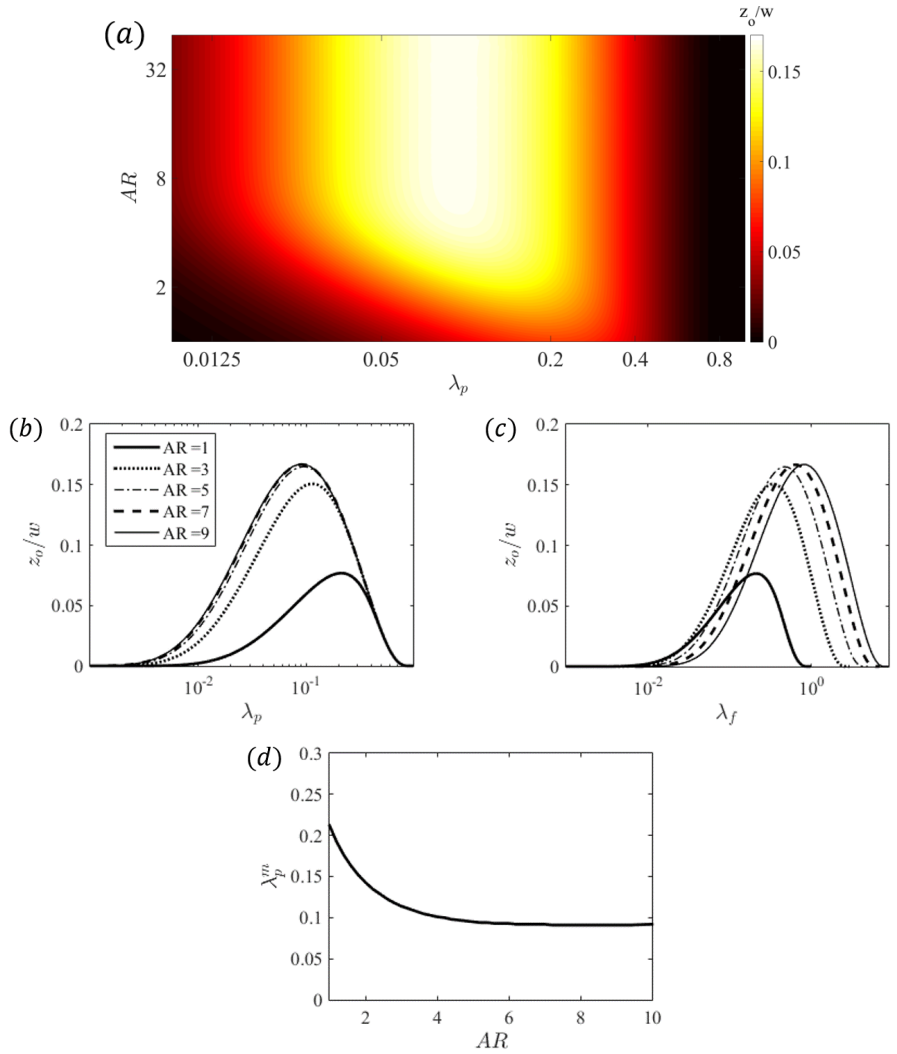

Figure 4.10: (a) Contour map of model z_o prediction as function of λ_p and aspect–ratio for an aligned arrangement of rectangular prism elements. (b) Various horizontal slices from (a) are extracted to better illustrate the variation of z_o with respect to aspect–ratio. Each line corresponds to a different value of the aspect–ratio. (c) Variation of z_o as a function of λ_f for various aspect–ratios. (d) Plan area density at which z_o peaks, λ_p^m as a function of the aspect–ratio.

the aspect–ratio is that the packing density at which z_o peaks (λ_p^m) shifts to the left with increasing aspect–ratio, until $AR = 5$, and is then constant. This is illustrated in Fig.4.10d, where for aspect–ratio 1, $\lambda_p^m \approx 0.2$. As aspect–ratio increases this value decreases and beyond aspect–ratio 5 becomes a constant value close to $\lambda_p^m \approx 0.1$. This is also a manifestation of the increased sheltering. The peak in z_o happens due to the competing effects of drag increasing as more elements are added in a given area and the decreased efficacy of these elements to cause drag due to the mutual sheltering effects. At higher aspect–ratios there is of course an increase in the sheltering effect causing the peak λ_p to shift to lower values. The model suggests that the plateauing behavior should be observable in the simulations, since the simulated cases have aspect–ratios up to 7.

Next, the model predictions are compared against results from the LES. To process the simulation results the time-mean streamwise velocity is averaged in the spanwise and streamwise directions within two rows. Since this is a developing flow, there are small differences in the streamwise direction from one row to the next. The streamwise location for which results are compared to the model is chosen such that the boundary layer height is similar ($\delta - h \approx 7w$) for the different cases to allow for a clear comparison of the friction velocity. There are three unknown parameters to be determined (d, u_τ and z_o). In order to reduce the uncertainty when attempting to obtain a 3-parameter fit to the data, d is determined from the model,[22] and is used to determine the friction velocity u_τ (slope) and z_o (intercept) from the fits.

The value of for the von–Karman constant $\kappa = 0.4$ as discussed in Sect. 2.2. The values of δ given as input to the model for the five sets of cases are specified in the form $\delta/w = c - h/w$ with the value of c being 7.2 for LP06A and LP11A, 6.8 for LP25A, 7.4 for LP06S and 6.6 for LP06P to match the corresponding values for the LES results. The resulting log-law fits are shown in Fig. 4.11 for the 5 sets of cases - LP06A, LP11A, LP25A, LP06S and LP06P. For the $\lambda_p = 0.06$ and 0.11 aligned cases, the profiles indicate a noticeable difference (increase in z_o) between the $AR = 1$ and 2 cases, with a smaller difference among these for the $\lambda_p = 0.25$ case. In Figs. 4.12, 4.13 the LES results are compared with the model predictions for the aligned cases, and in general the predictions match the simulations fairly well, both in the trends as well as quantitative details. It is observed that both $\lambda_p = 0.06$ and 0.11 have similar values for the maximum value of z_o of around $0.15w$ which is about 3 times the value for the cube case ($AR = 1$). It is also seen that LP06A reaches a plateau more slowly than the LP11A case. This is an indication of the difference in sheltering, with lower plan area ratio surfaces exhibiting reduced sheltering due to the increased spacing among elements. This is further evidenced by the results for case LP25A which has not much variation for $AR > 2$ indicating strong sheltering effects.

Figure 4.13 shows that the trends for u_τ are also predicted well by the model. The modeled friction velocity (and results from LES) initially increase with aspect–ratio and then plateaus earlier than z_o. One notices that the results (solid line) have a vertical shift between the model and simulations even if the model predicts the

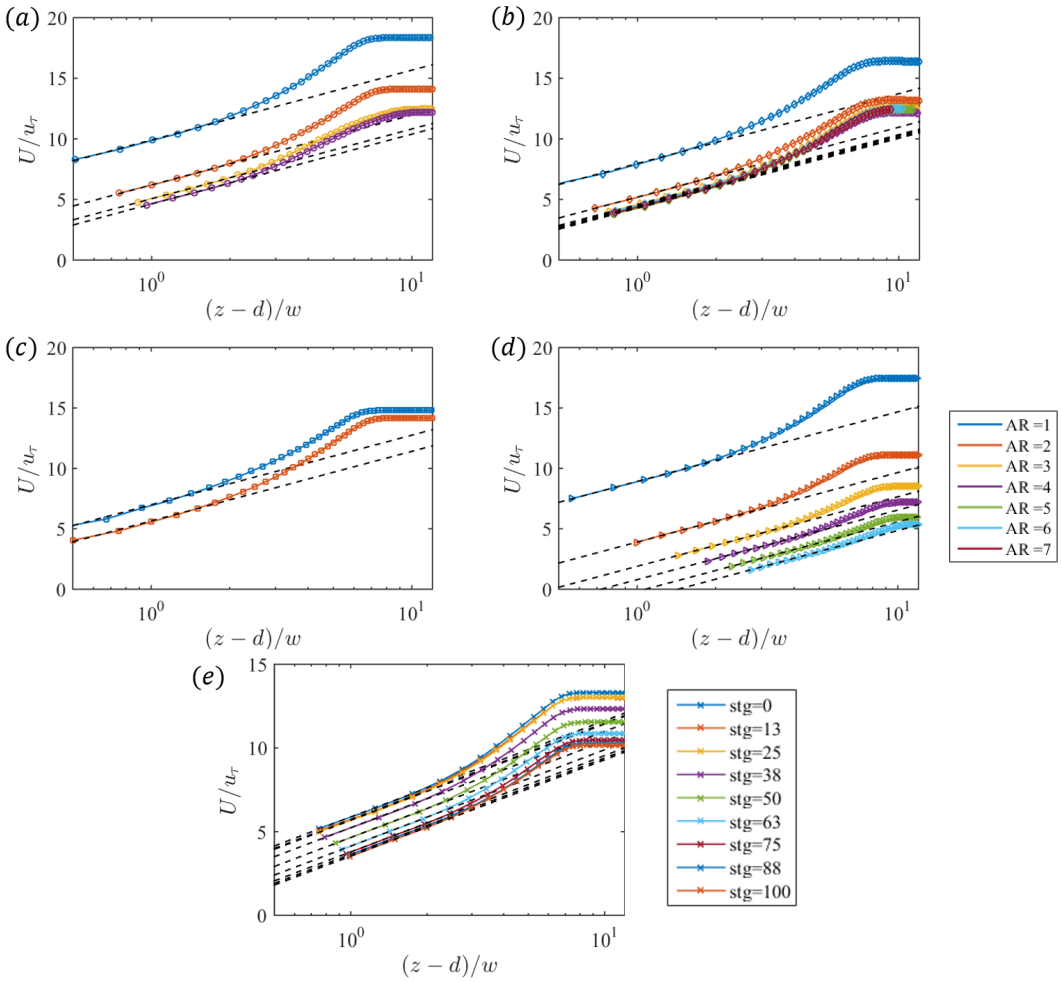

Figure 4.11: Log-linear plot of the mean velocity profiles from LES (symbols), normalized with the fitted value of u_τ so all fits (dashed lines) have the same slope of $1/\kappa$. The line's x-intercept ($U/u_\tau = 0$) is $(z_o - d)/w$ using the fitted value of z_o. Profiles are shown for 4 sets at various aspect–ratios: (a) LP06A (b)LP11A (c)LP25A (d)LP06S and also for the $AR = 2$ case for various staggering ratios, shown in (e) case LP06P.

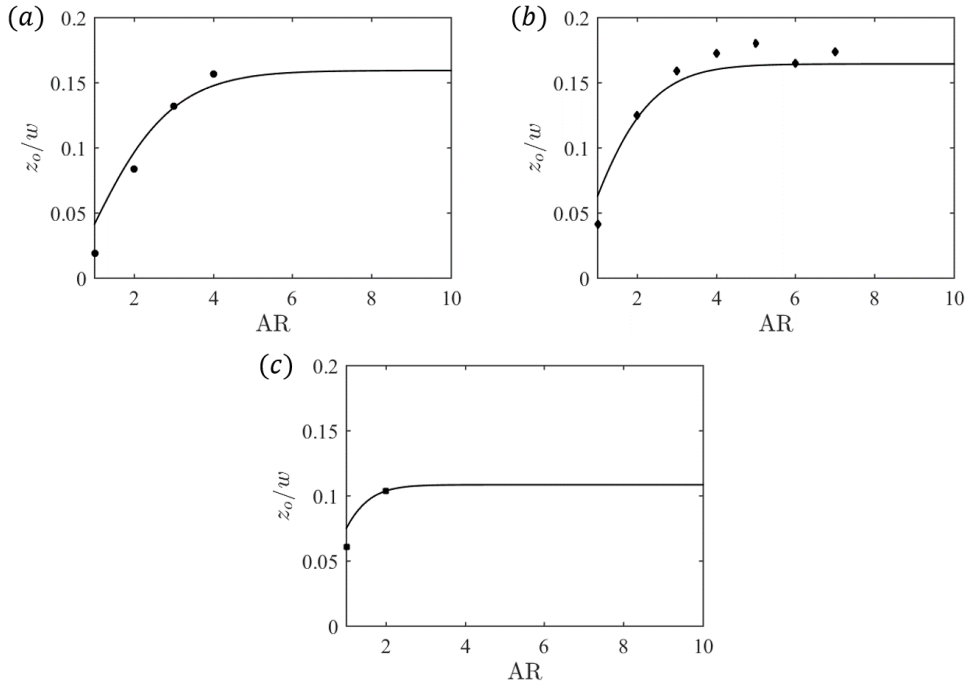

Figure 4.12: Comparison of z_o between the LES and the model for (a) LP06A, (b) LP11A and (c) LP25A. Symbols are the LES data and the lines are the model predictions.

trend correctly. To calculate u_τ and U_h, the model requires specification of the wake correction parameter Π. There is currently no theoretical framework for obtaining the value of Π a-priori. The results shown in solid lines use a value of 0.2 as is used in Ref. 63. Calculating Π for the different cases from the simulation profiles gives, on average, a value of Π closer to 0.5 for the higher λ_p cases. If this value of Π is used to recalculate the friction velocity for the three cases (Fig.4.13, dashed lines), it can be seen that the model is closer to the data. However it should be noted that absent a framework for calculating Π without simulation data, in practice one has to use a specified value of Π.

Next the fully staggered case is examined which is important due to two reasons

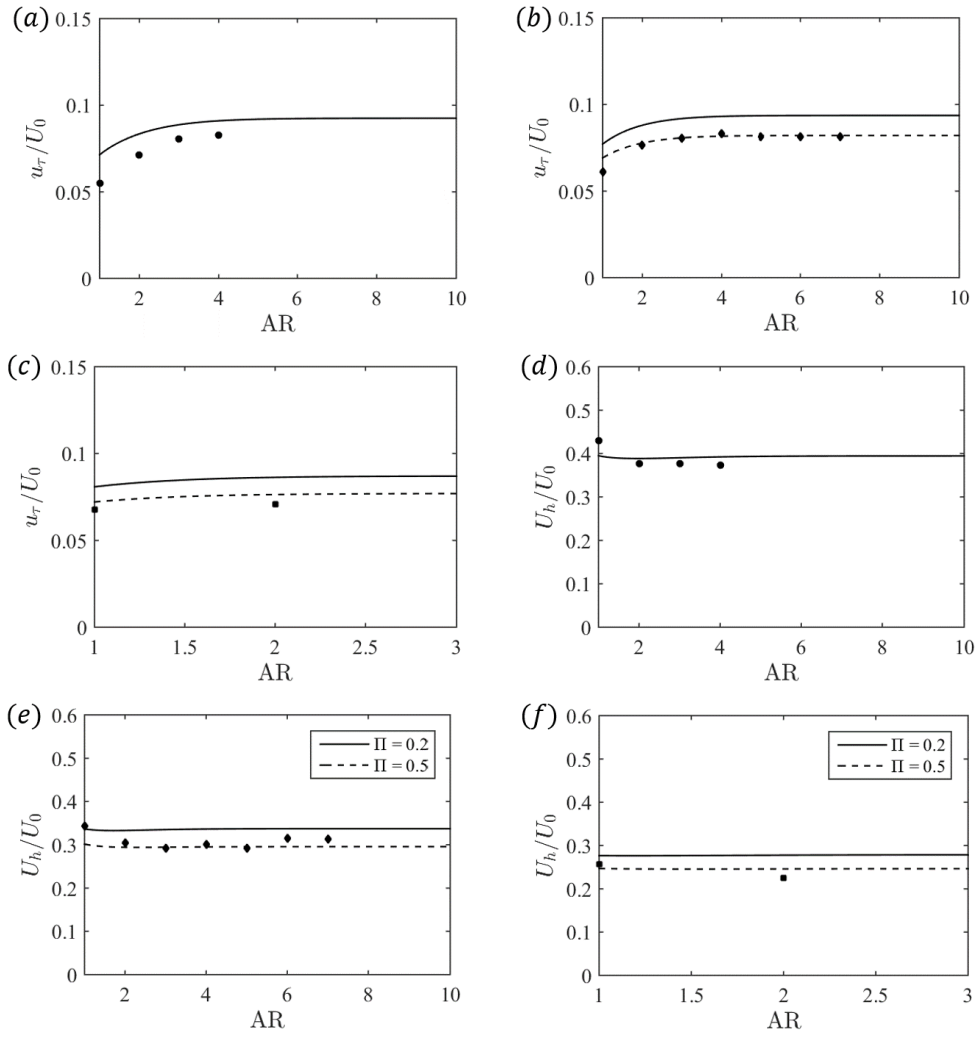

Figure 4.13: u_τ comparison – simulation (symbols) and model predictions (lines) for (a)LP06A (b)LP11A and (c)LP25A. (d)-(f) are the corresponding plots for U_h.

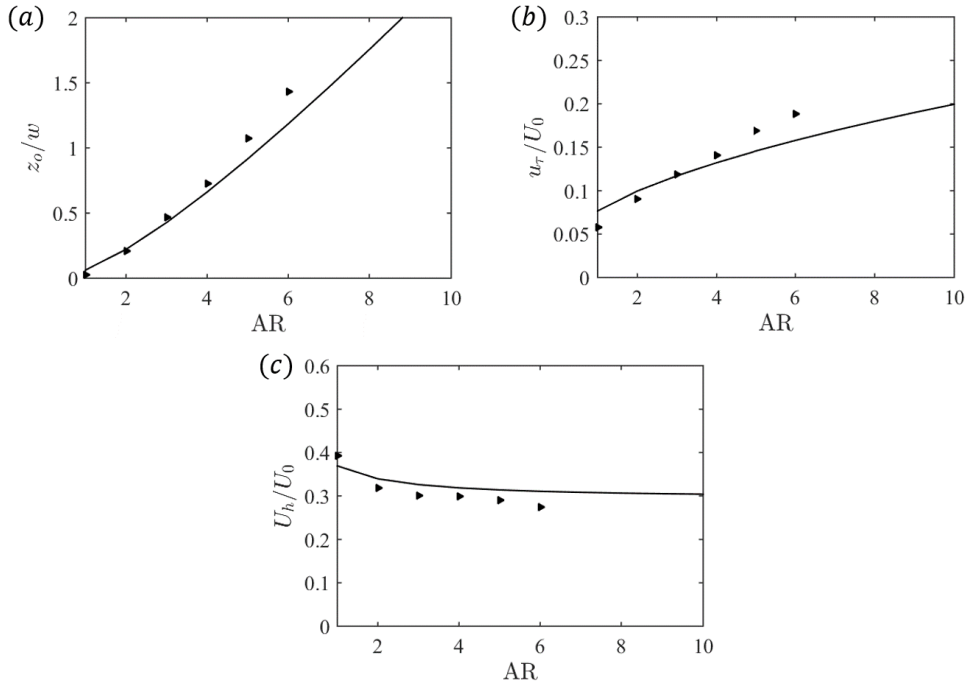

Figure 4.14: comparison between simulation (symbols) and model prediction (line) for LP06S (a)z_o (b)u_τ and (c)U_h.

- staggering inherently generates less sheltering as was explained in Sect. 4.2 and illustrated using Fig. 4.5, and thus one expects that variations with aspect–ratio should be appreciable. Furthermore, it is an important validation for how well the model captures the spanwise interactions between the roughness elements. Figure 4.14 shows that the expected stronger sensitivity to AR is indeed reflected in the simulation data. It is also evident that compared to the corresponding aligned case where z_o became independent of the aspect–ratio at around $AR = 5$, for the staggered cases it continues to increase for the range of aspect-ratio simulated. As mentioned before, this is not very surprising since staggering implies a weaker shading effect as discussed earlier. The simulation results also agree qualitatively with the model as

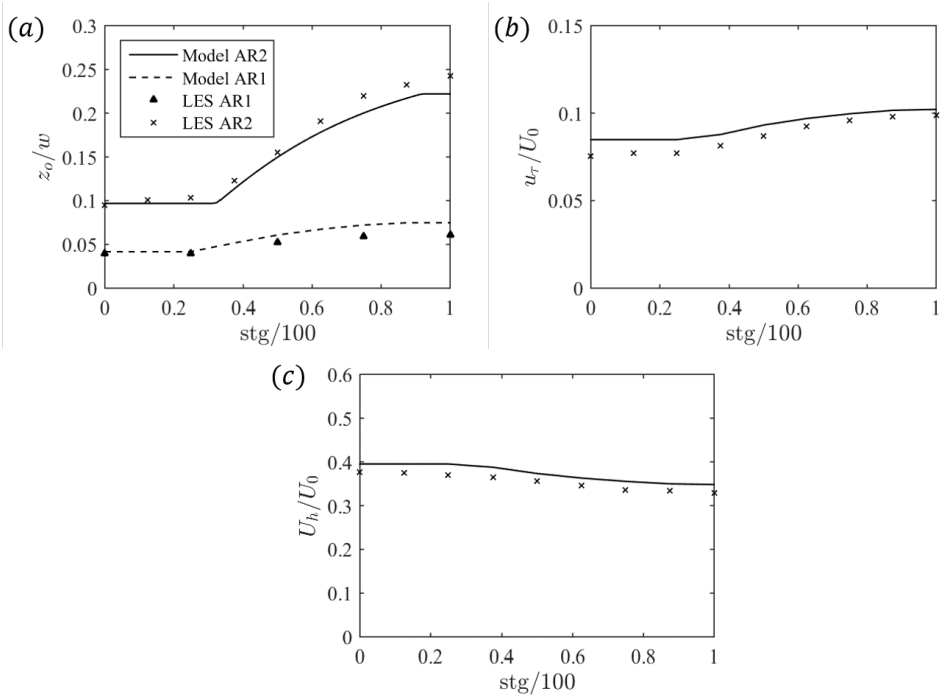

Figure 4.15: comparison between simulation and model for LP06P (a)z_o (b)u_τ and (c)U_h. Results of z_o for $AR = 1$ case also plotted for comparison.[142]

z_o increases in the range of AR between 1 and 6 (Fig. 4.14a). A similar increasing trend is also observed in the friction velocity u_τ (Fig. 4.14b), while the canopy height velocity U_h appears to be decreasing slowly (Fig. 4.14c). The model does not predict a plateauing of z_o at this plan area ratio for the fully staggered arrangement. The last set of cases (LP06P Fig. 4.15) illustrates the effect of changing the staggering while keeping both λ_p and the aspect–ratio constant. Here the value of λ_p and AR are fixed ($\lambda_p = 0.06$ and $AR = 2$), and the arrangement of the elements is modified by shifting them from a fully aligned case to a fully staggered one (as illustrated in Fig. 4.5), in increments of 12.5%. The effective roughness height (z_o) follows a behavior similar to that of the case for $AR = 1$ as seen in Ref. 142. It is to be noted that

staggering does not have a discernible effect on z_o or u_τ until reaching 25 % stagger. From this point onwards, there is a significant increase in z_o as the elements move away from the sheltered region and become more effective drag generators, reaching a maximum at the fully staggered configuration. The model predictions match the simulation results quite well.

4.5 Summary

Wall modeled large–eddy simulations and a phenomenological sheltering model have been used to explore the effect of varying the aspect–ratio and arrangement of rectangular prism shaped roughness elements on the mean velocity profile of turbulent boundary layer flow. The LES show that for aligned configurations, increasing aspect–ratio leads to greatly increased sheltering, and the flow response becomes independent of the aspect–ratio quite rapidly, for example around an AR of 4 for the LP11A case. A previously proposed model[63] is extended for applicability to high aspect–ratio roughness elements. The model performs well in predicting the mean flow properties and aerodynamic parameters of the surface which are obtained from LES. The model predicts that at high λ_p, the flow response in the aligned case will become independent of the aspect–ratio. The sheltering effect also increases at increased values of λ_p consistent with the expectation of increased sheltering between the elements at higher packing densities. The independence of the flow response to aspect–ratio, however, does not happen for the staggered arrangements wherein there is less sheltering and

the effect of aspect–ratio on the aerodynamic parameters persists for higher values of the aspect–ratio. While simulations up to an aspect–ratio of 6 confirm the model predictions that the aspect–ratio has an appreciable effect on the flow in that range, further validation of this effect is needed via simulations or experiments. However simulations at very high aspect–ratios are still a challenge due to large computational requirements.

In conclusion, the analytical model developed and tested here appears promising as a tool to provide rapid and reasonably accurate predictions of aerodynamic roughness properties of surfaces based only on geometric information. Several limitations of the LES and the model should be kept in mind, however. First, the LES presented here use relatively coarse resolutions. This means that the resulting mean velocity distributions especially within the canopy layer can be expected to be smeared out especially if one compares with high resolution Direct Numerical Simulations such as those presented in Ref. 26. The latter show sharper mean velocity profiles near the top of the roughness elements compared to typical profiles obtained in the present LES. However, from the point of view of overall momentum dynamics, mean drag forces and the mean logarithmic profile above the roughness elements, the lower resolution LES used here are expected to be sufficiently accurate and enable coverage of a large number of cases and geometries. Only by covering a large number of cases could the roughness model be meaningfully tested. Second, in terms of the model itself, it is important to stress that it is only applicable to flow over rectangular prism

geometries. To apply the model to general surfaces characterized by an arbitrary height distribution $H(x, y)$ the present model will have to be extended significantly. Although this analytical method is very powerful and has the potential of wide applicability, its application is limited to cuboidal roughness elements. In Appendix A an attempt will be presented, to extend this model to more general surfaces using the understanding that has been gained through these studies. In the next chapter an explicit relation will be developed based on the analytical method. This explicit relation will explore a methodology to predict the mean flow response directly from the geometric parameters without need for iterative procedures.

Chapter 5

An Explicit Analytical Roughness Model for Surfaces with Cuboidal Roughness Elements

This chapter investigates the possibility of developing an explicit analytical model to connect the flow properties to the surface morphology. The rough wall model presented in Sec. 2.2 shall be the basis for the proposed explicit model, and as such this discussion is restricted to cuboidal roughness elements with canonical arrangements. The more simplified explicit relations developed will be in the spirit of the engineering correlations presented in Sec. 1.1.1. In Sec. 5.1, an overview of the method to develop the simplified relation for all the cases will be presented. Sec. 5.2 develops

the simplified relation between flow parameters and the geometry for various cubic roughness element arrangements. The predictions from these relations are compared against data from the experiments and simulations from the literature. In Sec. 5.3 data from the various cases will be shown to collapse on a single curve predicted by the developed relation.

5.1 A Simplified Approach Relating Flow Parameters to Roughness Morphology

As a starting point consider the two–layer model for the velocity profile similar to that used in Yang et. al.[63] and explained in detail in Sec. 2.2.

$$\begin{aligned} U &= U_h \exp\left[a\left(z/h-1\right)\right], && 0<z<h; \\ U &= u_\tau/\kappa\left[\ln\left(\frac{z-d}{z_o}\right)+W(z/\delta)\Pi\right], && h\le z<\delta; \end{aligned} \tag{5.1}$$

The flow parameters can be expressed in terms of the attenuation coefficient a (see Sec. 2.2) as

$$\frac{z_o}{h-d} = \exp\left[-\kappa\Big/\sqrt{\frac{1}{2a}C_d\lambda_f\left(1-e^{-2a}\right)}\right] \tag{5.2}$$

$$\frac{d}{h} = \frac{1}{1-\exp(-2a)} - \frac{1}{2a} \tag{5.3}$$

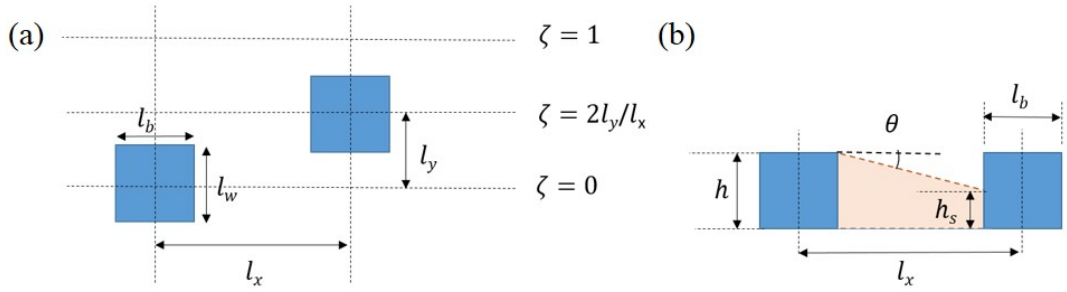

Figure 5.1: Top view showing the arrangement of roughness elements and side view showing a simple representation of the reduced momentum region. h_s is the height of the sheltered layer

Note that these equations are valid for elements with a constant sectional frontal area $dA_f(z)$ as a function of the wall distance z. The exponential profile attenuation coefficient determines the shape of the profile inside the canopy, and it in turn depends on the detailed interactions between the roughness elements. As before, the attenuation coefficient must be connected to the geometry of the rough surface, and the approach outlined in Secs. 2.2 and Sec. 4.3 is followed. Figure 5.1 shows an example arrangement of roughness elements. If a linear attenuation of the sheltering region in the stream-wise direction is assumed, the unsheltered height $h - h_s$ depends on the angle of sheltering θ, the distance between the elements (l_x in streamwise and l_y in the spanwise directions) and the geometry of the sheltering elements (l_b, l_w, h), i.e.

$$h - h_s \quad = f(\theta, l_x, l_y, l_b, l_w, h). \tag{5.4}$$

It can be seen from the sketch in Fig. 5.1 that the unsheltered height will typically be a linear function of $\tan\theta$ and the specific geometry. Furthermore if we assume that

the dependence can be factored into a factor that depends on the size of the elements and their separation distances and height. This can be used to write

$$h - h_s \quad = C(\zeta) L_\lambda(l_x, l_b) \tan\theta. \tag{5.5}$$

The effect of the parameters can be simplified from the understanding that the dominant effect is the distance between the elements $L_\lambda = l_x - l_b$, where l_x is related to the solidity through $\sqrt{\frac{hl_w}{\lambda_f}}$. The remainder of the roughness element arrangement is characterized through a non-dimensional factor $C(\zeta)$, which gives the effect of the two–dimensional placement of the elements. This factor can be characterized using the ratio of the distances $\zeta = 2l_y/l_x$. A factor of two is used to have $\zeta = 1$ for a fully staggered arrangement. An expression for $C(\zeta)$ in terms of ζ will be derived in Sec. 5.2.3. Thus

$$\begin{aligned} h - h_s &= C(\zeta) \left[\sqrt{\frac{hl_w}{\lambda_f}} - l_b \right] \tan\theta \\ 1 - h_s/h &= C(\zeta) \left[\sqrt{\frac{l_w}{h\lambda_f}} - \frac{l_b}{h} \right] \tan\theta \\ 1 - h_s/h &= C(\zeta) C_\lambda \tan\theta \end{aligned} \tag{5.6}$$

Here $C(\zeta)$ encodes the effect of the arrangement or "phase" of element distribution and $C_\lambda = \sqrt{\frac{l_w}{h\lambda_f}} - \frac{l_b}{h}$ the effect of the streamwise distance between the elements or "amplitude" of the distribution . The angle θ determines how fast the wake is smeared, and so $\tan\theta$ is a function of the element shape and the ratio of u_τ, the

friction velocity and U_h the convective velocity.[63] This gives

$$\tan\theta \;\; = C_\theta(l_w/h)\frac{u_\tau}{U_h} \tag{5.7}$$

with C_θ only a function of l_w/h since the shape of the wake is controlled by the dimensions normal to the flow and the expression for C_θ is $\max(1/3 + 2h/3l_w, 1)$ as shown in Sec. 4.3. The attenuation factor a is expressed as

$$a = \frac{a_o}{1 - h_s/h}. \tag{5.8}$$

Note that this equation is valid only for the case of a roughness element having a constant sectional frontal area $dA_f(z)$. For elements with varying cross sectional area this expression would be modified depending on the shape of the element and would have to be calculated by performing the momentum balance in the unsheltered area.

Substituting Eq. 5.7 and Eq. 5.6 into Eq. 5.9,

$$\begin{aligned} a \;\; &= \frac{a_o}{C(\zeta)C_\lambda C_\theta \dfrac{u_\tau}{U_h}} \\ a \;\; &= \frac{a_o}{C_\gamma}\frac{U_h}{u_\tau} \end{aligned} \tag{5.9}$$

where $C_\gamma(\lambda_f, l_w/h, l_b/h) = C(\zeta)C_\lambda(\lambda_f, l_w/h, l_b/h)C_\theta(l_w/h)$, which depends on the shape of the roughness element, the frontal area ratio and the arrangement. Using Eq. 5.9, the attenuation coefficient is represented as a function of the geometry.

To obtain an expression for the ratio u_τ/U_h consider the momentum balance, which gives Eq. 5.10 which is again valid for the case of elements with a constant sectional frontal area.

$$\frac{U_h}{u_\tau} = \sqrt{\frac{1}{C_d \lambda_f}} \left[\frac{2a}{1 - \exp(-2a)} \right] \tag{5.10}$$

Upon substituting into Eq. 5.9 and simplifying

$$\begin{aligned} a\left[1 - \exp(-2a)\right] &= \frac{2a_o^2}{C_\lambda^2 C(\zeta)^2 C_d \lambda_f} \\ &= \frac{2a_o^2}{C_\lambda'^2 C(\zeta)^2 C_d} \end{aligned} \tag{5.11}$$

where $C_\lambda' = C_\lambda \lambda_f^{-1/2}$, while that for $C(\zeta)$ will be shown in Sec. 5.2.3. The RHS is termed K_a, which is a geometric parameter which captures the amount of sheltering present for a given arrangement. So now Eq. 5.11 becomes

$$a\left[1 - \exp(-2a)\right] = K_a. \tag{5.12}$$

This expression for K_a is valid for elements with constant sectional frontal area. This chapter explores the application of this equation for the case of cubic roughness–element arrays of various packing densities and different arrangements – aligned, staggered, various percent stagger and different roughness–element orientations.

For a given value of K_a, the implicit relation in Eq. 5.12 has to be solved iteratively till convergence. It can be seen that in absence of the exponential term, it would reduce to $a = K_a$. Thus, it would be interesting to try and express a directly in terms

of K_a i.e.

$$a \;= K_a \; G(K_a) \tag{5.13}$$

where K_a is the initial "guess" solution and $G(K_a)$ is the correction term. So instead of an iterative solution procedure, an explicit relation is obtained using a suitable form of the correction term. In this chapter three different forms of G will be considered - a zeroth order (no correction $G = 1$), first order (from an explicit iteration) and a second order (from a Newton iteration). The three forms are

$$\begin{aligned} G(K_a) &= 1 && \textit{No Correction} \\ G(K_a) &= \left[1 - \exp(-2K_a)\right]^{-1} && 1^{st}\ \textit{order} \\ G(K_a) &= 1 + \frac{\exp(-2K_a)\left(1 - \exp(-2K_a)\right)}{\left(1 - \exp(-2K_a)\right)^2 + 2K_a \exp(-2K_a)} && 2^{nd}\ \textit{order.} \end{aligned} \tag{5.14}$$

Next the expression for a, Eq. 5.13 is substituted into the equations for z_o and d (Eq. 2.17) to obtain

$$\frac{d}{h} \;= \left[\frac{-1}{2K_aG} + \frac{1}{1 - \exp(-2K_aG)}\right]. \tag{5.15}$$

for d and

$$\frac{z_o}{h} \;= \left(1 - \frac{d}{h}\right) \exp\left[-\kappa \; \left(C_d \; \frac{\lambda_f \left(1 - \exp(-2K_aG)\right)}{2K_aG}\right)^{-1/2}\right] \tag{5.16}$$

for z_o. These can be written in the form

$$\begin{aligned} \frac{d}{h} &= \left[G' - \frac{1}{2K_G} \right] \\ \frac{z_o}{h-d} &= \exp\left[-\kappa \left(\frac{C_d \, \Lambda_f}{2} \right)^{-1/2} \right] \end{aligned} \tag{5.17}$$

where $K_G = K_a G$ and $\Lambda_f = \lambda_f (K_G G')^{-1}$ is the geometric parameter on which d and $z_o/(h-d)$ depend respectively. $G' = [1 - \exp(-2K_G)]^{-1}$ can be considered a further correction to G. It is equivalent to a predictor corrector step with the initial guess K_G. Thus z_o and d can be written as a function of purely the geometric property K_a. One important point to note here is that Eq. 5.17 is valid for any arrangement of the roughness elements as long as a form for K_a for the surface can be specified. In the next section this relation is obtained for various systematic arrangement of cubic roughness elements.

5.2 Application to Cubic Rough Surfaces in Various Arrangements

5.2.1 Aligned Cubes

For aligned cubes the sheltering volume is illustrated in Fig. 5.2. The shaded height h_s can be expressed as

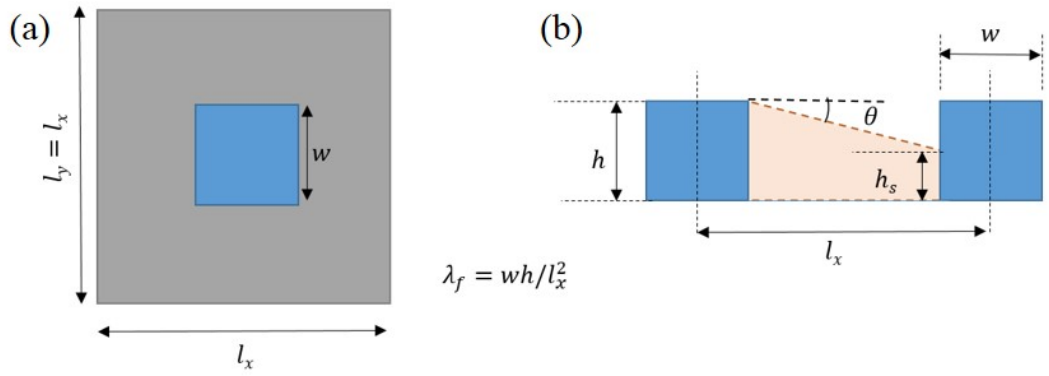

Figure 5.2: Illustration of repeating tile for an aligned arrangement with a frontal area ratio λ_f and the volumetric shading for this arrangement

$$\begin{aligned} h - h_s &= (l_x - w)\tan\theta \\ 1 - \frac{h_s}{h} &= \left(\frac{1}{\sqrt{\lambda_f}} - 1\right)\tan\theta \\ &= \left(\frac{1}{\sqrt{\lambda_f}} - 1\right)\frac{u_\tau}{U_h} \end{aligned} \tag{5.18}$$

where h is the cube height, w is the width of the cube ($w = h$). Thus here we find $C(\zeta) = 1$, $C_\theta = 1$ and $C_\lambda = 1/\sqrt{\lambda_f} - 1$. Substituting for the expression for the attenuation coefficient,

$$a = \left(\frac{a_o\sqrt{\lambda_f}}{1 - \sqrt{\lambda_f}}\right)\frac{U_h}{u_\tau} \tag{5.19}$$

which on substituting the ratio of u_τ/U_h and squaring both sides gives

$$a^2 = \frac{a_o^2}{C_d\left(1 - \sqrt{\lambda_f}\right)^2}\left[\frac{2a}{1 - \exp(-2a)}\right] \tag{5.20}$$

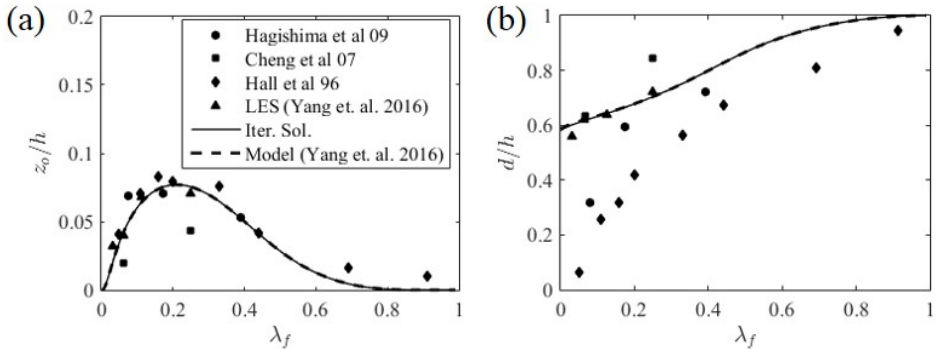

Figure 5.3: Comparison for the fully aligned case of (a) z_o and (b) d predictions from the full iterative solution against measured values from experiments and simulations.

which can be simplified in the form

$$\begin{aligned} a\left[1-\exp(-2a)\right] &= K_a \\ K_a &= \frac{2a_o^2}{C_d\left(1-\sqrt{\lambda_f}\right)^2} \end{aligned} \tag{5.21}$$

where K_a depends only on λ_f. This equation relates the attenuation coefficient a directly to the geometry through the parameter K_a. This equation is easy to solve iteratively, and in this case the same result as Ref 63 for the case of aligned cubes is obtained.

This predicted value of a can now be used to calculate z_o and d (Fig. 5.3). For the case of aligned cubes, the values predicted are the same as those obtained in Ref. 63. The prediction follows the general trend expected for such an arrangement with z_o increasing initially with an increase in λ_f. As λ_f continues to increase, mutual sheltering effects become important, and part of the roughness element is sheltered leading to the elements being less effective at generating drag. The value of z_o peaks

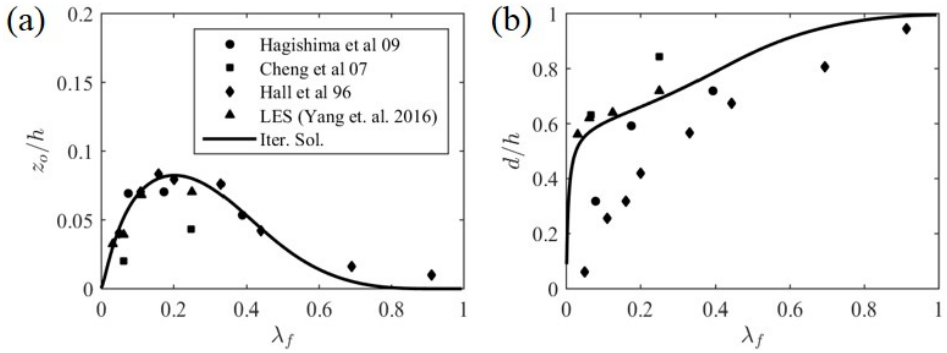

Figure 5.4: Comparison for the fully aligned case of (a) z_o and (b) d predictions from the full iterative solution with the β correction included against measured values from experiments and simulations.

around a value of 0.2 and then decreases as the elements are sheltered from the outer flow. The peak λ_f obtained is similar to the values predicted and measured by other studies in the literature.[10,19,30] The value of d increases monotonically as a function of λ_f and reaches 1 as expected as $\lambda_f = \lambda_p \to 1$. The values of z_o match well with experiments and simulations in the literature while d has more variation but is still within the range given in Ref. 10. One thing to note for d is that in the other limit $\lambda_f \to 0$ d does not go to 0 as expected. This is because the skin friction drag on the surface is neglected which would dominate as $\lambda_f \to 0$. To address this Yang et. al.[63] implemented a drag partition and corrected for this using a β correction. Following the same approach the z_o and d can be written as

$$\begin{aligned} \frac{z_o}{h} &= \left(1 - \frac{d}{h}\right) \exp\left[-\kappa\, C_d\, \lambda_f\, \frac{1-\exp(-2a)}{2a} \left(\frac{1+\beta\lambda_f}{\beta\lambda_f}\right)\right] \\ \frac{d}{h} &= \frac{\beta\lambda_f}{1+\beta\lambda_f}\left[\frac{1}{1-\exp(-2a)} - \frac{1}{2a}\right] \end{aligned} \tag{5.22}$$

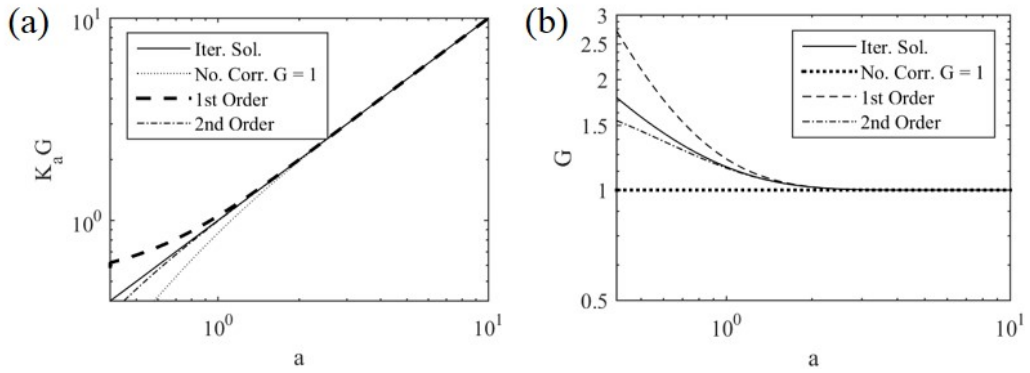

Figure 5.5: (a) Comparison of Predictions from the full iterative solution compared against various corrections $a = K_a G$. (b) Comparison of the different forms of the factor G

with a value of $\beta = 196$ is estimated for cubes.[63] This now gives the correct asymptotic behavior at $\lambda_f \to 0$ as both z_o and d tend to zero.

The different forms of G can now be used to compare how close the explicit correction is to the full iterative solution (Fig 5.5). It can be seen that a becomes equal to K_a at values greater than 2 since the $(1 - \exp(-2a))$ term is active only at low values of a. which is equivalent to a λ_f of around 0.2 for aligned cubes. So at high values of λ_f the correction term is not required, but many surfaces of interest are in the low to moderate ranges of λ_f where $a < 2$. Thus G can be important and it is seen that the second order correction gives a very close prediction to the iterative solution of a, while the first order correction has some differences from the iterative solution at low values of a as expected. This can also be seen in Fig. 5.5b – G becomes close to 1 near a value of $a = 2$, and also the second order correction is very close to predicting the actual value of G.

The asymptotic behavior of these equations for the aligned case can now be

checked. For the lower limit of λ_f, $z_o \to 0$ as $\lambda_f \to 0$ but for the correct behavior of d the β correction should be used as discussed earlier. At high values of λ_f, $G \to 1$, and the equations become

$$\begin{aligned} \frac{d}{h} &= \left[1 - \frac{1}{2K_a}\right] \\ \frac{z_o}{h} &= \frac{1}{2K_a} \exp\left[-\kappa \left(C_d \frac{\lambda_f}{2K_a}\right)^{-1/2}\right]. \end{aligned} \tag{5.23}$$

At the limit $\lambda_f \to 1$ $K_a \to \infty$ and thus $d/h \to 1$ and $z_o/h \to 0$ as expected.

Next the performance of the explicit equation in predicting z_o and d for the entire relevant range of λ_f is checked by comparing against the iterative solution. All three forms of the correction factor G as given in Eq. 5.14 will be used. First, it can be seen that the explicit formula matches the iterative solution very well (Fig. 5.6). For the general trends, even using no correction and simply taking $G = 1$ produces a good result. The differences between the different specifications for G are quantified by using z_o predicted using Eq. 5.17 (z_o^e) and the iterative solution method (z_o^i) to compute the relative difference ($|1 - z_o^e/z_o^i|$) which is shown in Fig. 5.6b and expressed as a percentage. It is seen that the deviations are highest for the case without correction, with the difference decreasing as λ_f increases. Even for this case the difference is less than 20% at $\lambda_f > 0.1$. The first–order correction matches more closely with the difference between it and the iterative solution becoming $< 10\%$ at $\lambda_f > 0.1$. Lastly the second–order correction matches the iterative solution pretty

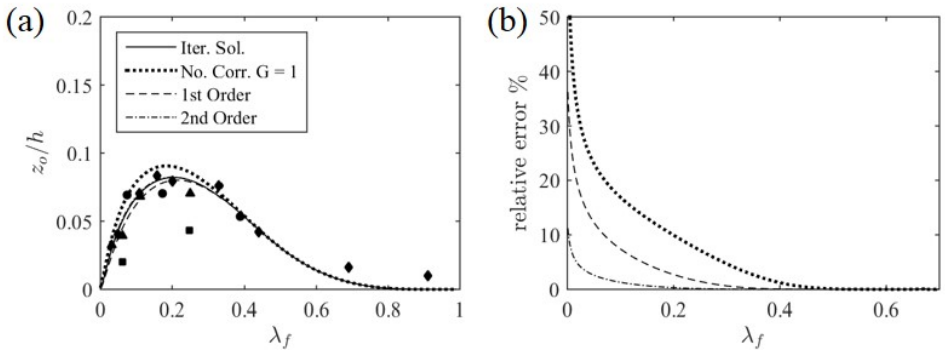

Figure 5.6: Comparison for the fully aligned case of (a) z_o from the full iterative solution against predictions from explicit corrections. (b) a measure of the relative difference in the predicted z_o using the correction as opposed to the full iterative solution.

closely with a very small difference ($< 10\%$) at low values of λ_f where z_o is very small anyways, and the differences are smaller at larger λ_f. One thing to note here is the iterative solution is a solution to an already simplified model, and although it is possible to match it as closely as required using different forms of G, we must keep in mind that it is not the absolute truth. All the forms of G that are used even the one without a correction term ($G = 1$) do give estimates of z_o which are within the range of the measured values from experiments and simulation values and give very similar and realistic trends.

Using the explicit equation, quick and accurate predictions of the flow response can be made which capture the trends correctly. It shows z_o increasing up–to $\lambda_f \approx 0.2$ and then decreasing as λ_f is increased further due to sheltering. Here since an equation that connects the geometry to z_o is obtained, this behavior can be shown explicitly.

From Eq. 5.17 and taking $G = 1$

$$\begin{aligned} \frac{z_o}{h-d} &= \exp\left(-\frac{2\kappa a_o}{C_d}\frac{1}{\sqrt{\lambda_f}\left[1-\sqrt{\lambda_f}\right]}\right) \\ \frac{z_o}{h-d} &\sim \exp\left[-\left(\lambda_f\left[1-\sqrt{\lambda_f}\right]^2\right)^{-1/2}\right]. \end{aligned} \tag{5.24}$$

This equation shows explicitly the two terms that encapsulate the competing effects of adding more roughness elements in a given area (the increase in surface area encapsulated by the first term λ_f) and the increased sheltering effects encapsulated in the second term $\left[1-\sqrt{(\lambda_f)}\right]^2$. This term is a measure of the area unoccupied by the roughness elements. It is the square of the ratio of the non–roughness occupied length in the streamwise direction given by $(l_x - w)/l_x$. As λ_f is increased, the elements get closer to each other ($l_d/h = (l_x - w)/h = 1 - \sqrt{\lambda_f}$) and increase the sheltering. It can be seen that Eq. 5.24 has a maximum at $\lambda_f = 0.25$. Thus $z_o/(h-d)$ peaks at a value of 0.25 while for z_o this peak shifts to the left since $1 - d/h$ is monotonically decreasing function of λ_f.

The model by Macdonald et. al.[143] is another simplified analytical model in the literature which has been applied to predict the trends for z_o in the whole range of

λ_f for aligned and staggered cubes. There z_o and d are expressed in the form

$$\frac{z_o}{h-d} = \exp\left(-0.5\beta\frac{C_d}{\kappa^2}\left(1-\frac{d}{h}\right)\lambda_f\right)^{-1/2} \tag{5.25}$$

$$\frac{d}{h} = 1 - A^{-\lambda_p}\left(1-\lambda_p\right). \tag{5.26}$$

where A, β are parameters that can be fitted. This gives an expression of z_o in the form

$$\frac{z_o}{h-d} = \exp\left(-0.5\beta\frac{C_d}{\kappa^2}\left(A^{-\lambda_p}\left(1-\lambda_p\right)\right)\lambda_f\right)^{-1/2} \tag{5.27}$$

This form also gives similar trends for the range of λ_f. However it requires that A and β be determined from the experimental data. Comparing this expression with that of the simplified analytical model Eq. 5.6 and the form with $G = 1$ (Eq. 5.24) some similarities can be seen in the dependence of z_o on λ_f and C_d. However the difference in the current approach is in how the mutual interactions are modeled with the form of K_a giving a way to predict z_o and d without requiring calibrations for parameters.

5.2.2 Fully Staggered arrangement

For a fully staggered arrangement the spanwise sheltering becomes the predominant sheltering mechanism (Fig. 5.7a), but at high λ_f there is a possibility that the

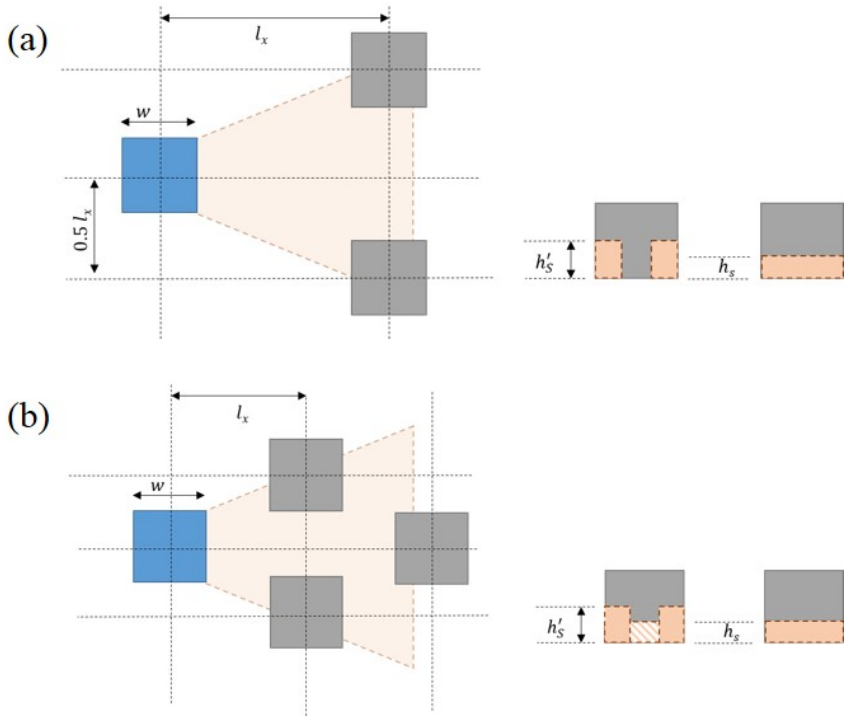

Figure 5.7: Illustration of the volumetric sheltering for a fully staggered arrangement (a) only spanwise sheltering (b) streamwise sheltering also present when the elements are close.

streamwise shading will be active as well (Fig. 5.7b). A form of K_a for the staggered arrangement is derived leading to (see Appendix C).

$$K_a = \frac{2a_o^2}{\left(C(1)\right)^2 C_d \left(1-\sqrt{\lambda_f}\right)^2}. \tag{5.28}$$

In Appendix C an estimate of the value of $C(1) = 1.5$ is obtained and shown to work well. Eq. 5.28 is used in conjunction with Eqs. 5.17 to predict z_o and d for the staggered arrangement and is compared with both experimental and simulations results from the literature as well as the analytical model[63] (Fig C.4). It is seen that the solution using Eq. 5.28 predicts the trends from the literature and also predicts

value very similar to that of the analytical model[63] for both z_o and d.

Now instead of using the full iterative solution the explicit relation given in Eq. 5.17 along with the three forms of G will be used. The results are shown in Fig. 5.8 which shows that the explicit formula does predict z_o and d well and also matches the iterative solution closely. As compared to the aligned case here the differences from the iterative solution are greater for the three cases, but as can be seen from Fig. 5.8b they decrease rapidly especially for the 2^{nd} order correction term with differences $< 10\%$ for most of the range of λ_f. Note that for these cases K_G can go below a_o but for these cases the value is clipped to a_o. Because of the clipping of K_G to not go below 0.4, the difference for the uncorrected case is actually lower than the 1^{st} order correction for values of $\lambda_f < 0.1$. Fig 5.9 shows the effect of removing this clipping behavior. Now for small values of λ_f, K_G can go below 0.4 but the overall trends still remain the same.

The explicit relation works well for staggered arrangements and Eq. 5.28 predicts a smaller value of K_a for a staggered case as compared to an aligned case which indicates reduced sheltering in the case of the staggered arrangement as is expected. Thus $C(\zeta)$ encapsulates the reduction in sheltering for the staggered arrangement as compared to an aligned arrangement at the same λ_f. Thus $C(\zeta)$ is in a sense similar to the β parameter used by Macdonald et. al.,[143] but here $C(\zeta)$ is estimated using phenomenological arguments and not left as a parameter. This reduced sheltering leads to a higher z_o and lower d for the staggered arrangement as compared to the

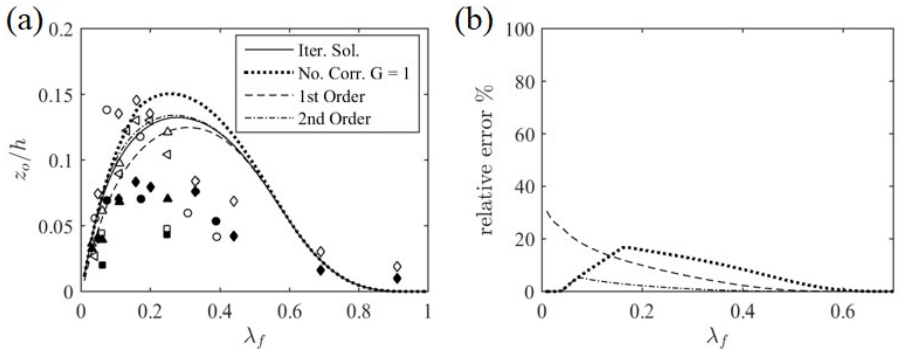

Figure 5.8: Comparison for the fully staggered case of (a) z_o from the full iterative solution against predictions from explicit corrections. (b) a measure of the relative error in using the correction as opposed to the full iterative solution.

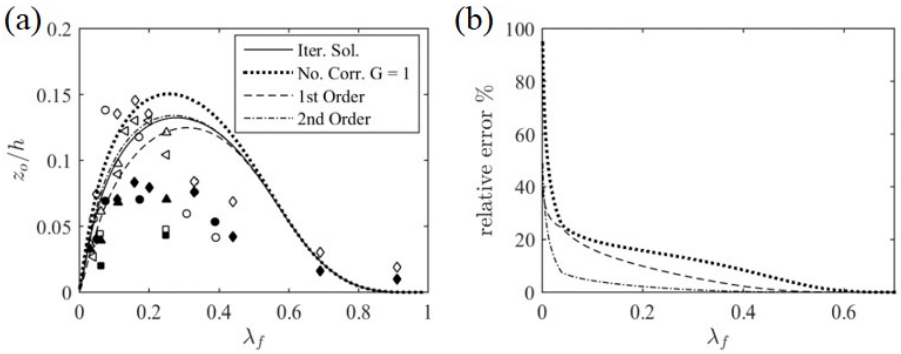

Figure 5.9: Comparison for the fully staggered case without clipping of K_G (a) z_o from the full iterative solution against predictions from explicit corrections. (b) a measure of the relative error in using the correction as opposed to the full iterative solution.

aligned arrangement for the same value of λ_f. It is also seen that for low values of λ_f K_G values become less than a_o, which should be clipped to a_o. Note that without clipping differences between the iterative solution and the explicit formula would be higher for the lower λ_f range (< 0.1) as shown in Fig. 5.9 although the trends are still the same.

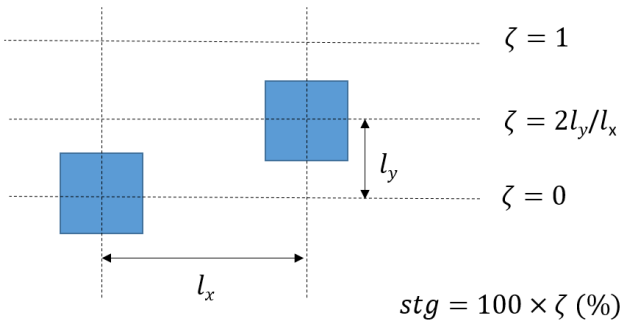

Figure 5.10: Illustration of a percentage stagger arrangement. $stg = 0, \zeta = 0$ is an aligned arrangement and $stg = 100, \zeta = 1$ is a fully staggered arrangement

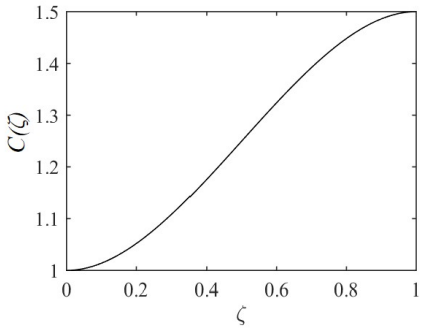

Figure 5.11: Variation of $C(\zeta)$ as a function of the percent stagger ζ.

5.2.3 Percent Stagger

A percent stagger arrangement with a stagger ratio $\zeta = 2l_y/l_x$ and a corresponding percent stagger $stg = 100\zeta$ is illustrated in Fig 5.10. The arrangement can vary from fully aligned ($\zeta = 0$) to fully staggered ($\zeta = 1$). Inspired by the fully staggered arrangement and following a similar argument K_a for this case can be written in the form

$$K_a = \frac{2a_o^2}{[C(\zeta)]^2 C_d \left(1 - \sqrt{\lambda_f}\right)^2}, \tag{5.29}$$

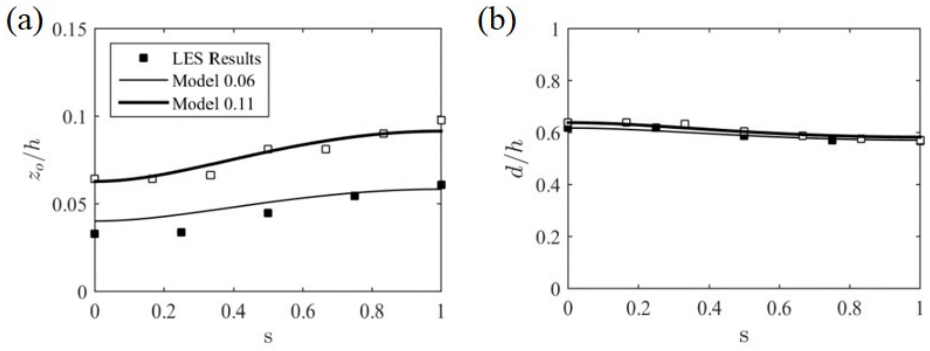

Figure 5.12: Comparison of (a) z_o and (b) d predictions from the full iterative solution against measured values from experiments and simulations for roughness elements of various percent stagger with $\lambda_f = 0.06$ and 0.11.

where $C(0) = 1$ corresponds to the aligned case and $C(1) = C^{st}$ corresponds to the fully staggered case. From symmetry and periodicity of the arrangements ($\zeta = 1 + r$ is the same arrangement as $\zeta = r$), $C(\zeta)$ should approach these limits smoothly. One way to ensure this is to propose that $C(\zeta)$ be of the form

$$C(\zeta) = c_o + c_1\zeta + c_2\zeta^2 + c_3\zeta^3 \tag{5.30}$$

and using the conditions above $C(\zeta)$ can be written as

$$C(\zeta) = 1 + 1.5\zeta^2 - \zeta^3 \tag{5.31}$$

This formulation of $C(\zeta)$ is used to solve for a iteratively, and the results are given in Fig. 5.12. It is seen that the predictions compare well against the LES[63] for both z_o and d. Each case has a fixed value of λ_f and the arrangement is varied

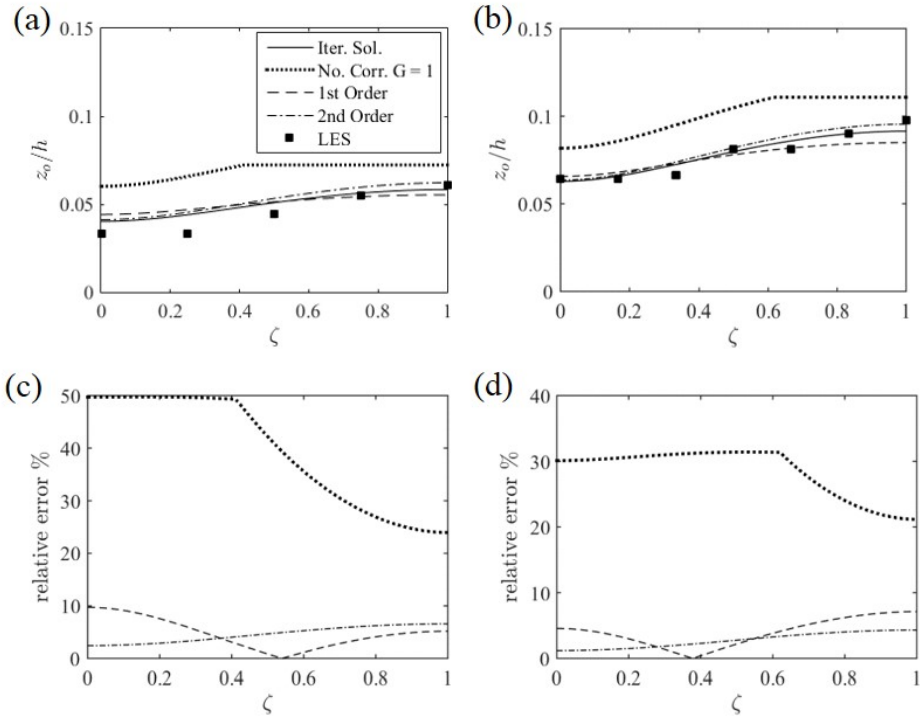

Figure 5.13: Comparison of z_o from the full iterative solution against predictions from explicit corrections for $\lambda_f =$ (a) 0.06 and (b) 0.11. measure of the relative error in using the correction as opposed to the full iterative solution for $\lambda_f =$ (c) 0.06 and (d) 0.11.

from a fully aligned to a fully staggered case. This is done for two different values of $\lambda_f = 0.06$ and 0.11. The LES data and the model prediction show a similar trend, where z_o increases with ζ while d decreases. This behavior is a manifestation of the decrease in sheltering that happens when the elements move from an aligned to a fully staggered case. Next, the explicit formula is tested for these arrangements, and the results are shown in Fig. 5.13a and b. It is seen that contrary to the earlier cases, the uncorrected results ($G = 1$) do have significant differences from the LES results even though they follow the same trend. This is because here a more subtle variation of z_o is investigated, since λ_f is fixed, and the arrangement is varied from an aligned

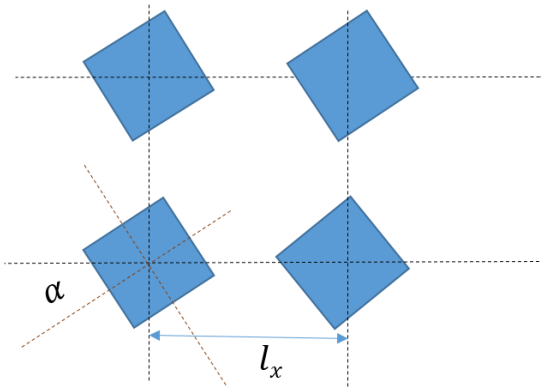

Figure 5.14: Illustration of the volumetric sheltering for an aligned arrangement of cubes with orientation α.

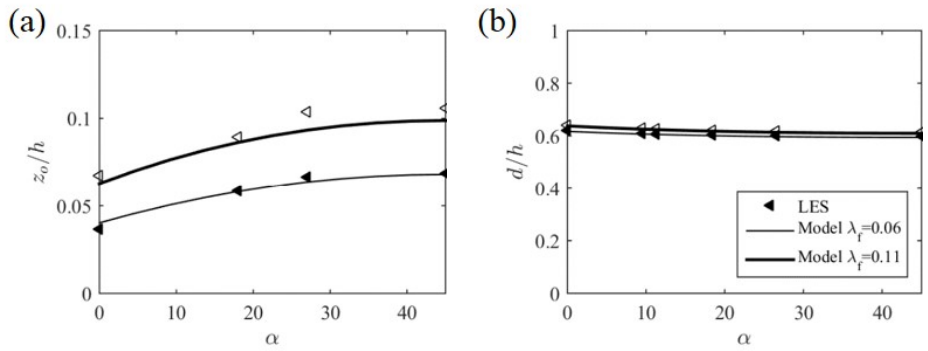

Figure 5.15: Comparison of (a) z_o and (b) d predictions from the full iterative solution against measured values from experiments and simulations for roughness elements of various orientation aligned arrangement with $\lambda_f = 0.06$ and 0.11.

to staggered case. The first and second order corrections give results close to the LES values. The difference from the full iterative solution can be seen in Fig. 5.13c and d where as expected the no correction case has a large difference while the other two cases have $< 10\%$ deviation from the full iterative solution.

5.2.4 Orientation

Next consider the case of aligned cubes which are arranged so as to have an orientation of α to the flow direction as shown in Fig. 5.14. As α is increased from 0 to $\pi/4$ the elements have increased frontal area facing the flow and the frontal area ratio is given by

$$\lambda_f = \lambda_f^0 \left[\cos(\alpha) + \sin(\alpha)\right] \tag{5.32}$$

where λ_f^0, is the frontal area ratio for the corresponding arrangement with $\alpha = 0$ and is also a measure of the streamwise distance between the elements. To derive K_a for such an arrangement similar arguments can be used as for the aligned case but with a frontal area λ_f^α. This leads to K_a of the form

$$\begin{aligned} K_a &= \frac{2a_o^2}{C_d\left(1-\sqrt{\lambda_f^0}\right)^2}\left(\frac{\lambda_f^0}{\lambda_f^\alpha}\right) \\ K_a &= K_a^0\left[\cos(\alpha)+\sin(\alpha)\right]^{-1} \end{aligned} \tag{5.33}$$

where K_α^0 is the value for $\alpha = 0$. This formulation of K_a is used in the iterative solution as for the earlier cases, and good predictions are obtained for z_o and d as compared to the simulations (Fig. 5.15). Both the LES[142] and the model predict that z_o increases as α is increased from 0 to $\pi/4$. From the model it is seen that this is both due to an increase in drag due to higher frontal area facing the flow and a reduction in sheltering for non–zero orientation. Instead of the iterative solution, the

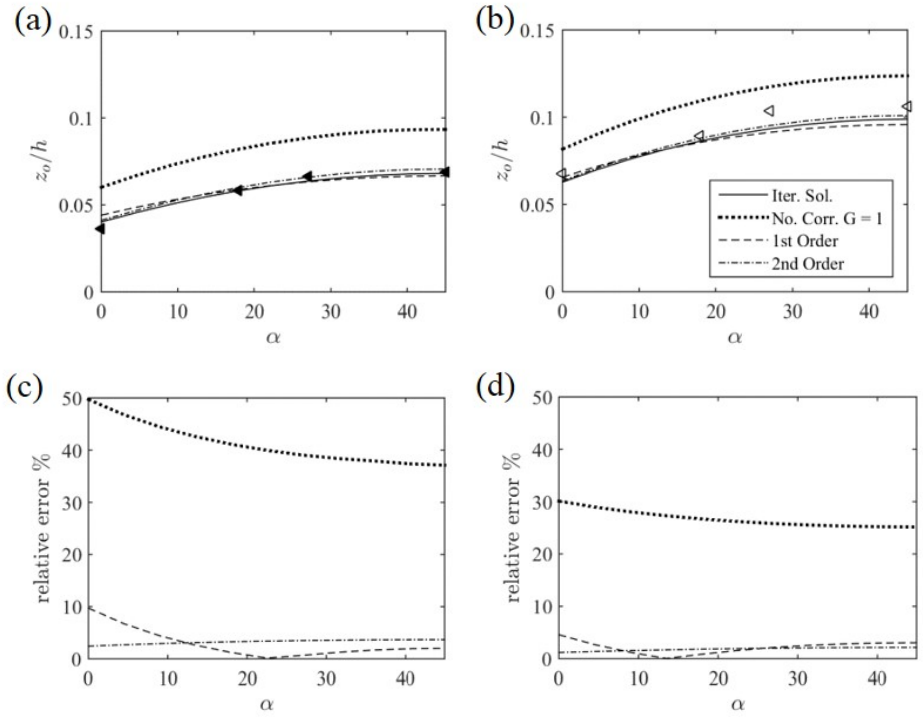

Figure 5.16: Comparison of z_o from the full iterative solution against predictions from explicit corrections for $\lambda_f^0 =$ (a) 0.06 and (b) 0.11. measure of the relative error in using the correction as opposed to the full iterative solution for $\lambda_f =$ (c) 0.06 and (d) 0.11.

explicit formula Eq. 5.17 can be used, and it can be seen that the explicit formula also predicts the same trend, and with either a first or second order correction provides a good match with the LES data (Fig. 5.16a,b). The difference from the iterative solution is very small for the corrected versions (Fig. 5.16c,d) while the uncorrected form has a vertical shift with a higher z_o but still predicts a similar trend.

5.3 Collapse of Data from Different Cases

In the previous section it is shown that z_o and d can be predicted using an explicit relation for rough surfaces created by various arrangements of cubic elements for various λ_f and for aligned, staggered, roughness-element orientations and different values of percent stagger. In all cases z_o and d are given by expressions of the form

$$\frac{d}{h} = \left[G' - \frac{1}{2K_G} \right] \tag{5.34}$$

$$\frac{z_o}{h-d} = \exp\left[-\kappa \left(\frac{C_d \, \Lambda_f}{2} \right)^{-1/2} \right] \tag{5.35}$$

$$\Lambda_f = \frac{\lambda_f}{K_G G'}, \quad K_G = K_a G, \quad G' = \frac{1}{1 - \exp(-2K_G)} \tag{5.36}$$

with the value of K_a calculated as shown in the preceding sections for the various cases, and the G is a specified form of the correction factor. Of the three forms tested here (Eq. 5.14), the second order form of G provides overall closer predictions to the LES results from Refs. 63 and 142. The prediction from Eqs. 5.34 – 5.36 matches the results from the LES in both the trends and also in predicting the actual values for the configurations considered. Usually rough surfaces are characterized using the frontal area ratio λ_f only, but for the same λ_f, depending on the arrangement of the roughness elements, the mean flow response will differ. This is illustrated in Fig. 5.17. where the LES data[63,142] are plotted as a function of λ_f for the different arrangements of cubic roughness elements. For both z_o and d (Fig. 5.17a,b) the general trend of z_o

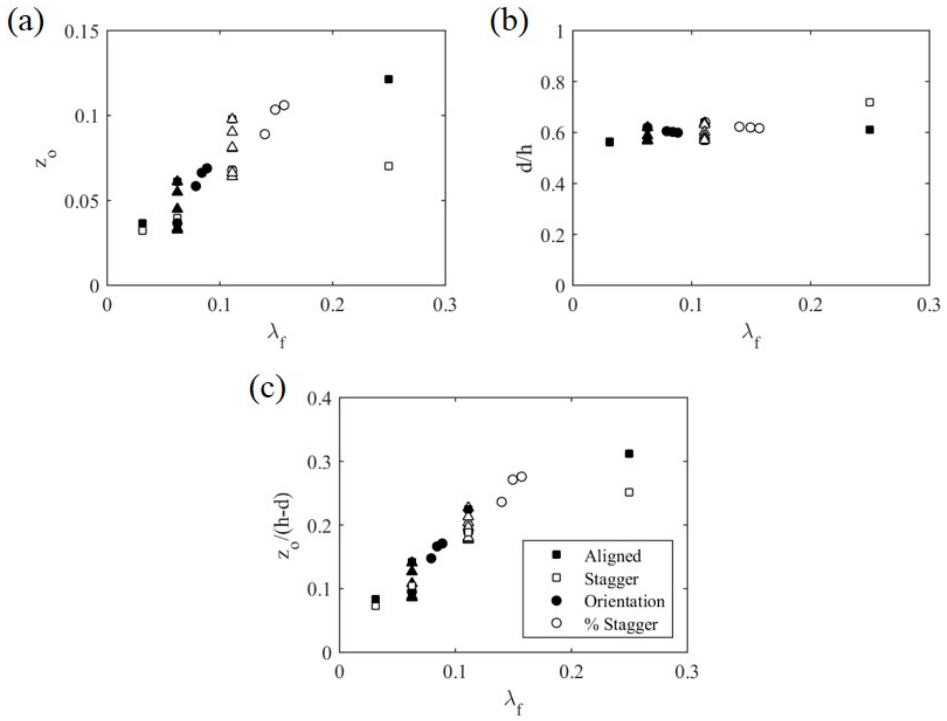

Figure 5.17: Comparison of (a) z_o/h, (b) d/h (c) $z_o/(h-d)$ for different arrangements from LES data[63]

and d increasing for $\lambda_f < 0.2$ is evident from these simulations while also illustrating that λ_f does not fully characterize the surface is known. Fig 5.17c shows that the difference in z_o is reduced if plotted in terms of $z_o/(h-d)$ but still noticeable variations are observed. Consider for example the case of $\lambda_f = 0.25$ for aligned and staggered case, where z_o for the staggered case is higher than the aligned case. Now if the data are replotted with the parameter not as a function of λ_f but using the variables Λ_f and K_G it can be seen that the various cases collapse on a single line both for z_o (Fig 5.18a) and d (Fig 5.18b). The line is the prediction from Eq. 5.35. Thus it can be seen that the explicit relation connecting z_o and d to the surface geometric properties performs well in capturing the trends for the various cases. In the equation

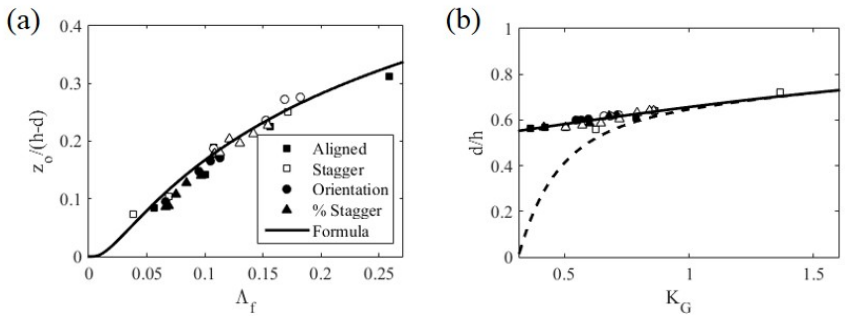

Figure 5.18: The LES data plotted as function of the geometric parameters and compared against the derived formula for (a) $z_o/(h-d)$ and (b) d/h.

for d if the G' correction is neglected (dashed line in Fig 5.18b) it is seen that the predicted d becomes incorrect for values of $K_a < 1$, which is a region in which most of the LES results are. Thus the correction term is important. To conclude it is seen that z_o for the surface is predicted by the rough surface parameter Λ_f which encodes information about the packing density of the roughness elements through λ_f and the sheltering between the elements via K_G and G'. Meanwhile the zero–plane displacement d depends on K_G and G'.

5.4 Predictions of Friction Velocity u_τ and Canopy Height Velocity U_h

The model in Ref. 63 also provides a way to predict u_τ and U_h from z_o and d for a specified boundary layer height

$$\begin{aligned} \frac{u_\tau}{U_o} &= \left[\frac{1}{\kappa}\ \ln\left(\frac{\delta - d}{z_o}\right) + \frac{2\Pi}{\kappa}\right]^{-1} \\ \frac{U_h}{u_\tau} &= \sqrt{\frac{1}{C_d \lambda_f}}\left[\frac{2a}{1 - \exp(-2a)}\right]. \end{aligned} \tag{5.37}$$

The results for substituting the z_o and d predicted from Eqs. 5.34 and 5.35 for the aligned and staggered arrangement are shown in Fig. 5.19. It can be seen that z_o and d predicted from the explicit equation does lead to a fair prediction for both u_τ and U_h for both the aligned and staggered cases as compared to the LES results. To obtain these results, the same value for δ/h was used as was used in Ref. 63. The values are $\delta/h = 5.2$ and $\Pi = 0.2$.

The equation for u_τ can be connected to the geometric parameters by substituting for d and z_o from Eqs. 5.34 and 5.35

$$\left[\frac{u_\tau}{U_o}\right]^{-1} = \left(\frac{C_d \Lambda_f}{2}\right)^{-1/2} + \frac{1}{\kappa}\ln\left(\frac{\delta/h - d/h}{1 - d/h}\right) + \frac{2\Pi}{\kappa}, \tag{5.38}$$

and for $\delta >> h$ the friction velocity can be written as

$$\left[\frac{u_\tau}{U_o}\right]^{-1} = \left(\frac{C_d \Lambda_f}{2}\right)^{-1/2} + \frac{1}{\kappa}\ln\left(\frac{\delta}{h - d}\right) + \frac{2\Pi}{\kappa}. \tag{5.39}$$

There are three terms contributing to the expression for u_τ. The first term is a "drag" term which is C_d times an area ratio ($\Lambda_f \sim \lambda_f / K_a$). This is modified by a term which introduces the dependence on the boundary layer height scaled by $h - d$ plus the

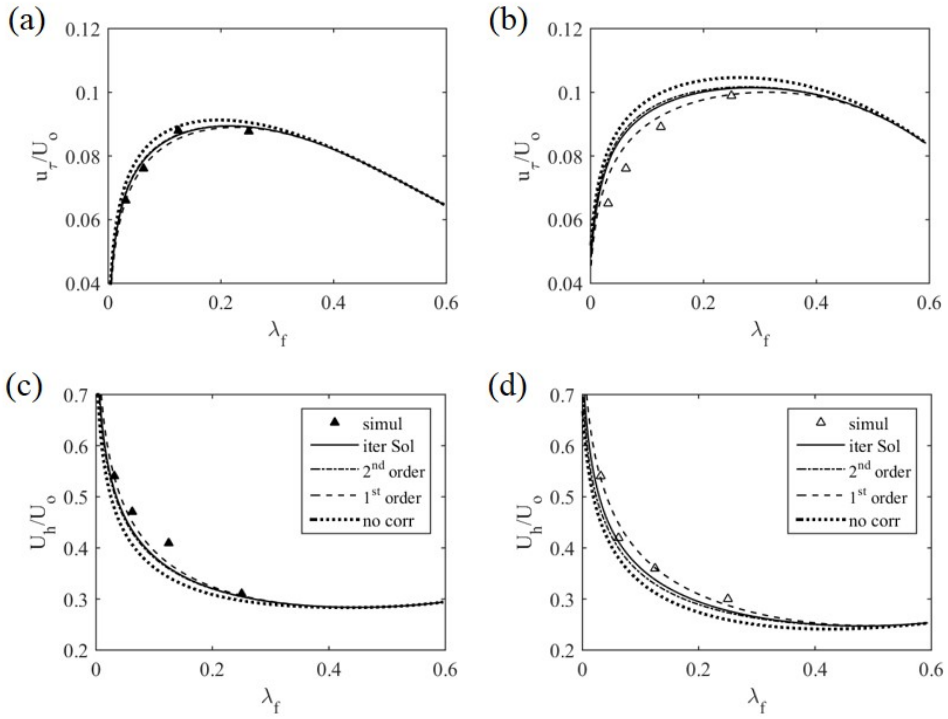

Figure 5.19: The model predictions for the friction velocity compared against the LES data for (a) aligned and (b) staggered arrangement of cubes while (c) and (d) are the corresponding canopy height velocity for the two arrangements.

wake correction parameter Π to account for the outer–layer dynamics. The effect of the terms and their variation with λ_f is shown in Fig. 5.20 for aligned and staggered arrangements. Here Π is set to 0 and $\delta/h = 5.2$ is used. The first term captures the trend of the behavior of u_τ which is modulated by the variation in the second term. Equation 5.39 can also be expressed as

$$\left[\frac{u_\tau}{U_o}\right]^{-1} = \left(\frac{C_d \Lambda_f}{2}\right)^{-1/2} - \frac{1}{\kappa}\ln\left(1 - G' + \frac{1}{2K_G}\right) + \frac{1}{\kappa}\ln\left(\frac{\delta}{h}\right) + \frac{2\Pi}{\kappa}. \tag{5.40}$$

The first two terms are dependent only on the rough surface morphology while the

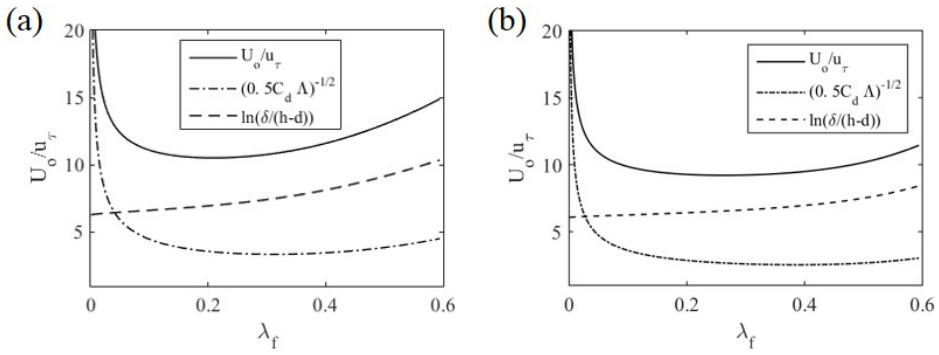

Figure 5.20: Comparison of the effect of the different terms on the friction velocity for (a) aligned and (b) staggered arrangements.

third term is the effect of the boundary layer height.

5.5 Summary

In this study, an explicit analytical model has been developed which allows calculation of the mean flow response on a cube-roughened surface from the surface morphology. The predictions from the explicit model are seen to match well with simulation and experimental results in the literature. The explicit model is valid for a variety of different arrangements – aligned, staggered, percentage stagger, roughness element orientation and for the whole range of frontal area ratios from the very sparse to the very dense. The geometrical parameters explicitly take into account not just λ_f but also the variations in the arrangements for the different cases. The model also identifies new effective geometrical parameters, Λ_f and K_G which control the mean flow response. Using these parameters, it is seen that the data for the different cases collapse onto a single curve which is the prediction from the explicit relation.

The advantage of this approach is that the calculation of z_o, d and u_τ requires only knowledge of Λ_f and K_G for a given surface which are easy to calculate. Along with z_o and d the current approach also provides an explicit equations for the canopy height velocity U_h and the friction velocity u_τ. It is seen that the friction velocity for a surface is determined from three terms – a drag term which is modified by the effect of d and the boundary layer height δ. The predicted friction velocity also matches fairly well with the simulation results from Ref. 63. Thus this approach seems a good way to obtain relations connecting rough surface geometry to the mean flow response although the approach has been tested so far only for cubes for the cases discussed above. More research is required to extend such an analysis to surfaces with variation of heights and also for more complex roughness elements.

Chapter 6

Thesis Summary

Turbulent flow over rough–walls is a topic that is of practical interest in a variety of areas and which has rich and complex physics associated with it. This thesis has been an attempt to delve into an important aspect of such flows – that of the mean flow response to macro–scale roughness elements and connecting it to the rough surface topology. The aim was to quantify the response as a function of the rough surface topology. The study was undertaken using high–fidelity simulations, wherein the roughness element geometry was resolved using the sharp–interface immersed boundary method, and an integral wall model was used to apply the stress condition. Even with very idealized geometries such simulations are very computationally intensive, and there is a very large parameter space that has to be traversed. Analytical and explicit analytical reduced flow models are also developed to complement these

large–scale simulations. Such models can estimate the flow properties quickly and accurately. This thesis investigated the problem of rough–wall boundary layer flows mainly through two applications – effect of barnacle fouling on ship hulls and neutral atmospheric boundary layer flow over urban canopies.

Biofouling on ship hulls leads to increased losses and has a significant economic impact. To analyze this problem in–depth, first detailed flow around attached individual acorn barnacles, which are a major agent of biofouling was studied. The flow was also compared against idealized geometries generated from analysis of 3D scans of the barnacles. The flow features were seen to have aspects similar to those of more canonical cases present in the literature. The major features of the flow were also captured fairly well by the idealized frustum geometry even though the detailed shape of the barnacles do affect the flow. Arrays of these geometries at different packing densities and arrangements were used to create idealized representations of barnacle fouled surfaces. Large eddy simulations were carried out to parameterize the mean flow properties with respect to the packing density and arrangement. It was seen that at low coverage density, the arrangement does not have much of an effect and both the aligned and staggered arrangement had similar values for the rough wall boundary layer parameters and the drag, similar to the results in literature for flow over cuboidal arrangements.

Next a parametric study was done on turbulent flow over rectangular–prism roughness elements. These are usually used in the literature to stand for neutral ABL flow

over urban canopies. In this thesis, the effect of roughness element aspect–ratio, coverage density and arrangement were investigated in detail by picking representative points from the parameter space and carrying out LES for these cases. Coupled with these large–scale simulations, a new analytical rough wall model was also extended to high aspect–ratio elements and tested by comparing the predictions of the model against the LES data. It was seen that the model predicts that for aligned arrangements, the drag and the roughness length–scale both plateau after a certain aspect–ratio, results that were confirmed from the LES data. This is an effect of the increased sheltering between the elements, and it means that beyond a coverage density dependent cut–off aspect ratio, the flow does not see the effect of the aspect–ratio. It was seen that this effect is not observed for the staggered set of cases that were run, both from the LES and from the model – indicating a reduction in the sheltering effects for staggered arrangements. This study serves to quantify the effect of aspect–ratio of cuboidal roughness elements on the mean flow response. The model that is developed is also very useful to quickly estimate the effect of various idealized urban canopy arrangements.

The analytical model, while a quick and easy tool for estimating the drag and aerodynamic properties of rough surfaces, is constrained by the fact that it is difficult to apply for non–canonical roughness geometries and arrangements. As an attempt to address this issue, a more generalized extension of this method is attempted and the initial results are shown in Appendix A.

Finally, the possibility of deriving an explicit analytical model, similar to the engineering correlations for rough surfaces, is investigated. This is done by leveraging the analytical roughness model and so is currently constrained to cuboidal geometries. It is seen that for the canonical arrangements investigated, such a relation is indeed possible, and it connects the flow response directly to the geometrical parameters. Expressing the flow response in terms of these geometrical parameters allows collapse the data from disparate arrangements onto a single curve which is predicted from the explicit relation.

The types of rough surfaces that are present in engineering and geophysical applications are very vast. In this thesis attention has been mostly focused on fairly canonical types of surfaces. This was due mainly to computational cost constraints. Still, even for these simpler geometries there was an avenue to perform detailed quantification of the geometric effects. The computational tools applied in these studies are more generally applicable, and as a future study it would be interesting to apply the rescale–recycle–inflow integral–wall–modeled sharp–interface–immersed–boundary LES simulation technique to flow over more complex surfaces, including multiple scales and random roughness. Effects of flow stratification and buoyancy might be another avenue that could be explored. The integral wall model is applicable more widely and not just to rough wall boundary layers – another very important application could be to study flow separation and flow control over airfoils, turbine blades etc. Such efforts are currently under–way, and the results are promising.[144]

The simulations carried out have aided in the extension and validation of flow based phenomenological predictive models for the aerodynamic properties of rough surfaces. These are very promising as the models takes on the order of $1 - 100$ seconds to run instead of the $O(10^5)$ CPU hours required for the CFD computations.

Appendix A

A Generalized Shading Model for Macro–Scale Roughness Elements

As discussed in the Chapter 4 the analytical model is restricted to simple arrangements of rectangular–prism roughness elements. However, many rough surfaces of practical interest are more complex, and the analytical approach would be difficult to apply for such surfaces. This appendix attempts to extend the analytical roughness model to develop a general approach that can handle more complex rough surfaces. An example of such a surface is shown in Fig A.1a, and a zoomed in view of a region of the surface is shown in Fig A.1b. As a first step, the formulas for geometric and aerodynamic parameters for a general rough surface are presented in Sec. A.1. An important step is to extend the shading model to more general cases which is done

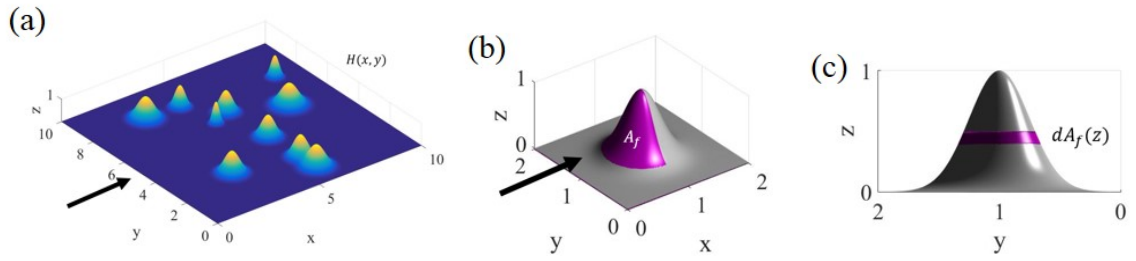

Figure A.1: (a) an example of a surface with a random arrangement of roughness elements. (b) illustration of the frontal area A_f and (c) the sectional area $dA_f(z)$.

in Sec. A.2. This general model developed requires a numerical solution procedure and is first tested and validated for the cases of aligned and staggered cubes and rectangular–prism elements. These comparisons are shown in Appendix B and are cases where the general model should give the same result as the analytical model (up to numerical accuracy). The model is then applied to various experimental and numerical studies from literature in Sec. A.3 and in Sec. A.4. The barnacle fouled surfaces from Chapter 3 are now revisited, and the model predictions are compared against the LES results in Sec. A.5.

A.1 Calculation of Geometric and Aerodynamic Parameters

A general rough surface such as in Fig. A.1 can be represented in the form of $H(x, y)$ where the surface has a height $H(x, y)$ at a horizontal position (x, y). The geometric parameters of interest of such a surface (λ_f, λ_p) are not known apriori and must be

calculated. Without loss of generality, the x coordinate is assumed to be aligned with the flow direction and y is the spanwise direction. The frontal area A_f (Fig A.1b) can then be expressed in terms of $H(x, y)$ as

$$A_f = \int_0^{L_y} \int_0^{L_x} \frac{1}{2} \left| \frac{\partial H}{\partial x} \right| dxdy \tag{A.1}$$

where the horizontal extend of the surface is from 0 to L_x in the streamwise and 0 to L_y in the spanwise directions. To find the sectional frontal area $dA_f(z)$ (Fig. A.1c) the expression is

$$A_f(z) = \int_0^{L_y} \int_0^{L_x} \frac{1}{2} \left| \frac{\partial H^z}{\partial x} \right| dxdy \tag{A.2}$$

$$H^z(x, y) = \max[H(x, y), z] \tag{A.3}$$

$$dA_f(z) = \frac{d}{dz} \left(\int_0^{L_y} \int_0^{L_x} \frac{1}{2} \left| \frac{\partial H^z}{\partial x} \right| dxdy \right) dz \tag{A.4}$$

where $A_f(z)$ is the frontal area up to a height z.

As was seen in Sec. 2.2 in the most general form, z_o and d are related to the attenuation coefficient in the form

$$\frac{u_\tau}{U_h} = \sqrt{\frac{C_d}{A_T} \int_0^h \exp[a(z/h) - 1] dA_f(z)} \tag{A.5}$$

$$\frac{z_o}{h - d} = \exp\left[-\frac{\kappa}{u_\tau / U_h} \right] \tag{A.6}$$

$$\frac{d}{h} = \frac{\int_0^h \exp[a(z/h) - 1] z dA_f(z)}{\int_0^h \exp[a(z/h) - 1] h dA_f(z)}. \tag{A.7}$$

For a general surface $H(x, y)$, the expression for the sectional frontal area $dA_f(z)$ can be used to solve for z_o, d and further for u_τ and U_h if the value of the attenuation coefficient of the surface 'a' is known. For cuboidal elements, the attenuation coefficient is calculated using the idea of "volumetric shading" as has been explained previously (Sec. 2.2 and Sec. 4.3) to capture the interaction between the elements. In that approach, the low–momentum region behind a roughness element is parameterized using a simple shape which is postulated to depend on the ratio of the turbulent velocity scale to the convective velocity scale. In the next section a methodology will be presented in brief for obtaining the volumetric shading for a general surface.

A.2 Generalized Shading Model

The shading volume has been illustrated for the example of a cubic roughness element in Fig. 2.6a. This volume can shade part of the frontal area of the roughness element producing a shaded area (Fig 2.6b,c). In the analytical model the shaded area is converted into an "equivalent shaded height" which is a one–dimensional representation of the shaded–area (Fig 2.6d).

This method can now be extended for a general surface S which is defined as a set of points which has a height $H(x, y)$ at a horizontal location (x, y). First the surface

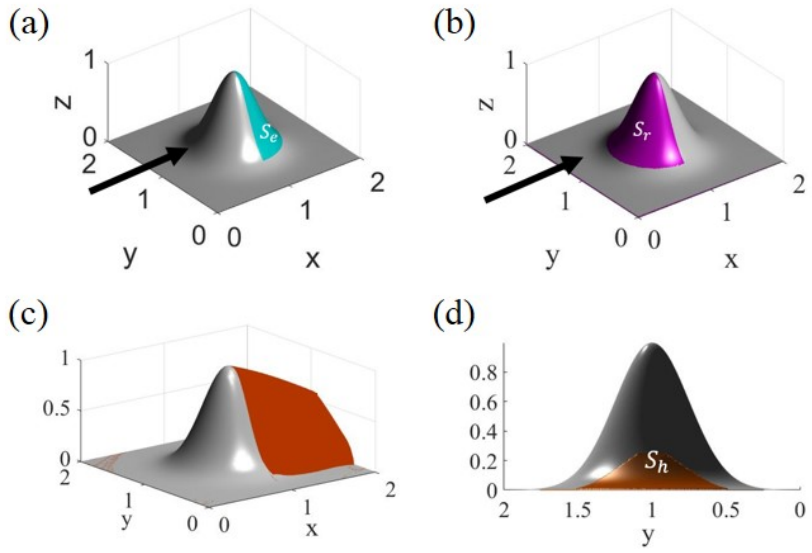

Figure A.2: Dividing the surface into (a) emitter (S_e) and (b) receptor (S_r) Surfaces. (c) is the volumetric shading generated by S_e while (d) is the illustration of a shaded area.

is split into three parts – emitter (S_e), receptor (S_r) and inert (S_n) surfaces. The emitter surface is that part of the surface that is in the leeward portion and is defined as the set of points on the surface having surface normals with a positive component in the direction of the flow. Similarly, the receptor surface is the part of the surface which is facing the flow i.e. where the normals have a negative component in the flow direction. The inert surfaces have normals perpendicular to the flow direction. The gradient of H gives the normal of the surface and can be used to identify to whether a particular point on the surface (x, y, H) is part of S_e, S_r or S_n.

S_e consists of the set of points that generates the shading volume (V_{sh}) which is illustrated in Fig. A.2c. S_r is the set of points that faces the flow and is responsible for generating the form drag. Depending on the geometry and arrangement of the

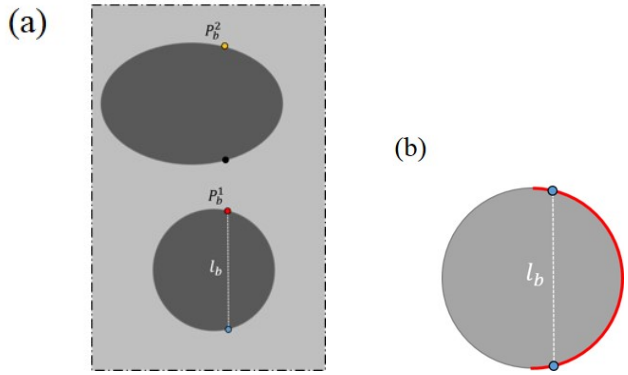

Figure A.3: (a) The creation of an elemental edge corresponding to a point P_e. (b) The edge length l_b associated with the point P_b.

rough surface, a part of the receptor surface could fall within the shading volume. This surface which is the intersection of V_{sh} and S_r gives the sheltered surface S_h (an illustration is shown in Fig. A.2d). The sheltered surface is considered to be inactive and does not generate any drag since it is "shaded" from the flow and the flow does not "see" this surface.

The current method aims to calculate the height of the shading volume at all horizontal locations (x, y). To do so the S_e has to be first converted into a set of elemental sections (edges). This is illustrated in Fig. A.3a,b. The top view of the surface shows a part of a rough surface that has a cylindrical roughness element and an elliptical element. The blue dot is a point P_e which belongs to S_e. The edge corresponding to P_e is created by connecting P_b^1 to P_e and has an edge length l_b. This procedure is followed for all points that are part of S_e. For each of these edges, the local–aspect ratio is defined using the edge–length and the height of the surface at that point. This creates an element e_b with an edge length l_b which can be used

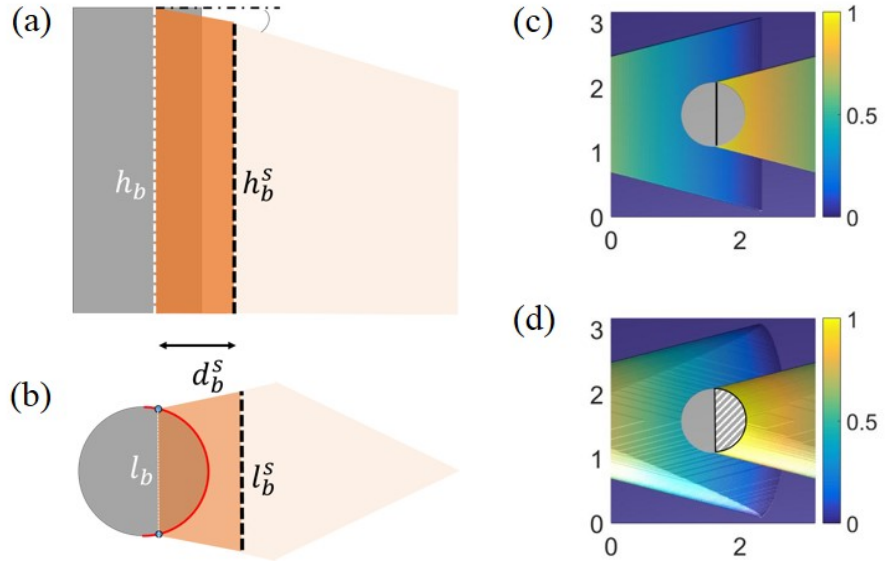

Figure A.4: (a) Side and (b) Top view of the projection and sweep method to generate the height of the shading volume corresponding to an edge l_b. (c) The top view showing the height of the shading volume for one edge S_{sh}^b. (d) The height of the shading volume for the full surface. The edges used to generate this area are given by the white hatched region. For (c) and (d) the color indicates the height of the shading volume.

to calculate the local aspect–ratio $\rho_b = l_b/H(x, y)$ For example, for a cube this would give the edge length of the cube w, and the points would be the two extremities of the backward facing edge at height h of the cube. But this is a general specification and can work for surfaces which do not have well defined canonical arrangement of geometries.

Now it is assumed that each elemental section has an associated shading volume, which is similar to that of a rectangular–prism element of the same aspect ratio. The total shading volume generated by the surface is then the integrated effect of the shading volume generated by each of these elements. The shading volume for an element e_b, V_{sh}^b is represented by a volume which has a height h_b^s and a spanwise

extend l_b^s at a location d_s downstream from the edge. This is generated by sweeping and projecting the edge e_b downstream (Fig. A.4a,b) using

$$h_b^s(d_s) = \max\left[\left(H(x,y) - d_s \tan\theta\right), 0\right] \tag{A.8}$$

$$l_b^s(d_s) = \begin{cases} l_b + 2d_s \tan\theta & 0 < d_s \leq l_b/\tan\theta \\ 3l_b - 2d_s \tan\theta & l_b/\tan\theta < d_s \ \leq 2.5l_b/\tan\theta \end{cases} \tag{A.9}$$

Thus by sweeping and projecting the edge in a piece–wise fashion, the height of the sheltering volume is generated for a particular edge. This is illustrated in Fig. A.4c for a surface made of repeating tiles of a cylindrical roughness element attached to a flat plate. The height of the shading volume generated from each edge is given by $H_{sh}^b(x,y)$ at a horizontal location (x,y). It can be seen that within the spanwise extend l_b^s H_{sh}^b will be equal to h_b^s and will be zero outside this region. The integrated effect of all the elemental edges gives the total height of the shading volume for the surface at every (x,y) (Fig. A.4d) and is given by

$$H_{sh}(x,y) = \max(H_{sh}^b(x,y)). \tag{A.10}$$

H_{sh} can be used to identify the shaded area which is the minimum of H_{sh} and H at the horizontal locations (x,y) which are part of S_r (Fig. A.5.)

In the analytical model this shaded area is converted into an equivalent shaded height h_s by finding the height $z = h_s$ at which the frontal area up to z, $A_f(z)$, is

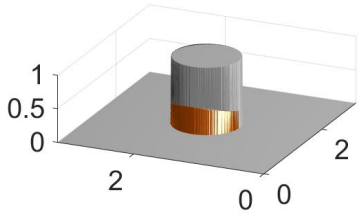

Figure A.5: Illustration of the shaded height for a cylindrical roughness element.

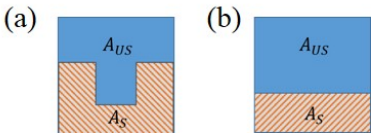

Figure A.6: Sketch of (a) an example shaded area predicted by the model $H_s h(x, y)$ for staggered cubes and (b) the "equivalent" spanwise constant height shaded area of height h_s.

equivalent to the shaded area (Sec. 2.2 and Fig. 2.6d). This is also illustrated in Fig. A.6 using a shaded area similar to that seen for staggered cubes, where A_s is the shaded area and A_{US} is the unshaded area. For cubes of width w, the equivalent shaded height is $h_s = A_s/w$ where A_s is the area of the shaded region. For a general surface, the shaded area A_s can be calculated in a similar manner to Eq. A.1 using the x direction derivative of H_s

The h_s once calculated is used to perform a drag balance in the unshaded area (the blue area in Fig. A.6b) so as to get

$$C_{DH} U_h^2 \int_{h_s}^{h} dA_f(z) dz = C_d \int_{h_s}^{h} [u(z)]^2 \, dA_f(z) \tag{A.11}$$

which for a constant $dA_f(z)$ roughness element was shown to reduce to

$$a = \frac{a_o}{1 - h_s/h} \tag{A.12}$$

with the value of a_o depending on the ratio of C_{DH} to C_d. It was shown that for cubes this was equal to 0.4. This method will not work for general surfaces where it is not required that $dA_f(z)$ is a constant. It will also not be viable to define an "equivalent sheltered height" for a general surface. Instead if the full integral is performed (the corresponding region in the sketch is Fig. A.6b), it can be shown to be

$$C_{DH} \iint \left(|\nabla_x H| - |\nabla_x H_s|\right) dxdy = C_d \frac{h}{2} \exp(-2a) \iint \left(|\nabla_x E_H| - |\nabla_x E_{H_s}|\right) dxdy \tag{A.13}$$

$$E_\Psi = \exp(2a\Psi/h) \qquad \Psi = H, H_s \tag{A.14}$$

This condition Eq. A.14 can be written in the form

$$a + \log\left[\frac{C_{DH}}{C_d} \frac{\iint \left(|\nabla_x H| - |\nabla_x H_s|\right) dxdy}{h \iint \left(|\nabla_x E_H| - |\nabla_x E_{H_s}|\right) dxdy}\right] = 0 \tag{A.15}$$

Thus a more general condition for 'a' is obtained, which can be shown is equivalent to the construct in Eq. A.12 for a span–wise constant shading height (for example that produced by aligned cubes). This condition has to be solved iteratively, as was done in the analytical model, since the shaded area depends on $\tan\theta$ which in

turn depends on a. There are now two specifications for computing a – Eq. A.12 which converts the shaded area into an "equivalent height", and Eq. A.15 where the full integration is performed. Note also that Eq. A.12 is only valid for the case of roughness elements with a constant $dA_f(z)$, and for a general surface if the equivalent shaded height principle is to be used for these cases Eq. A.11 should be used instead of Eq. A.12.

For a general surface this procedure has to be carried out numerically, and the algorithm is coded up in MATLAB and requires the input in the form of a surface $H(x, y)$ of size $N_x \times N_y$. The input surface is assumed to be periodic, so only the minimum repeating tile need be specified. The code gives as output the geometric (λ_f, λ_p) and aerodynamic parameters (z_o, d, u_τ, U_h) of the surface. The input flow parameters that are to be specified are the drag coefficients C_d and C_{DH} (or a_o depending on the formulation used to solve for a) along with the boundary layer height δ and the wake correction factor Π to calculate u_τ and U_h. This method when applied to cuboidal surfaces and if the "equivalent shading height approach" and Eq. A.12 are used, should be exactly the same as the analytical formulation. The model is tested for aligned and staggered cubes and rectangular–prism elements using this formulation and the results are shown in Appendix B. It is seen that this general model does match the analytical model and also the results from the LES presented in Chapter 4. In Appendix B the effect of mesh size on the accuracy and solution time is also investigated. It is seen that the results do not vary much with the mesh size,

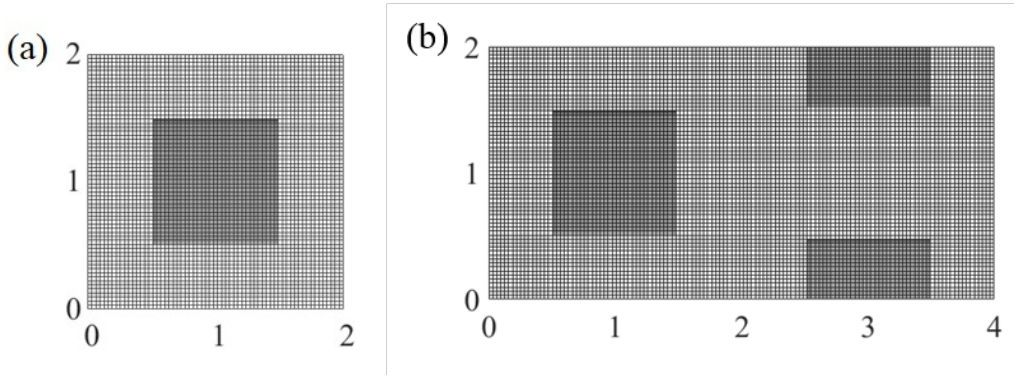

Figure A.7: Example input surfaces $H(x, y)$ for the aligned and staggered case.

and even a fairly coarse mesh would still give fairly accurate results. The next part to test is the new formulation for the attenuation coefficient by comparing the prediction from using the "equivalent height" approach in Eq. A.12 and the 2D integration of the unshaded area (Eq. A.15) to the experimental and simulation data present in the literature. This is done in the next section.

A.3 Comparison of the Equivalent h_s Method to the Full Integration Approach

A.3.1 Aligned and Staggered Cubes

Figure A.7 shows an example of the repeating tile used as input to the model. For these comparisons, a grid resolution of $N_x = N_y = 1024$ is used for the aligned case and $N_x = 2048$ is used for the staggered since the repeating tile has double the size of the aligned case in the streamwise direction. Such a high resolution is used since

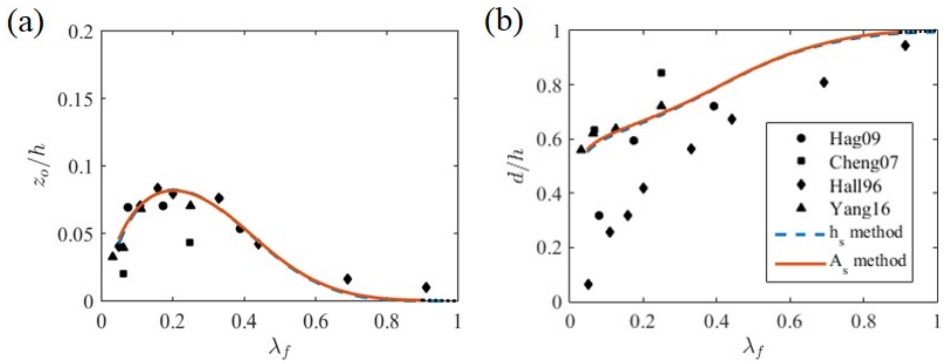

Figure A.8: Comparison of (a) z_o and d for aligned arrangements, obtained from the numerical model via the two methods and also compared against measurements from literature.

the variation in z_o and d should be captured smoothly with a $\Delta\lambda_f = 0.01$. For the aligned cubes the sheltered area is of constant height in the spanwise direction, since only streamwise shading is active as shown in Fig. 2.6b, which means Eq. A.15 will be equivalent to Eq. A.12, and the two methods should give the same result. This is indeed seen to be the case (Fig. A.8) with both curves lying on top of each other, and thus the two methods are shown to be equivalent for the aligned case.

For the staggered case the sheltered area is somewhat complicated (Fig. 2.6c,d), and the two methods could give different results. From the Fig. A.9 it is seen that at low values of λ_f the two methods match. Differences between the two start becoming apparent at values of λ_f greater than 0.2, and these differences seem to persist till $\lambda_f = 1$ with the full integral method approaching the limits more steeply. Since the computation for $\lambda_f = 1$ cannot be carried out, the predictions are extrapolated (the black line in Fig. A.9), and it does approach the correct limits of $z_o = 0$ and $d = 1$. The second point to note is that both of the methods give predictions which are

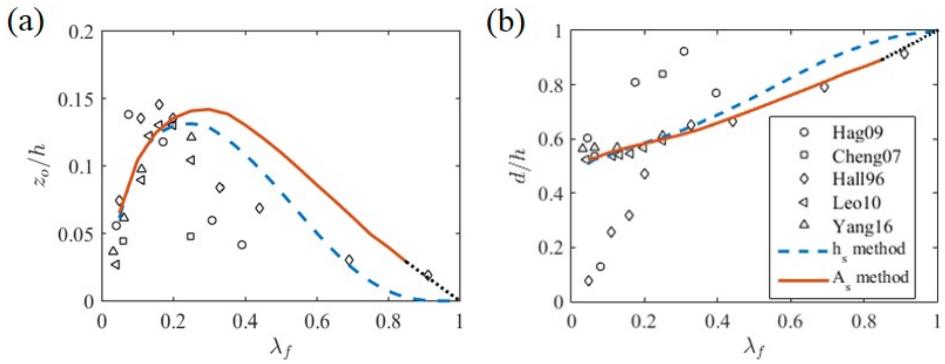

Figure A.9: Comparison of (a) z_o and d for staggered arrangements, obtained from the numerical model via the two methods and also compared against measurements from literature.

within the range of the values given in the literature. Thus both methods perform well, but the Eq. $A.15$ is more versatile.

A.3.2 Arrangements with a Percent Stagger

The next set of cases is to test the effect of varying the arrangement of the elements at a given density. Thus λ_f is fixed, and the percent stagger is varied from aligned ($stg = 0$) to fully staggered ($stg = 100$) (See Sec. 4.1 for the definition of stg). The results are plotted using the stagger ratio which is $\zeta = stg/100$. They are compared against results from an LES[142] for $\lambda_f = 0.06$ and 0.11 (Fig. A.10). Both methods match the LES results well and are fairly similar. It should be noted that for the $\lambda_f = 0.11$ case the 2D integration method gives a result that approaches the fully staggered limit more smoothly than the h_s case. The smooth behavior is consistent with the symmetry of the arrangement.

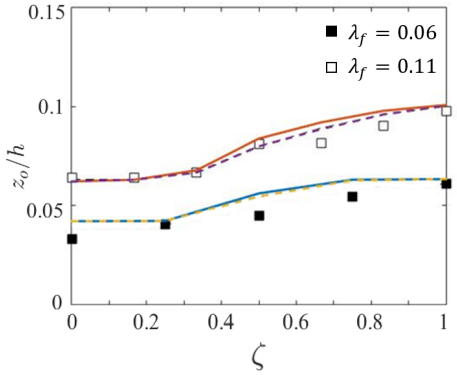

Figure A.10: Model comparisons against LES (a) for percent stagger and (b) for roughness element orientation. The points are LES from Ref 142, the solid lines are the A_s method while the dashed lines are the h_s method.

A.3.3 Roughness Element Orientation

The last case tested for cuboidal geometry is the case of roughness element orientation to the flow. Figure A.11a illustrates an example surface that is used in the computation along with the associated height of the shading volume. The roughness element is rotated so as to have an angle of α with respect to incoming flow. The surface shown here has an angle of 45^0 with the flow and a $\lambda_f = 0.16$ and a corresponding $\lambda_f^o = 0.11$, that is an arrangement at the same spacing, but zero orientation would have a solidity of 0.11. Note here that as α is increased from 0 to $\pi/4$, the frontal area of the elements increase, hence there is an increase in λ_f as well, while λ_f^o characterizes the distance between the elements which remains constant. For the comparison, two sets of cases are tested, one with $\lambda_f^o = 0.06$ and the other with $\lambda_f^o = 0.11$ and the orientation from 0 to $pi/4$. Here it is seen that both methods give almost exactly the

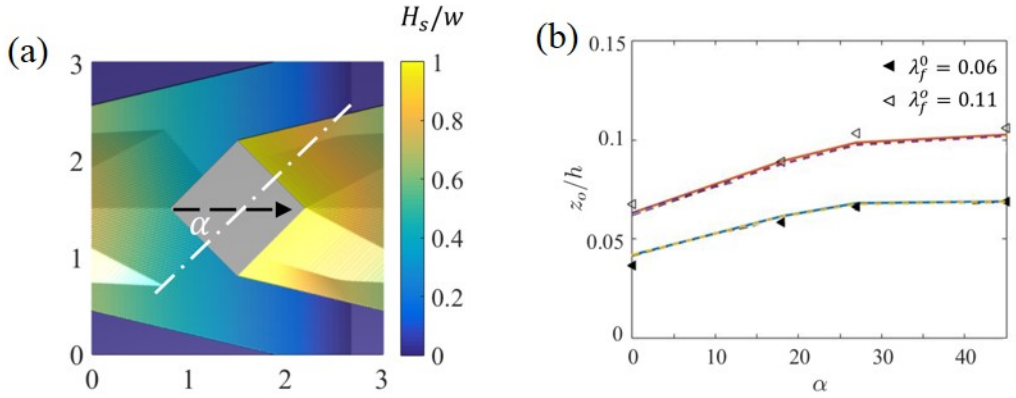

Figure A.11: (a) Top view of an example input surface to the model, with the cubic roughness element at an angle ($\alpha = \pi/4$)to the flow. The associated height of the sheltering volume is also shown. (b) Model comparisons against LES for roughness element orientation. The points are LES from Ref 142, the solid lines are the A_s method while the dashed lines are the h_s method. α is plotted in degrees.

same result and both also matches the LES results[142] very well (Fig. A.11a).

Thus it can be concluded that the full integration approach as well as the equivalent height approach works well for cuboidal geometries and both provide results that are consistent with published results in the literature. However, the full integration approach is advantageous since it can be used for more complex roughness elements, and this is done in the following sections – first to rough surfaces created by arrangements of LEGO blocks[32] and then to arrays of idealized biofouled surfaces from Chapter 3.

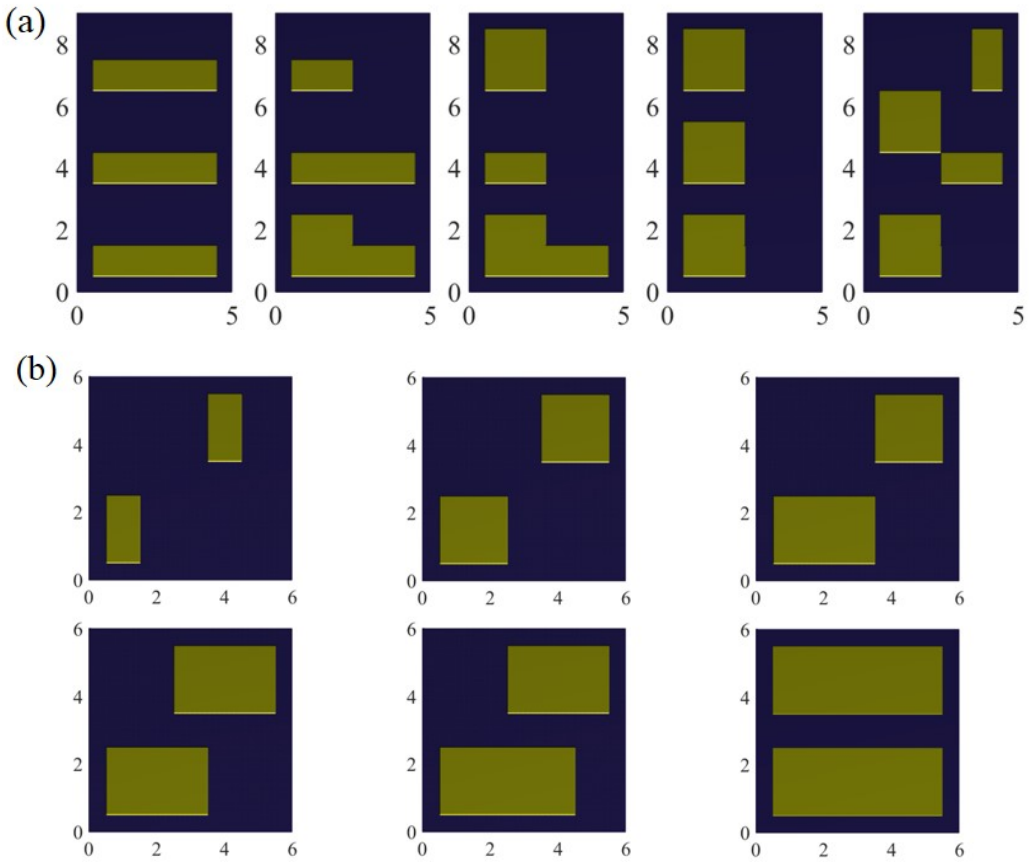

Figure A.12: LEGO block arrangement for (a)CASELF and (b) CASELP. The flow is from left to right.

A.4 LEGO Block Roughened Surfaces

In this section the generalized model predictions are compared against the experimental results[32] for various LEGO roughened surfaces. The geometry and arrangement are obtained from the Placidi and Ganapatisubramani.[32] They carried out experiments on two sets of arrangements – the first one where the λ_p was fixed and the λ_f was varied (CASELF – Fig. A.12a) and the other one with a fixed λ_f and a varying λ_p (CASELP – Fig. A.12b). The corresponding values of λ_f and λ_p are given in

Table A.1: The two sets of cases for the LEGO blocks from Placidi and Ganapatisubramani.[32] CASELF has a constant $\lambda_p = 0.27$ and CASELP has constant $\lambda_f = 0.15$.

CASELF	
Case	λ_f
LF1	0.09
LF2	0.12
LF3	0.15
LF4	0.18
LF5	0.21
LF6	0.24

CASELP	
	λ_p
LP1	0.11
LP2	0.22
LP3	0.27
LP4	0.33
LP5	0.39
LP6	0.56

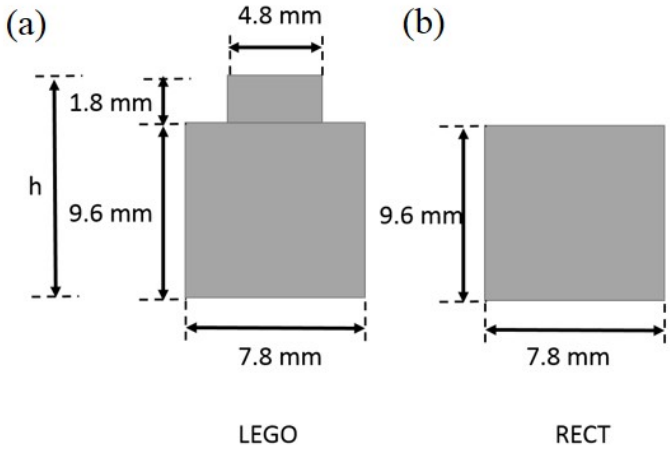

Figure A.13: The details of the geometry used (a)The LEGO block and (b) RECT geometry obtained by removing the top protrusion from (a).

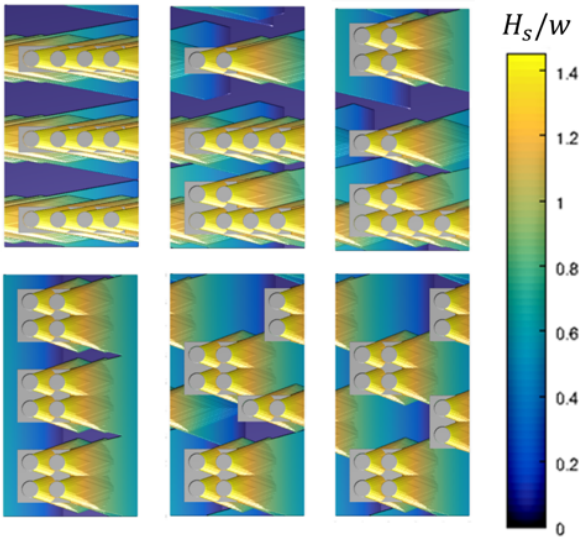

Figure A.14: The model predicted sheltering volume for the CASELF illustrated using contours of the height of the sheltering volume.

Table A.1. The λ_f is the nominal value for each arrangement calculated based on the area of a projection of one LEGO block. It should also be noted that the case geometries are based on the geometries presented in Ref 32, and there is a difference in λ_p for the last case in LPCASE where λ_p as calculated is 0.56 which is used here, in lieu of 0.44 as used in Ref 32. In the analysis two types of elements are used– the full LEGO block (LEGO – Fig. A.13a) and the LEGO block with the protruding cylinder removed (RECT – Fig. A.13b). For the model $Nx = Ny = 200$ is chosen after a convergence study to see that the predicted z_o and d do not vary much. The values for δ/h is fixed as 11 which is the average value from the experiments[32] and $C_d = 1$ and $C_{DH} = 0.7$ which are the same value used for cubes.

Figures A.14 and A.15 illustrate the sheltering predicted by the model for the LEGO block using a top view and the contours of the height of the sheltered volume.

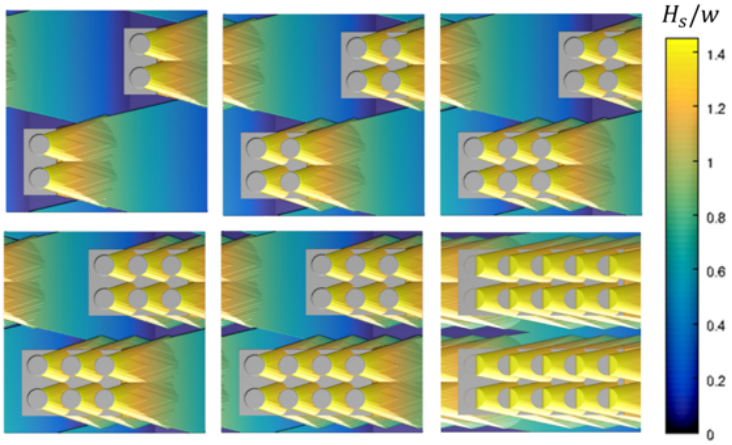

Figure A.15: The model predicted sheltering volume for the CASELP illustrated using contours of the height of the sheltering volume.

It can be seen that the sheltering volume is fairly complex and would have been difficult to do analytically even for the RECT element. For the LEGO block the protrusions at the top do seem to be sheltered heavily since they are quite close to each other.

Fig. A.16a,b shows the comparison of z_o and d for the CASELF runs. The x axis is the case number and z_o and d are all non-dimensionalized with the LEGO block height h. A fairly good match is obtained between the experimental measurements and the model predictions for both LEGO and RECT geometries. It is seen that the z_o increases and d decreases as the frontal area increases. The rectangular block has a lower d/h since the values are non-dimensionalized with the full LEGO height. From Fig. A.16c it is seen that the friction velocity is also predicted well. For u_τ calculations a value of $\Pi = 0.5$ is used which is O(1). Changing the value of Π gives a similar trend but will shift the value of u_τ up or down. One thing to note here is

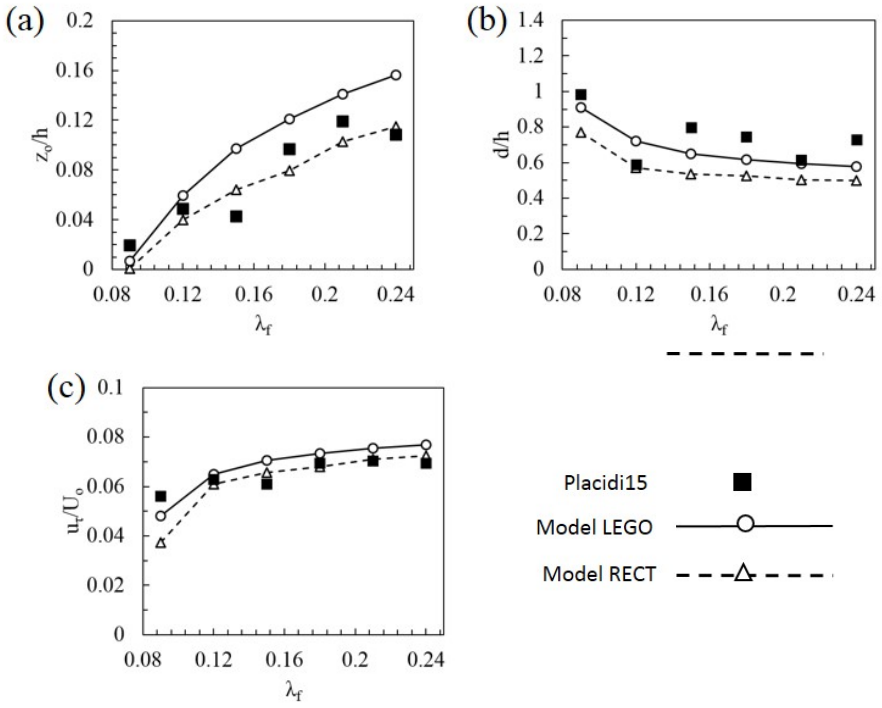

Figure A.16: Comparison of (a) z_o (b) d and (c) u_τ for CASELF arrangements.

that the model uses a value of $\kappa = 0.4$, while the experimental fit was done using a κ of 0.38 but this should not change the trends that is observed. For CASELP (Fig. A.17) it is seen that the trends are still predicted correctly, although there is some difference in the values of z_o and d from the model and the experiment. The value of d in the experimental data does seem somewhat high especially for the 3^{rd} arrangement $\lambda_p = 0.27$. The u_τ values also match fairly well between the experiments and both the LEGO and RECT cases.

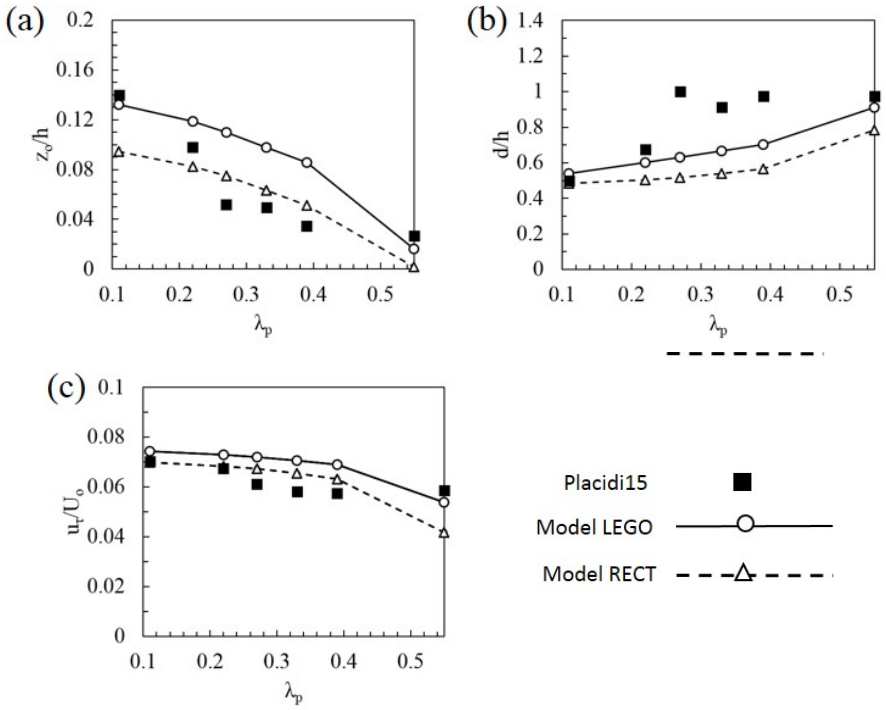

Figure A.17: Comparison of (a) z_o (b) d and (c) u_τ for CASELP arrangements.

A.5 Application to Idealized Biofouled Surfaces

This model provides a way to model the idealized biofouled surfaces in Chapter 3.1. For the model, a value of $C_d = 0.6$ and $C_{DH} = 0.4$ is used. This is lower than the values used for the cuboidal cases and are measured from the LES for the lowest λ_f. This is comparable to a value of 0.52 that is obtained for C_{DH} for the case of an isolated barnacle in the experiments of Schultz et. al.[145] The grid size used for the calculation is $N_x = N_y = 200$ for all the cases. For the LES results the fitting procedure is the same as explained in Sec. 4.4. The corresponding log–law fits are shown in Fig. 3.19 for all the cases. The model results match fairly the trends of the

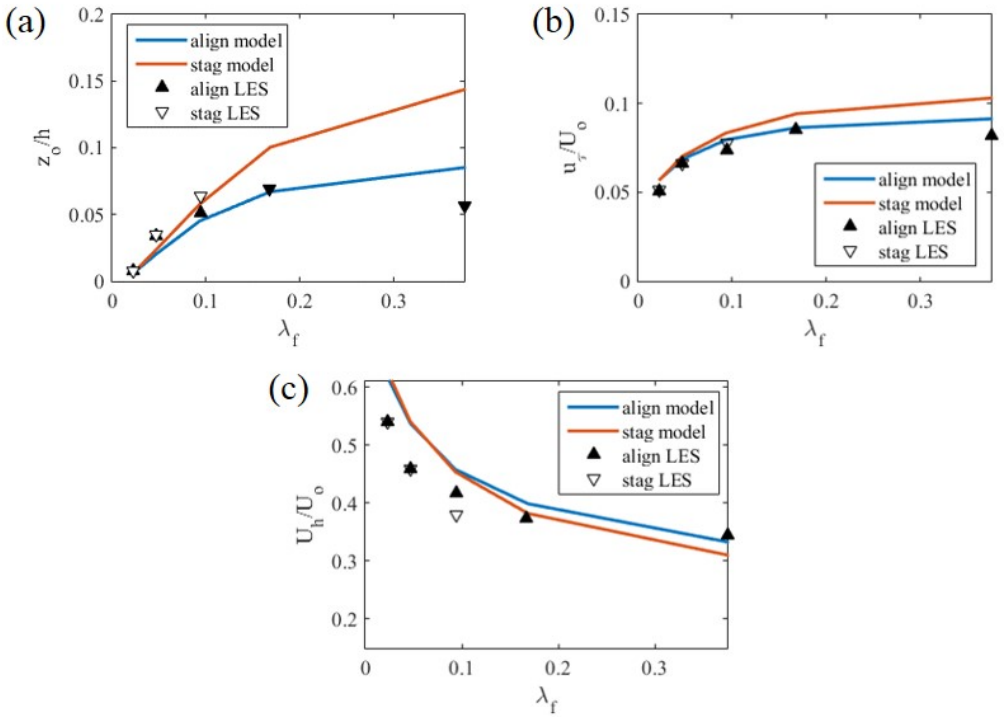

Figure A.18: Comparison of (a) z_o (b) u_τ and (c) U_h for the idealized barnacle fouled surfaces.

LES predictions. One interesting observation is that the model seems to predict that the z_o and u_τ plateau rather than decrease at high values of λ_f, whereas for cubes, a decreasing trend is observed at these values. This indicates the model predicts that the sheltering effects do not overwhelm the additional drag–generation for this geometry. More data are required to either affirm or refute this statement for such surfaces, although the behavior is consistent with the LES simulations for the higher λ_f cases of 0.16 and 0.38. It would be an interesting to test in more detail using cases with different λ_f and for frustums with various diameter ratios.

Figure A.19: The region surrounding the *Sperrstrasse* urban canyon in Basel. The region of interest is highlighted.

A.6 Predicting Drag on Urban Geometries

Next, an example is shown investigating the application of the model to more complex geometry, in this case that of an urban canyon. The data–set used here is the area around *Sperrstrasse* in the city of Basel (Fig A.19). This area has been investigated as part of the Basel Urban Boundary Layer Experiment (BUBBLE)[81] to elucidate various energy and transport processes, and recently has also been subject of a detailed LES study.[83] The data–set is obtained from the Geoportal of the Basel-Stadt Canton `http://www.geo.bs.ch/`. This data–set is in the form of an AutoCAD file which is converted into a height based data–set using a sampling grid. The 512 m^2 area under investigation is shown in Fig A.20 in the form of the building–height contour (This is the same region simulated in the LES[83] as well). The mean height of the buildings

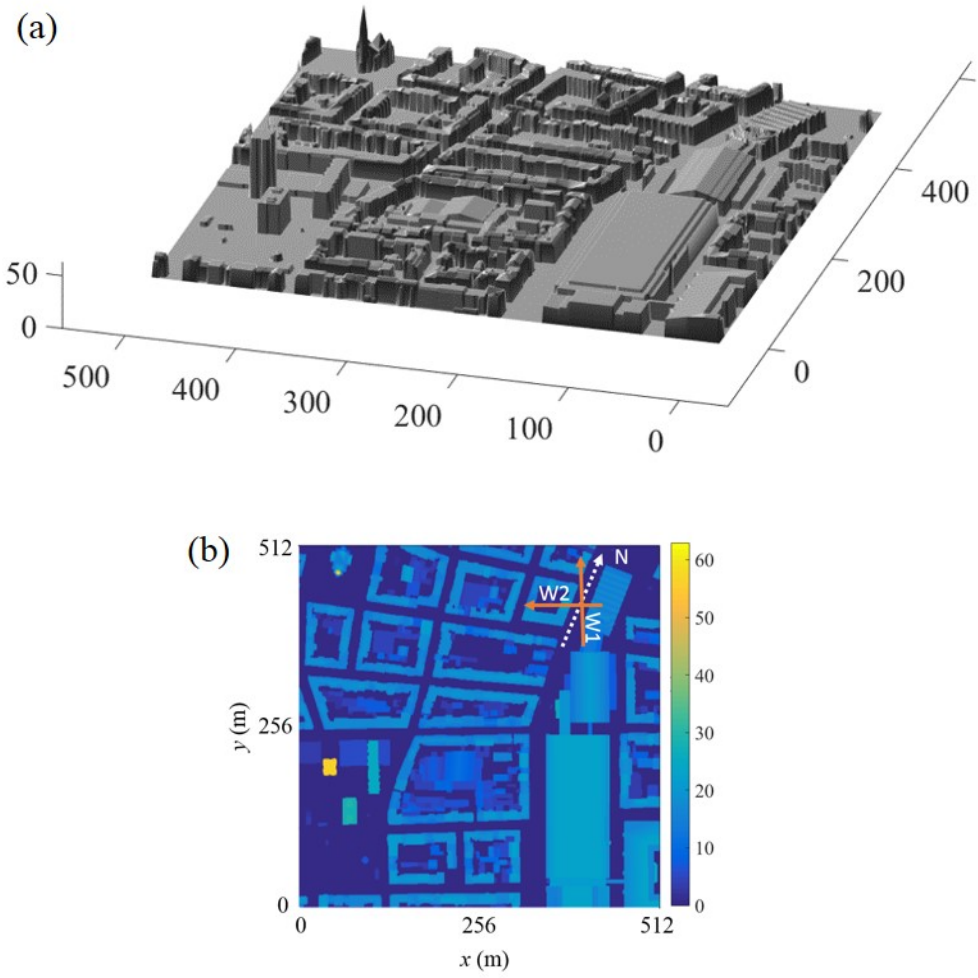

Figure A.20: (a) The converted data–set in the form of $h(x, y)$ which is the input to the shading model. (b) Top view indicating the two wind directions tested – W1 and W2. The coloring is the building height. The grid used has a resolution of 1m in the x and y directions.

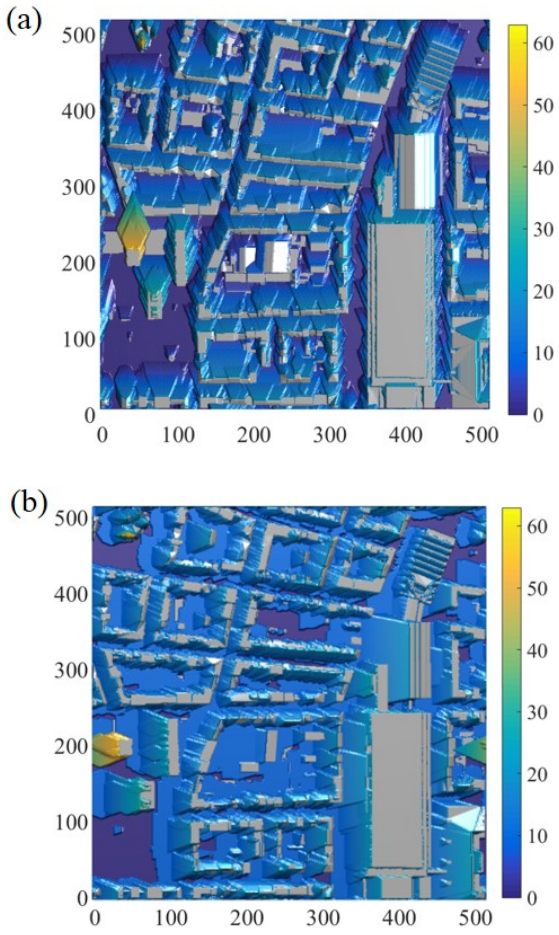

Figure A.21: The predicted shading colored by the height of the shading volume for (a) W1 and (b) W2 directions.

$\bar{h}$ is 15.4m and the variance σ is 6.5m. This data–set is imported into the shading model and two directions of the incoming wind are investigated similar to the LES data–set – W1 and W2 as indicated in Fig. A.20b. The predicted shading is shown in Fig. A.21. The velocity profiles for the LES were provided and were used to calculate the aerodynamic parameters of the wind profile. This was done by using the model predicted d to fit the log–law and obtain the z_o and u_τ. The inlet boundary layer thickness δ and the free stream velocity was matched to the simulation values. The

Table A.2: Comparison of the data from the model to the fitted LES data.

Direction W1			Direction W2		
	z_o(m)	u_τ (m/s)		z_o(m)	u_τ (m/s)
LES	2.67	1.18	LES	2.68	1.13
MODEL	3.86	1.03	MODEL	3.46	0.94

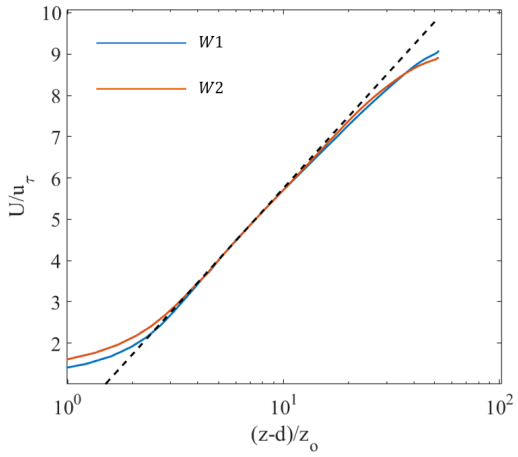

Figure A.22: The LES profiles from Giometto et.al.[83] non-dimensionalized and plotted in log–linear profile using the fitted data.

predicted z_o from the model is compared against the LES data in Table A.2. The corresponding log–law fits are shown in Fig. A.22. Comparing the data in the table, and it can be seen that the drag predicted is very similar although the z_o value for the model seems a bit high.

A.7 Summary

In this Appendix a way to generalize the analytical rough–wall model[63] to more general surfaces is attempted. A general formulation is developed that expresses

the aerodynamic parameters in terms of the height of the input surface $H(x, y)$. Further a methodology is also developed for the shading volume that can work for any general roughness element and reverts to the simpler formulation for the case of cubes and rectangular prism elements. The methodology requires a numerical solution for a general surface, and it is shown that for cubes and rectangular prism roughness elements in various configurations, the predictions match well with the results from literature. This methodology is also applied to two cases – the first case is the LEGO block roughened surfaces.[32] For the CASELF, it is seen that for a fixed λ_p, z_o and d increases as λ_f increases and for the CASELP, z_o decreases and d increases as λ_p is increased keeping λ_f fixed. Next this formulation is applied to arrays of frustums. For the frustums again the trends are predicted correctly and the model seems to predict no decrease in z_o and u_τ at high λ_f for this geometry, which still requires more tests. This method could serve a quick way to predict the aerodynamic parameters for any type of general roughness elements and any type of configuration, although further testing is required. Ultimately, it will be interesting to apply such models to surfaces with more general height distributions[31,79,146] and also to evaluate drag forces for flow over actual urban environments,[82,83] an example of which has been presented here.

Appendix B

Validation of The General Shading Model

In this Appendix the general shading model presented in Appendix A is applied to cuboidal geometries in aligned, staggered and percent stagger configurations. The predictions are compared against the analytical model predictions and also the LES results from Chapter 4 and from Yang and Meneveau.[142] Since the analytical model uses the "equivalent h_s" approach, in this section the same approach is followed, i.e. Eq. A.12, to obtain a one to one comparison.

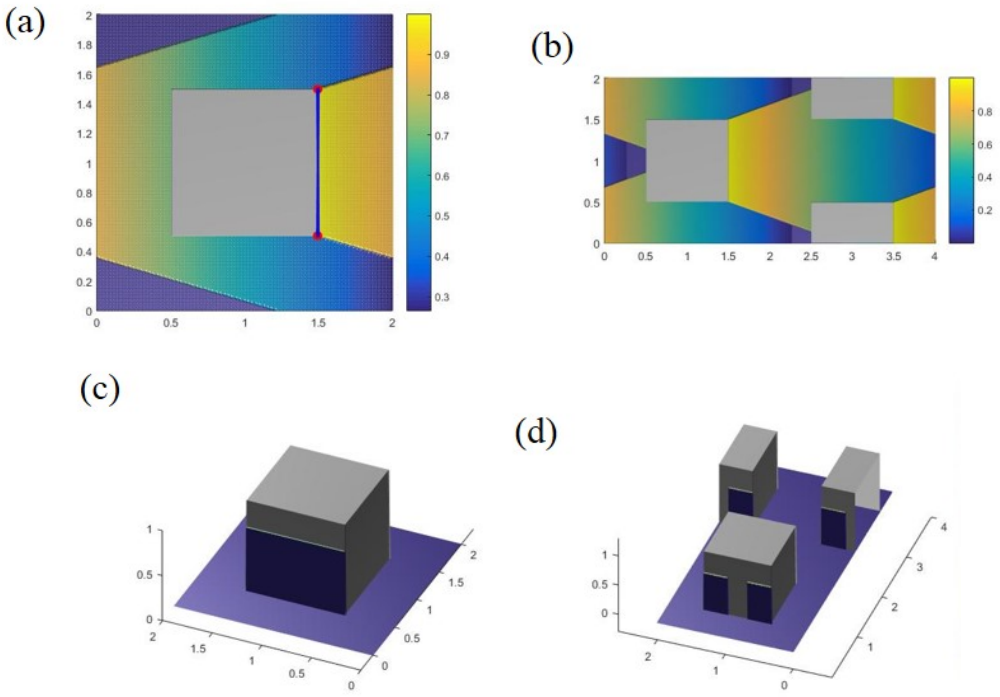

Figure B.1: The top view showing the sheltering region for (a) an aligned and (b) staggered arrangement. The colors indicate the height of the sheltering region. (c) and (d) shows the corresponding sheltered area on the cubes.

B.1 Aligned and Staggered Cubes

The first case tested is cubic roughness elements in an aligned arrangement for various values of λ_f. Example input surfaces are shown in Fig A.7a,b for the case of $\lambda_f = 0.25$ aligned and staggered arrangements. Note that the code assumes periodic boundary conditions in the streamwise and spanwise direction, and thus only the repeating tile need be specified. The volumetric sheltering for the two cases are shown in Fig B.1a,b, and the the predicted sheltered area is shown in Fig B.1c,d. For the aligned case the edge from where the sheltering region is generated is also shown. Note that the shaded

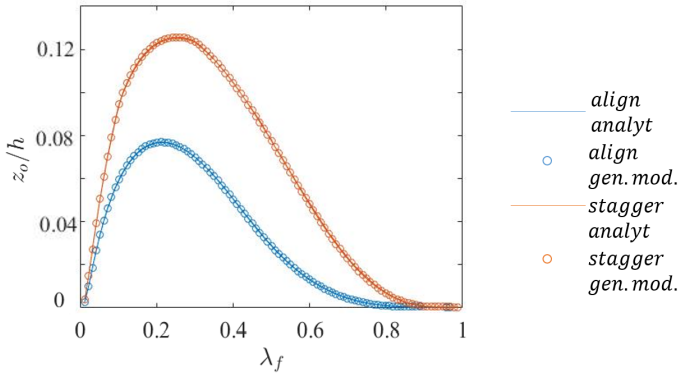

Figure B.2: z_o prediction for aligned and staggered cubes compared between the analytical model and the general shading model.

area in Fig. B.1d is converted into an "equivalent height" to calculate the attenuation coefficient. The results are shown in Fig. B.2, and a very good match is obtained between the two approaches for both aligned and staggered arrangements. The cases are run at intervals of λ_f of 0.01, and a very fine resolution of $N_x = N_y = 1024$ is used for the aligned and $N_x = 2048$ is used for the staggered case. This resolution is used for all the cases in this appendix. In practice such a high resolution is not required, and using an order magnitude lower resolution still gives good results. This is tested by picking a case of aligned cubes of $\lambda_f = 0.25$ and testing the effect of varying the resolution from a coarse resolution of 64×64 to a very fine resolution of 1024×1024. Table B.1 shows the results for both the geometric and aerodynamic properties. The result for the analytical model are shown as well. As expected, a decreasing trend in the error is seen as the mesh size is increased for all the quantities – λ_f, λ_p, z_o, d, u_τ and U_h. The time for the computation increases almost linearly with $N = N_x \times N_y$ (Fig. B.3). To compare the performance at different levels,

Table B.1: Comparison of results on various grids for the case of an aligned cubes with $\lambda_f = 0.25$.

N	λ_f	λ_p	z_o/h	d/h	u_τ/U_o	U_h/U_o	$t_s(s)$
64	0.1053	0.1008	0.0620	0.6344	0.1439	0.6394	0.1143
128	0.1097	0.1094	0.0634	0.6363	0.1452	0.6352	0.2437
256	0.1093	0.1085	0.0627	0.6373	0.1447	0.6360	0.9168
512	0.1103	0.1107	0.0631	0.6379	0.1450	0.6350	4.7464
1024	0.1102	0.1105	0.0629	0.6381	0.1449	0.6352	20.7179
Analytical	0.1100	0.1100	0.0628	0.6381	0.1452	0.6357	–

Table B.2: The differences between the aerodynamic parameters calculated at each grid with the result from an analytical calculation.

N	$\Delta z_o/z_o^c$	$\Delta d/d^c$	$\Delta u_\tau/u_\tau^a$	$\Delta U_h/U_h^a$
64	0.0123	0.0057	0.0088	0.0058
128	0.0103	0.0028	0.0004	0.0008
256	0.0008	0.0011	0.0030	0.0004
512	0.0041	0.0003	0.0010	0.0011
1024	0.0013	0.0001	0.0018	0.0008

the difference of the predicted aerodynamic properties from the analytical value are shown in Table B.2. The percentage difference from the analytical value is around 1% or less for all the parameters for all the cases and not much is gained by going for very high resolutions compared to the trade-off in cost. Thus for getting quick estimates of the aerodynamic properties of the surface a coarse resolution works well. For these validation cases a high resolution is used to match the analytical result as closely as possible.

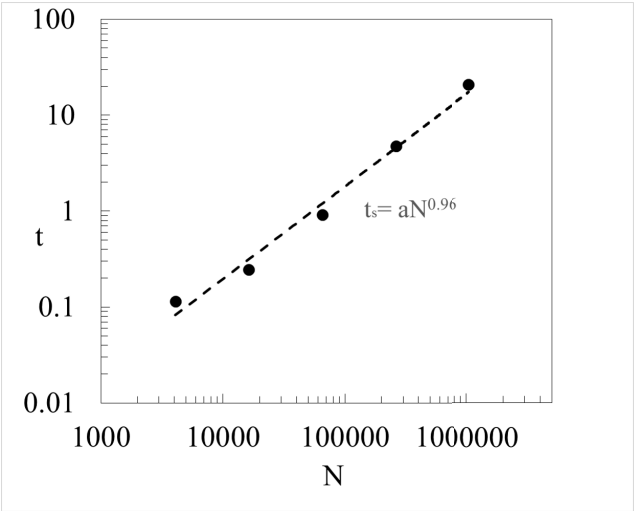

Figure B.3: Variation of the computation time as a function of the grid size N plotted on a log–log scale.

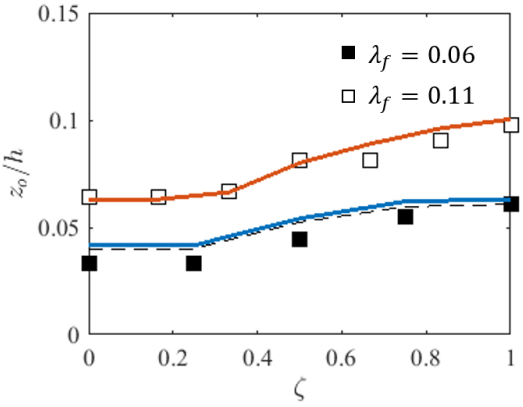

Figure B.4: Comparison of z_o for a percent stagger arrangement of cubes for predictions from the generalized model (solid lines), the analytical model (dashed lines) and the LES (points).

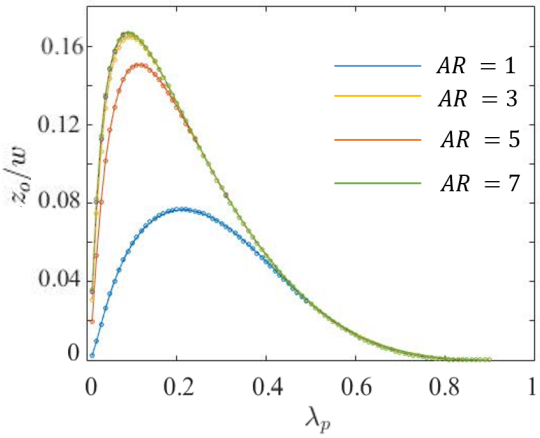

Figure B.5: The predicted z_o for aligned arrangement of rectangular–prisms at various aspect–ratios compared between the generalized model (points) and the analytical version (solid lines).

B.2 Percent Stagger Arrangement of Cubes

Next, the case of a percent stagger arrangement of cubes is compared against LES results.[142] Two values of λ_f are chosen – 0.06 and 0.11. The results are given in Fig. B.4, and it can be seen that the model matches well the data from LES as well as the predictions from the analytical model

B.3 Rectangular Prism – Aligned, Staggered and Percent Stagger Arrangements

Next the general shading model will be tested for rectangular–prism elements at various aspect–ratios and arrangements. First a comparison between the generalized

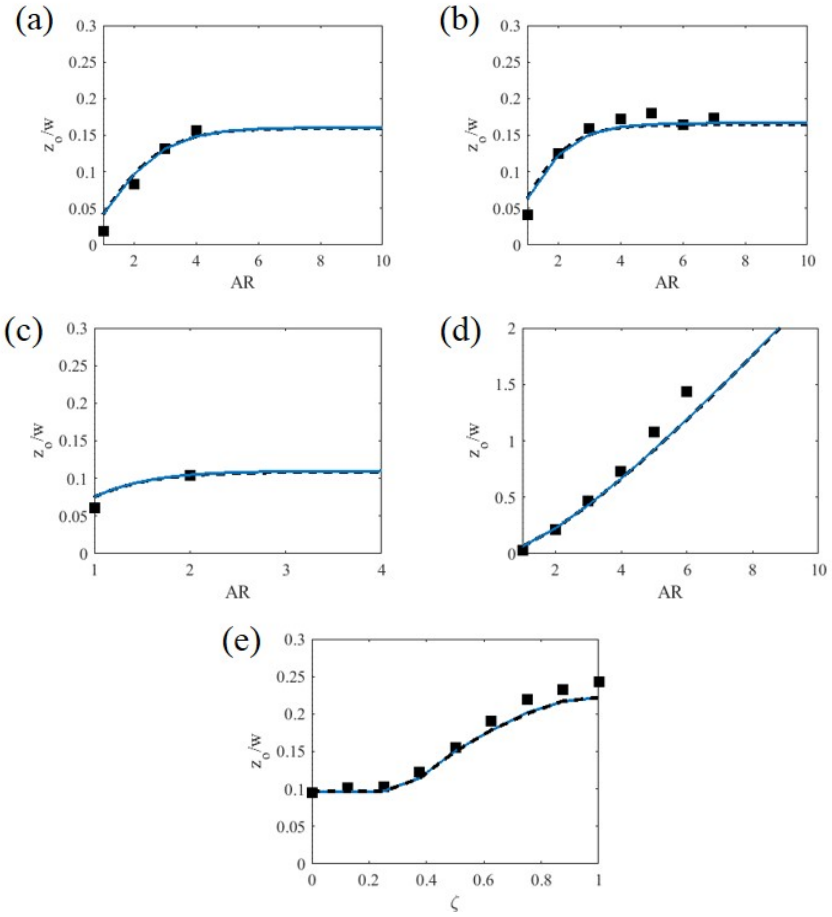

Figure B.6: The predicted z_o for two values of λ_f with various values of percent stagger the five sets of cases from Chapter 4. The points are LES results while the solid lines are the predictions from the generalized shading model and the dashed lines those from the analytical model.

model and the analytical version is presented in Fig. B.5 for an aligned arrangement of cubes for various aspect–ratios for λ_p from 0.01 to 0.9. It can be seen that they match very well for all the aspect ratios.

Following this, the cases from Chapter 4 are replicated for the five sets of cases - three aligned sets of cases at $\lambda_p = 0.06, 0.11, 0.25$ and various aspect–ratios, a staggered set at $\lambda_p = 0.06$ and various aspect ratios, and finally a percent stagger set

of cases at $\lambda_p = 0.06$ and $AR = 2$. The results are shown in Fig. B.6 and again a very good match is found between the analytical formulation and the generalized model. Thus it can be seen that the numerical solution procedure outline in Appendix A matches the analytical result for the various canonical cuboidal surfaces.

Appendix C

Derivation of Geometric Parameters for a Staggered Arrangement

For a fully staggered arrangement the sheltering volume behind an element is as shown in Fig C.1a–c. The sheltered region on a cube in such an arrangement is shown in Fig C.2. The sheltered region consists of the two contributions – (1) a region of height h_{s1} and width $2w_s$ generated via spanwise sheltering and (2) a region of height h_{s2} and width w generated via streamwise sheltering. There is an overlap of the two regions, and it leads to the shape as shown which has a total area

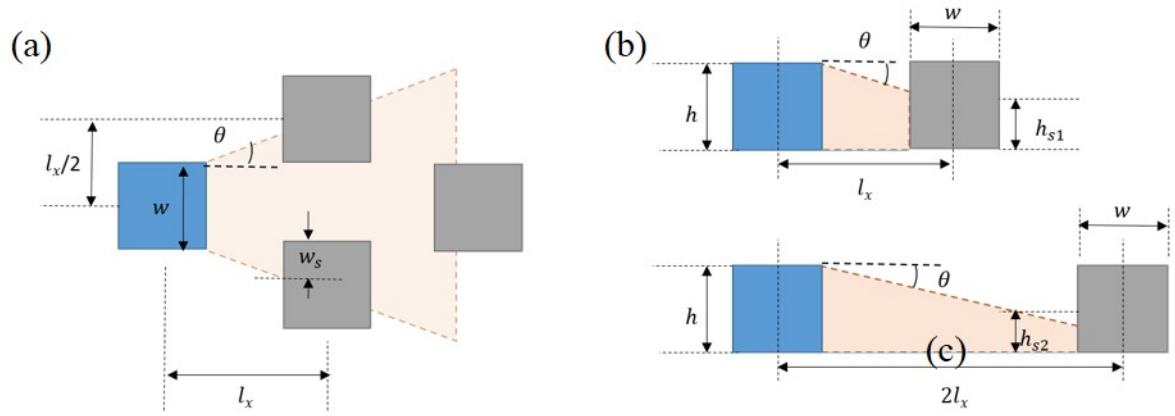

Figure C.1: Streamwise and spanwise sheltering for a staggered arrangement. (a) Top view of spanwise and streamwise sheltering (b) side view of spanwise sheltering and (c) side view of streamwise sheltering.

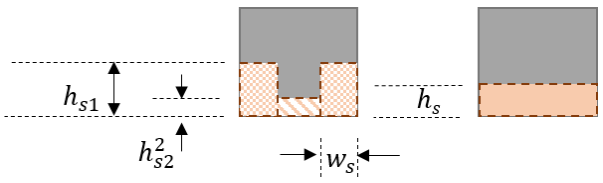

Figure C.2: Sheltered region on a cube in staggered arrangement and conversion into an equivalent 1D shaded height h_s.

$$A_s = h_{s2}w + 2(h_{s1} - h_{s2})w_{sm} = h_s w \tag{C.1}$$

with $w_{sm} = \min(w_s, w/2)$. This sheltered area is converted into an equivalent region of height h_s as shown in Fig. C.2 where

$$\begin{aligned} h_s &= A_s/w \\ h_s &= h_{s2} + 2(h_{s1} - h_{s2})w_{sm}/w. \end{aligned} \tag{C.2}$$

APPENDIX C. DERIVATION OF GEOMETRIC PARAMETERS FOR A STAGGERED ARRANGEMENT

Note that depending on the actual shape of the sheltered region h_{s1}, h_{s2}, w_s etc. could turn out to be zero. h_{s2} is zero at low and moderate values of λ_f ($\lesssim 0.3$) where the elements are far enough apart that the streamwise sheltering is not active. At even lower values of λ_f ($\lesssim 0.1$) the side sheltering is also not active i.e. w_s is zero. The h_s thus calculated from Eq. C.2 is used in the model for predicting the attenuation coefficient a[63]

$$a = \frac{a_o}{1 - h_s/h}. \tag{C.3}$$

This can be expressed in a similar fashion to the representation in Sec. 5.1 as

$$\begin{aligned} a &= \frac{a_o}{C_\zeta^{st}\left(\frac{1}{\sqrt{\lambda_f}} - 1\right)\tan\theta} \\ C_\zeta^{st} &= \frac{1 - \frac{h_s}{h}}{\left(\frac{1}{\sqrt{\lambda_f}} - 1\right)\tan\theta} \end{aligned} \tag{C.4}$$

where $C(\zeta = 1) = C_\zeta^{st}$ encodes the information regarding the relative arrangement for a fully staggered arrangement. If a similar approach in Sec 5.2.1 is followed, Eq. C.4 can be written as

$$\begin{aligned} a(1 - \exp(-2a)) &= K_a \\ K_a &= \frac{2a_o^2}{\left(C_\zeta^{st}\right)^2 C_d \left(1 - \sqrt{\lambda_f}\right)^2}. \end{aligned} \tag{C.5}$$

APPENDIX C. DERIVATION OF GEOMETRIC PARAMETERS FOR A STAGGERED ARRANGEMENT

To estimate C_ζ^{st}, consider the behavior in the limits of $\lambda_f = 0$ and 1. In the limit $\lambda_f \to 0$ it can be seen that

$$\begin{aligned} C_\zeta^{st} &= \frac{1 - \dfrac{h_s}{h}}{\left(\dfrac{1}{\sqrt{\lambda_f}} - 1\right)\tan\theta}; \qquad \tan\theta \sim \sqrt{\lambda_f} \\ C_\zeta^{st} &\to \frac{1}{1 - \sqrt{\lambda_f}} = 1 \quad as\ \lambda_f \to 0. \end{aligned} \tag{C.6}$$

The numerator becomes equal to 1 as $h_s \to 0$, and denominator scales as $(1 - \sqrt{\lambda_f})$ which implies $C_\zeta \to 1$ as $\lambda_f \to 0$. Now consider the high λ_f limit when $\lambda_f \to 1$. Here, even though both numerator and denominator approach 0 a limit can still be found. The expression for h_s in this limit can be obtained by using Eq. C.2. The sheltered heights and widths can be expressed in terms of the geometry and the sheltering angle θ as

$$\begin{aligned} h_{s1} &= h - (l_x - h)\tan\theta; & h_{s1} &= h\left[1 - \left(\frac{1}{\sqrt{\lambda_f}} - 1\right)\tan\theta\right] \\ h_{s2} &= h - (2l_x - h)\tan\theta; & h_{s2} &= h\left[1 - \left(\frac{2}{\sqrt{\lambda_f}} - 1\right)\tan\theta\right] \\ 2w_s &= h + (2\tan\theta - 1)(l_x - h); & 2w_s &= h\left[1 + (2\tan\theta - 1)\left(\frac{1}{\sqrt{\lambda_f}} - 1\right)\right]. \end{aligned} \tag{C.7}$$

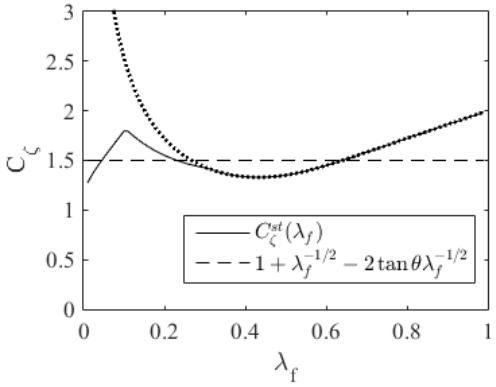

Figure C.3: C_ζ^{st} as a function of λ_f for the staggered arrangement. Also shown in the analytical form derived for the high λ_f case.

From Eq. C.7 the unsheltered height can be expressed as

$$\begin{aligned} 1-\frac{h_s}{h} &= -1+\frac{2}{\sqrt{\lambda_f}}-\frac{1}{\sqrt{\lambda_f}}\left[1+(2\tan\theta-1)\left(\frac{1}{\sqrt{\lambda_f}}-1\right)\right] \\ &= \left[1+\frac{1}{\sqrt{\lambda_f}}-\frac{2\tan\theta}{\sqrt{\lambda_f}}\right]\left[\frac{1}{\sqrt{\lambda_f}}-1\right]. \end{aligned} \tag{C.8}$$

This gives an expression of C_ζ^{st} in the form

$$C_\zeta^{st}=\left[1+\frac{1}{\sqrt{\lambda_f}}-\frac{2\tan\theta}{\sqrt{\lambda_f}}\right]\to 2 \tag{C.9}$$

as $\lambda_f \to 1$ and $\tan\theta \to 0$. Thus C_ζ^{st} is a function of λ_f and has values of 1 and 2 at the limits of low and high λ_f respectively. The value at a λ_f depends on the ratio of u_τ to U_h which is unknown and would have to be solved iteratively. But since the variation in C_ζ^{st} is not large, a value in between, i.e. $C_\zeta^{st}=1.5$ is chosen. The validity of this is checked by a by a post-hoc calculation of the "correct" C_ζ^{st} for different values of λ_f. The results are shown in Fig. C.3 along with the derived expression for high λ_f. It

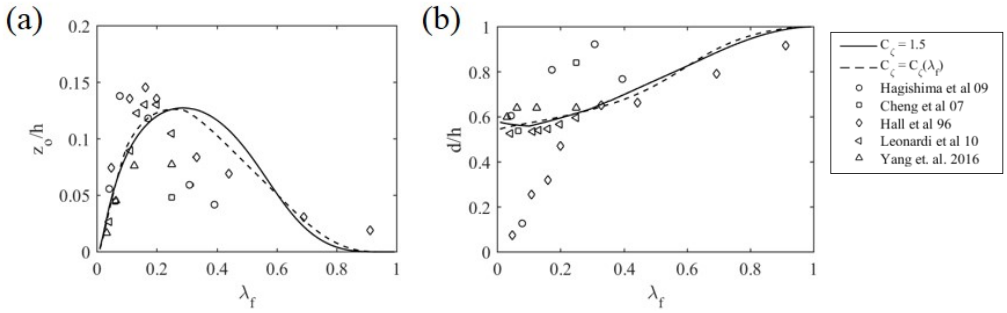

Figure C.4: (a) z_o and (b) d compared for the case of staggered arrangement using a constant C_ζ^{st} and a C_ζ^{st} that varies as a function of λ_f. They are also compared against experimental and simulation results from literature.

can be seen that the C_ζ^{st} does indeed lie in between 1 and 2 and that this $C_\zeta^{st}(\lambda_f)$ is approximated fairly well by the value of 1.5. The mean value of C_ζ^{st} thus calculated is also close to 1.5, and the standard deviation is around 0.2. Using a constant value of C_ζ^{st} gives a fair prediction of z_o and d for the data from the literature and also compares well against the prediction using a varying C_ζ^{st} (Fig. C.4). Hence picking a value of $C_\zeta^{st} = 1.5$ for the whole range is justified and works well.

Appendix D

A Techno–Economic Analysis of Biofouling

As discussed in Sec. 1.2, biofouling has a significant impact on the economics of naval operations. An important aspect of this is to predict optimal remediation strategies – for example the frequency of cleaning of ship hulls that has undergone fouling. Currently, for the US Navy, the cleaning is carried out when the coverage density is 20 %.[65] Leveraging the phenomenological model, a very simple analysis can be performed on the economics of biofouling. Note that this is an exploratory attempt with many assumptions, but still points to the usefulness of a predictive model and also the framework that could be the basis of more detailed analysis.

The first step in the analysis is to find the cost function associated with biofouling.

The growth of biofouling layer leads to an increase in the drag on the surface leading to an increase in the fuel cost given by

$$\begin{aligned} C_F &= (FP)(SFC)\int_0^{T_i} \frac{1}{2}\rho C_D(t) U_{op}^3 A_{hull} \\ &= (FP)(SFC) A_{hull} U_{op}^3 \int_0^{T_i} \frac{1}{2} \left(\frac{u_\tau}{U_{op}}\right)^2 dt \end{aligned} \tag{D.1}$$

where FP is the price of the fuel per KG, SFC is the specific fuel consumption, ρ is the sea–water density, A_{hull} is the hull wetted area and U_{op} is the operating speed of the ship. T_i is the cleaning interval, when the ship is taken in and the hull cleaned. Thus C_F is the total increased fuel cost within one cleaning interval.

Each cleaning of the hull has a cost C_c associated with it. This cost includes both the direct cost of hull cleaning C_h and the lost utilization cost C_U due to the ship being idle. Thus the total operating cost during an operating time t where the ship is cleaned N_c times is

$$\begin{aligned} C_T &= N_c(C_F + C_C) = \frac{t}{T_i}\left(C_F + C_c\right) \\ &= \frac{t}{T_i}\left[C_c + (FP)(SFC)\rho A_{hull} U_{op}^3 \int_0^{T_i} \left(\frac{u_\tau}{U_{op}}\right)^2 dt\right]. \end{aligned} \tag{D.2}$$

Thus the optimal cleaning time T_o is the cleaning time T_i which minimizes C_T

Table D.1: Parameters for the DDG–51 class destroyer.

U_{op} (m/s)	$A_{hull}(m^2)$	SFC (g/KWh)	FP USD/Kg	C_h (USD)	C_U (USD)
8.5	3000	250	1.25	30000	480000

which is given by

$$\begin{aligned} \frac{\partial C_T}{\partial T_i}\Big]_{T_i=T_o} &= 0 \implies \\ T_o &= \frac{C_c + \rho A_{hull}(FP)(SFC)U_{op}^3 \int_0^{T_o} \left(\frac{u_\tau}{U_{op}}\right)^2 dt}{\rho A_{hull}(FP)(SFC)U_{op}^3 \left(\frac{u_\tau(t=T_o)}{U_{op}}\right)^2} \end{aligned} \tag{D.3}$$

This equation can be solved for the optimal time T_o if information about the variation of u_τ as a function of time is known. This is related to the coverage density of the biofouled surface and how the coverage grows with time. As an illustration assume that the growth is linear and increases to 40% solidity in 3 years. Another example would be to use a logistic growth curve instead of the linear curve. These growth curves are shown in Fig. D.1 and provide $\lambda_f(t)$ as a function of time. For relating λ_f to the drag, the model in Chapter 5 is used. Note that the model is valid only for cubes, but it is used to serve as simple stand–in and should give reasonable estimates, since as was seen in Sec. A.5, the values for cubes and frustums are not too dissimilar. For calculating the drag, the staggered case is chosen as it more closely mimics a random arrangement. This gives the prediction of u_τ as a function of time which can be fed into Eq. D.3. To apply this to a real–world example, the DDG–51

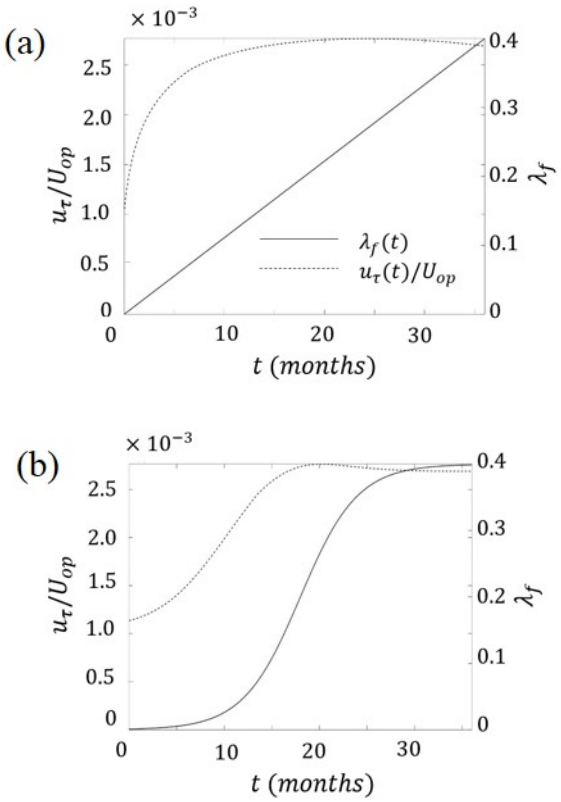

Figure D.1: The assumed growth of biofouling on the ship hull as (a) linear and (b) logistic curve and the associated drag increase on the surface.

class destroyer (Fig. D.2) is used, whose values for the operating parameters are obtained readily from Schultz et. al.[65] and are given in Table D.1. The utilization cost is estimated using the cost of each ship (1 Billion USD), the estimated operational life of the ship (40 years) and the time for a hull cleaning (1 week) , which gives,

$$C_U = \frac{1 \times 10^9}{40 \times 52} \times 1 \approx 480000 USD. \tag{D.4}$$

Figure D.2: The DDG–51 class destroyer of the US Navy (`http://www.navy.mil/management/photodb/photos/030313-N-0115R-077.jpg`)

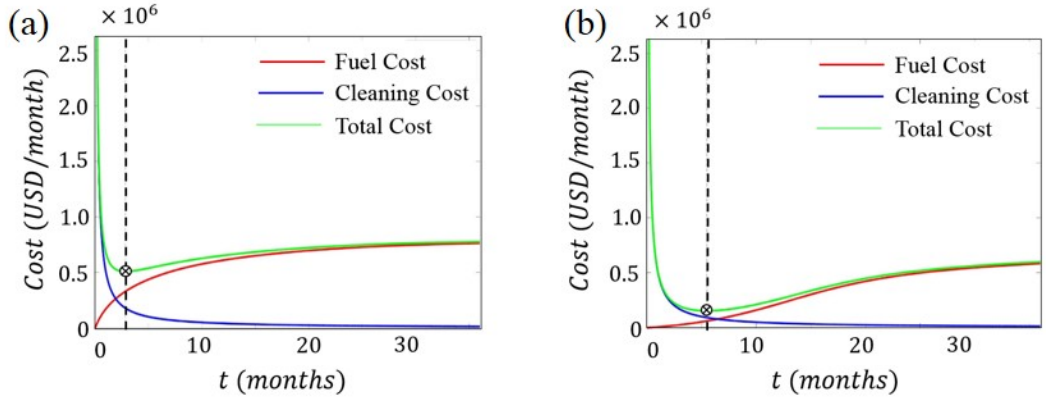

Figure D.3: The costs of biofouling and the optimal cleaning time predicted by the (a) linear and (b) logistic growth curve.

These values are used in Eq. D.3 to predict the cost as a function of cleaning time (Fig. D.3) for both the linear and logistic growth curve. It is seen that the cost decreases at first, as the cost of cleaning is not enough to offset in the increased drag at those cleaning intervals, but as time increases the cost of biofouling becomes more and more and the optimal point (T_o) is reached where the total cost is minimum. Beyond this point, the cost of biofouling is too high and the cleaning interval is not small enough. For the values chosen, the optimal cleaning interval is 3 months for the

Table D.2: Estimations of the optimal cleaning time for the two type of assumed biofouling growth rates – linear and logistic

Case	λ_f	λ_p	T_o (months)
Linear	0.03	0.06	3
Logistic	0.003	0.006	5.5

linear growth case and 5.5 months for the logistical growth case. The corresponding fouling frontal areas are $\lambda_f \approx 0.03$ for the linear case and 0.006 for the logistical growth case. If it is assumed that $\lambda_P \approx 2\lambda_f$ similar for the frustum case, it predicts the optimal cleaning should be at λ_p values 0.06 and 0.006 respectively. The values are tabulated in Table D.2. This shows that the optimal point is very sensitive to the growth rate, and it should be chosen using the knowledge of the growth history of the biofouling.

This analysis though very idealized illustrates the strength and applicability of simplified roughness models. A more in–depth analysis using the models presented in this thesis as well as more realistic models for the growth rate and the surface geometry could be used to obtain a better estimate for the optimal cleaning point. However, as shown by this analysis choosing the optimal cleaning point as a particular value of the coverage ($\lambda_p = 0.2$), would be suboptimal as the coverage at the optimal cleaning point is a function of the growth rate and roughness topology.

Appendix E

Tabulation of geometric factors

In this section the typical values for the geometric parameters from Chapter 5 are tabulated. First for a given K_a it is shown how the calculated values of K_G changes (Table E.1). The results are shown for the uncorrected, first order and second order corrected versions given by the superscripts 0, 1 and 2 respectively. The result of the calculation via the full iteration is also shown. One important thing to note is that these values should be clipped, that is $K_G = \min(K_G, a_o)$ where a_o is 0.4 for cubes. It is observed that at low values of K_a the different correction options have a big effect, and the second order correction gets a result close to the actual value. At values greater than 2 for K_a the correction term is not important. Next the values of K_G and Λ_F for the case of aligned cubes as a function of λ_f are tabulated (Table E.2). The value of K_G increases monotonically with λ_f indicating increasing sheltering at

higher λ_f. Λ_f initially increases reaches a plateau around 0.3 and then decreases. The values for the staggered case are given in Table E.3 where it is observed that the plateauing happens later around $\lambda_f \approx 0.4$ because of the reduction in sheltering.

Table E.1: K_G as a function of K_a and compared with a from iterative solution. The superscripts denote the order of correction used for G. $K_G < 0.4$ should be clipped to 0.4 when used in calculations.

K_a	K_G^0	K_G^1	K_G^2	K_G^{iter}
0.2000	0.2000	0.6066	0.3173	0.3774
0.2500	0.2500	0.6354	0.3802	0.4321
0.3000	0.3000	0.6649	0.4394	0.4838
0.3500	0.3500	0.6953	0.4956	0.5335
0.4000	0.4000	0.7264	0.5493	0.5817
0.4500	0.4500	0.7583	0.6012	0.6288
0.5000	0.5000	0.7910	0.6515	0.6750
0.5500	0.5500	0.8244	0.7006	0.7205
0.6000	0.6000	0.8586	0.7486	0.7656
0.6500	0.6500	0.8935	0.7959	0.8103
0.7000	0.7000	0.9291	0.8425	0.8547
0.7500	0.7500	0.9654	0.8886	0.8989
0.8000	0.8000	1.0024	0.9343	0.9430
0.8500	0.8500	1.0400	0.9797	0.9871
0.9000	0.9000	1.0782	1.0249	1.0311
0.9500	0.9500	1.1171	1.0699	1.0752
1.0000	1.0000	1.1565	1.1149	1.1193
1.1000	1.1000	1.2371	1.2048	1.2079
1.2000	1.2000	1.3197	1.2948	1.2969
1.3000	1.3000	1.4043	1.3851	1.3866
1.4000	1.4000	1.4906	1.4760	1.4770
1.5000	1.5000	1.5786	1.5674	1.5681
1.6000	1.6000	1.6680	1.6595	1.6600
1.7000	1.7000	1.7587	1.7523	1.7526
1.8000	1.8000	1.8506	1.8458	1.8460
1.9000	1.9000	1.9435	1.9399	1.9401
2.0000	2.0000	2.0373	2.0347	2.0348
2.5000	2.5000	2.5170	2.5164	2.5164
3.0000	3.0000	3.0075	3.0073	3.0073

Table E.2: K_G and Λ_f as a function of λ_f for aligned cubes. $K_G < 0.4$ clipped to 0.4 when used in calculations. These values are calculated assuming a second order form for G.

λ_f	K_a	G	G'	K_G	Λ_f
0.0200	0.4341	1.3474	1.4502	0.5849	0.0236
0.0400	0.5000	1.3030	1.3731	0.6515	0.0447
0.0600	0.5613	1.2676	1.3175	0.7115	0.0640
0.0800	0.6222	1.2370	1.2731	0.7697	0.0816
0.1000	0.6844	1.2098	1.2359	0.8280	0.0977
0.1200	0.7491	1.1851	1.2040	0.8877	0.1123
0.1400	0.8170	1.1625	1.1760	0.9498	0.1253
0.1600	0.8889	1.1417	1.1512	1.0149	0.1369
0.1800	0.9654	1.1227	1.1292	1.0838	0.1471
0.2000	1.0472	1.1052	1.1096	1.1573	0.1557
0.2200	1.1351	1.0892	1.0921	1.2363	0.1629
0.2400	1.2298	1.0747	1.0766	1.3217	0.1687
0.2600	1.3322	1.0616	1.0628	1.4144	0.1730
0.2800	1.4434	1.0500	1.0507	1.5156	0.1758
0.3000	1.5644	1.0398	1.0402	1.6267	0.1773
0.3200	1.6965	1.0310	1.0312	1.7490	0.1774
0.3400	1.8411	1.0235	1.0236	1.8844	0.1763
0.3600	2.0000	1.0173	1.0174	2.0347	0.1739
0.3800	2.1751	1.0124	1.0124	2.2020	0.1705
0.4000	2.3688	1.0085	1.0085	2.3889	0.1660
0.4200	2.5837	1.0056	1.0056	2.5981	0.1608
0.4400	2.8231	1.0035	1.0035	2.8329	0.1548
0.4600	3.0908	1.0020	1.0020	3.0971	0.1482
0.4800	3.3913	1.0011	1.0011	3.3951	0.1412
0.5000	3.7302	1.0006	1.0006	3.7323	0.1339
0.5200	4.1142	1.0003	1.0003	4.1153	0.1263
0.5400	4.5515	1.0001	1.0001	4.5520	0.1186
0.5600	5.0523	1.0000	1.0000	5.0525	0.1108
0.5800	5.6293	1.0000	1.0000	5.6294	0.1030
0.6000	6.2984	1.0000	1.0000	6.2984	0.0953

Table E.3: K_G and Λ_f as a function of λ_f for staggered cubes. $K_G < 0.4$ clipped to 0.4 when used in calculations. These values are calculated assuming a second order form for G.

λ_f	K_a	G	G'	K_G	Λ_f
0.0200	0.2171	1.5630	1.8160	0.4000	0.0275
0.0400	0.2500	1.5210	1.8160	0.4000	0.0551
0.0600	0.2807	1.4855	1.7680	0.4169	0.0814
0.0800	0.3111	1.4533	1.6803	0.4521	0.1053
0.1000	0.3422	1.4231	1.6066	0.4870	0.1278
0.1200	0.3745	1.3943	1.5429	0.5222	0.1489
0.1400	0.4085	1.3667	1.4868	0.5583	0.1687
0.1600	0.4444	1.3399	1.4366	0.5955	0.1870
0.1800	0.4827	1.3140	1.3913	0.6342	0.2040
0.2000	0.5236	1.2888	1.3502	0.6748	0.2195
0.2200	0.5675	1.2643	1.3125	0.7175	0.2336
0.2400	0.6149	1.2405	1.2780	0.7628	0.2462
0.2600	0.6661	1.2174	1.2461	0.8110	0.2573
0.2800	0.7217	1.1951	1.2168	0.8625	0.2668
0.3000	0.7822	1.1737	1.1897	0.9180	0.2747
0.3200	0.8482	1.1531	1.1647	0.9781	0.2809
0.3400	0.9205	1.1335	1.1417	1.0434	0.2854
0.3600	1.0000	1.1149	1.1205	1.1149	0.2882
0.3800	1.0876	1.0975	1.1012	1.1936	0.2891
0.4000	1.1844	1.0813	1.0837	1.2807	0.2882
0.4200	1.2919	1.0665	1.0679	1.3778	0.2855
0.4400	1.4116	1.0531	1.0539	1.4865	0.2809
0.4600	1.5454	1.0413	1.0417	1.6092	0.2744
0.4800	1.6956	1.0310	1.0312	1.7483	0.2662
0.5000	1.8651	1.0225	1.0226	1.9070	0.2564
0.5200	2.0571	1.0155	1.0156	2.0890	0.2451
0.5400	2.2758	1.0102	1.0102	2.2989	0.2325
0.5600	2.5262	1.0062	1.0062	2.5419	0.2189
0.5800	2.8147	1.0035	1.0035	2.8246	0.2046
0.6000	3.1492	1.0018	1.0018	3.1549	0.1898

Bibliography

[1] V. Lucey, "Mechanism of pitting corrosion of copper in supply waters," *British Corrosion Journal*, vol. 2, no. 5, pp. 175–185, 1967.

[2] M. Edwards, J. F. Ferguson, and S. H. Reiber, "The pitting corrosion of copper," *Journal of the American Water Works Association;(United States)*, vol. 86, no. 7, 1994.

[3] A. Karimi and J. Martin, "Cavitation erosion of materials," *International Metals Reviews*, vol. 31, no. 1, pp. 1–26, 1986.

[4] S. Li, *Cavitation of hydraulic machinery*. World Scientific, 2000, vol. 1.

[5] A. Redfield, L. Hutchins, E. Deevy, J. Ayers, H. Turner, F. Laidlaw, J. Ferry, and D. Todd, "Marine fouling and its prevention," *US Naval Inst., Annapolis, Md*, vol. 388, 1952.

[6] E. R. Holm, "Barnacles and biofouling," *Integrative and Comparative Biology*, vol. 52, no. 3, pp. 348–355, 2012.

[7] W. P. Kustas and W. Brutsaert, "Wind profile constants in a neutral atmospheric boundary layer over complex terrain," *Boundary-Layer Meteorology*, vol. 34, no. 1-2, pp. 35–54, 1986.

[8] J. D. Albertson and M. B. Parlange, "Surface length scales and shear stress: Implications for land-atmosphere interaction over complex terrain," Tech. Rep., 1999.

[9] J. Finnigan, "Turbulence in plant canopies," *Annual Review of Fluid Mechanics*, vol. 32, no. 1, pp. 519–571, 2000.

[10] C. S. B. Grimmond and T. R. Oke, "Aerodynamic properties of urban areas derived from analysis of surface form," *Journal of Applied Meteorology*, vol. 38, no. 9, pp. 1262–1292, 1999.

[11] "A halved condenser brass tube pattern with corrosion pittings." *Wikimedia Commons, (CC BY-SA 3.0)*, 2006.

[12] "Cavitation damage evident on the propeller of a personal watercraft." *Wikimedia Commons, (CC BY-SA 3.0)*, 2006.

[13] "Water turbine from the agoyan hydroelectric plant eroded by volcanic ash laden water." *Wikimedia Commons, (CC BY-SA 3.0)*, 2012.

[14] "Kaheawa wind power, maui," *Wikimedia Commons, (CC BY-SA 3.0)*, 2012.

[15] "A night time panorama of Baltimore's inner harbor." *Wikimedia Commons*, 2008.

[16] J. Nikuradse, "Laws of flow in rough pipes," *NACA Technical Memorandum*, vol. 1292, 1933.

[17] H. Schlichting, "Experimental investigation of the problem of surface roughness," *NACA Technical Memorandum*, vol. 823, 1937.

[18] M. Raupach, R. Antonia, and S. Rajagopalan, "Rough-wall turbulent boundary layers," *Applied Mechanics Review*, vol. 44, no. 1, pp. 1–25, 1991.

[19] J. Jiménez, "Turbulent flows over rough walls," *Annual Review of Fluid Mechanics*, vol. 36, no. 1, pp. 173–196, 2004.

[20] M. Schultz and K. Flack, "The rough-wall turbulent boundary layer from the hydraulically smooth to the fully rough regime," *Journal of Fluid Mechanics*, vol. 580, pp. 381–405, 2007.

[21] I. Marusic, B. McKeon, P. Monkewitz, H. Nagib, A. Smits, and K. Sreenivasan, "Wall-bounded turbulent flows at high Reynolds numbers: Recent advances and key issues," *Physics of Fluids (1994-present)*, vol. 22, no. 6, p. 065103, 2010.

[22] P. Jackson, "On the displacement height in the logarithmic velocity profile," *Journal of Fluid Mechanics*, vol. 111, pp. 15–25, 1981.

[23] D. Coles, "The law of the wake in the turbulent boundary layer," *Journal of Fluid Mechanics*, vol. 1, no. 02, pp. 191–226, 1956.

[24] H. Cheng and I. P. Castro, "Near-wall flow development after a step change in surface roughness," *Boundary-Layer Meteorology*, vol. 105, no. 3, pp. 411–432, 2002.

[25] H. Cheng, P. Hayden, A. Robins, and I. Castro, "Flow over cube arrays of different packing densities," *Journal of Wind Engineering and Industrial Aerodynamics*, vol. 95, no. 8, pp. 715–740, 2007.

[26] S. Leonardi and I. P. Castro, "Channel flow over large cube roughness: a direct numerical simulation study," *Journal of Fluid Mechanics*, vol. 651, pp. 519–539, 2010.

[27] J. Claus, O. Coceal, T. Thomas, S. Branford, S. Belcher, and I. Castro, "Wind-direction effects on urban-type flows," *Boundary-Layer Meteorology*, vol. 142, no. 2, pp. 265–287, 2012.

[28] W. Anderson, Q. Li, and E. Bou-Zeid, "Numerical simulation of flow over urban-like topographies and evaluation of turbulence temporal attributes," *Journal of Turbulence*, vol. 16, no. 9, pp. 809–831, 2015.

[29] W.-C. Cheng and F. Porté-Agel, "Adjustment of turbulent boundary-layer flow

to idealized urban surfaces: A large-eddy simulation study," *Boundary-Layer Meteorology*, vol. 155, no. 2, pp. 249–270, 2015.

[30] D. Hall, R. Macdonald, and S. Walker, *Measurements of dispersion within simulated urban arrays: a small scale wind tunnel study.* Building Research Establishment, 1996.

[31] A. Hagishima, J. Tanimoto, K. Nagayama, and S. Meno, "Aerodynamic parameters of regular arrays of rectangular blocks with various geometries," *Boundary-Layer Meteorology*, vol. 132, no. 2, pp. 315–337, 2009.

[32] M. Placidi and B. Ganapathisubramani, "Effects of frontal and plan solidities on aerodynamic parameters and the roughness sublayer in turbulent boundary layers," *Journal of Fluid Mechanics*, vol. 782, pp. 541–566, 2015.

[33] C. F. Colebrook, "Turbulent flow in pipes, with particular reference to the transition region between the smooth and rough pipe laws." *Journal of the Institution of Civil Engineers*, vol. 11, no. 4, pp. 133–156, 1939.

[34] L. F. Moody, "Friction factors for pipe flow," *Trans. ASME*, vol. 66, no. 8, pp. 671–684, 1944.

[35] J. P. Bons, "A review of surface roughness effects in gas turbines," *Journal of Turbomachinery*, vol. 132, no. 2, pp. 041 203–041 203–10, 2010.

[36] C.-H. Moeng, "A large-eddy-simulation model for the study of planetary

boundary-layer turbulence," *Journal of Atmospheric Sciences*, vol. 41, no. 13, pp. 2052–2062, 1984.

[37] U. Piomelli and E. Balaras, "Wall-layer models for large-eddy simulations," *Annual Review of Fluid Mechanics*, vol. 34, no. 1, pp. 349–374, 2002.

[38] X. I. A. Yang, J. Sadique, R. Mittal, and C. Meneveau, "Integral wall model for large eddy simulations of wall-bounded turbulent flows," *Physics of Fluids*, vol. 27, no. 2, p. 025112, 2015.

[39] P. S. Lissaman, "Energy effectiveness of arbitrary arrays of wind turbines," *Journal of Energy*, vol. 3, no. 6, pp. 323–328, 1979.

[40] S. Frandsen, "On the wind speed reduction in the center of large clusters of wind turbines," *Journal of Wind Engineering and Industrial Aerodynamics*, vol. 39, no. 1, pp. 251–265, 1992.

[41] R. J. Stevens, "Dependence of optimal wind turbine spacing on wind farm length," *Wind energy*, 2015.

[42] K. A. Flack and M. P. Schultz, "Review of hydraulic roughness scales in the fully rough regime," *Journal of Fluids Engineering*, vol. 132, no. 4, p. 041203, 2010.

[43] J. F. Barlow and O. Coceal, "A review of urban roughness sublayer turbulence," *Met. Office Research and Development–Tech. Rep.*, no. 527, 2009.

[44] D. J. Bettermann, "Contribution l'tude de la couche limite turbulente le long de plaques rugueuses juin," *Laboratoire d'Arothermique du CNRS, Rapport 65-6*, 1965.

[45] F. Dvorak, "Calculation of turbulent boundary layers on rough surfaces in pressure gradient." *AIAA Journal*, vol. 7, no. 9, pp. 1752–1759, 1969.

[46] R. L. Simpson, "A generalized correlation of roughness density effects on the turbulent boundary layer." *AIAA Journal*, vol. 11, no. 2, pp. 242–244, 1973.

[47] R. Dirling, "A method for computing roughwall heat transfer rates on reentry nosetips," in *American Institute of Aeronautics and Astronautics, Thermophysics Conference, 8 th, Palm Springs, Calif*, 1973.

[48] A. Sigal and J. E. Danberg, "New correlation of roughness density effect on the turbulent boundary layer," *AIAA Journal*, vol. 28, no. 3, pp. 554–556, 1990.

[49] J. A. Van Rij, B. Belnap, and P. Ligrani, "Analysis and experiments on three-dimensional, irregular surface roughness," *Journal of Fluids Engineering*, vol. 124, no. 3, pp. 671–677, 2002.

[50] H. Lettau, "Note on aerodynamic roughness-parameter estimation on the basis of roughness-element description," *Journal of Applied Meteorology*, vol. 8, no. 5, pp. 828–832, 1969.

[51] J. Counehan, "Wind tunnel determination of the roughness length as a function

of the fetch and the roughness density of three-dimensional roughness elements," *Atmospheric Environment*, vol. 5, no. 8, pp. 637–642, 1971.

[52] R. Macdonald, "Modelling the mean velocity profile in the urban canopy layer," *Boundary-Layer Meteorology*, vol. 97, no. 1, pp. 25–45, 2000.

[53] B.-G. Kim, C. Lee, S. Joo, K.-C. Ryu, S. Kim, D. You, and W.-S. Shim, "Estimation of roughness parameters within sparse urban-like obstacle arrays," *Boundary-Layer Meteorology*, vol. 139, no. 3, pp. 457–485, 2011.

[54] A. Musker, "Universal roughness functions for naturally-occurring surfaces," *Transactions of the Canadian Society for Mechanical Engineering*, vol. 6, no. 1, pp. 1–6, 1980.

[55] E. Napoli, V. Armenio, and M. De Marchis, "The effect of the slope of irregularly distributed roughness elements on turbulent wall-bounded flows," *Journal of Fluid Mechanics*, vol. 613, pp. 385–394, 10 2008.

[56] M. P. Schultz and K. A. Flack, "Turbulent boundary layers on a systematically varied rough wall," *Physics of Fluids*, vol. 21, no. 1, 2009.

[57] R. M. Cionco, "A mathematical model for air flow in a vegetative canopy," *Journal of Applied Meteorology*, vol. 4, no. 4, pp. 517–522, 1965.

[58] O. Coceal and S. Belcher, "A canopy model of mean winds through urban

areas," *Quarterly Journal of the Royal Meteorological Society*, vol. 130, no. 599, pp. 1349–1372, 2004.

[59] F.-s. Lien, E. Yee, and J. D. Wilson, "Numerical modelling of the turbulent flow developing within and over a 3-d building array, part ii: a mathematical foundation for a distributed drag force approach," *Boundary-Layer Meteorology*, vol. 114, no. 2, pp. 245–285, 2005.

[60] S. Di Sabatino, E. Solazzo, P. Paradisi, and R. Britter, "A simple model for spatially-averaged wind profiles within and above an urban canopy," *Boundary-Layer Meteorology*, vol. 127, no. 1, pp. 131–151, 2008.

[61] R. Mittal, H. Dong, M. Bozkurttas, F. Najjar, A. Vargas, and A. von Loebbecke, "A versatile sharp interface immersed boundary method for incompressible flows with complex boundaries," *Journal of Computational Physics*, vol. 227, no. 10, pp. 4825–4852, 2008.

[62] J. H. Seo and R. Mittal, "A sharp-interface immersed boundary method with improved mass conservation and reduced spurious pressure oscillations," *Journal of Computational Physics*, vol. 230, no. 19, pp. 7347–7363, 2011.

[63] X. I. A. Yang, J. Sadique, R. Mittal, and C. Meneveau, "Exponential roughness layer and analytical model for turbulent boundary layer flow over rectangular-prism roughness elements," *Journal of Fluid Mechanics*, vol. 789, pp. 127–165, 2016.

[64] M. P. Schultz, "Effects of coating roughness and biofouling on ship resistance and powering," *Biofouling*, vol. 23, no. 5, pp. 331–341, 2007.

[65] M. Schultz, J. Bendick, E. Holm, and W. Hertel, "Economic impact of biofouling on a naval surface ship," *Biofouling*, vol. 27, no. 1, pp. 87–98, 2011.

[66] D. J. Crisp, "Territorial behaviour in barnacle settlement," *Journal of Experimental Biology*, vol. 38, pp. 429–446, 1961.

[67] ——, "The planktonic stages of the cirripedia balanus balanoides (l.) and balanus balanus (l.) from north temperate waters." *Crustaceans*, vol. 3, pp. 208–221, 1961.

[68] M. G. Hadfield, "The DP Wilson lecture. Research on settlement and metamorphosis of marine invertebrate larvae: past, present and future," *Biofouling*, vol. 12, no. 1-3, pp. 9–29, 1998.

[69] N. Lagersson and J. Høeg, "Settlement behavior and antennulary biomechanics in cypris larvae of balanus amphitrite (crustacea: Thecostraca: Cirripedia)," *Marine Biology*, vol. 141, no. 3, pp. 513–526, 2002.

[70] C. Clarke Murray, T. W. Therriault, and P. T. Martone, "Adapted for invasion? comparing attachment, drag and dislodgment of native and nonindigenous hull fouling species," *Biological Invasions*, vol. 14, no. 8, pp. 1651–1663, 2012.

[71] "Nauplius of elminius modestus." *Wikimedia Commons, (CC BY-SA 3.0)*, 2007.

[72] "photographed near the upper shoreline, lundy island, uk. max shell length about 10mm." *Wikimedia Commons, (CC BY-SA 3.0)*, 2007.

[73] "photographed near the upper shoreline, lundy island, uk. max shell length about 10mm." *Woods Hole OCeanogrphic Institution Archives*, 1943, retrieved online 05/20/2016.

[74] R. Britter and S. Hanna, "Flow and dispersion in urban areas," *Annual Review of Fluid Mechanics*, vol. 35, no. 1, pp. 469–496, 2003.

[75] H. J. S. Fernando, "Fluid dynamics of urban atmospheres in complex terrain," *Annual Review of Fluid Mechanics*, vol. 42, pp. 365–389, 2010.

[76] S. Leonardi, P. Orlandi, R. Smalley, L. Djenidi, and R. Antonia, "Direct numerical simulations of turbulent channel flow with transverse square bars on one wall," *Journal of Fluid Mechanics*, vol. 491, pp. 229–238, 2003.

[77] C.-H. Liu, M. C. Barth, and D. Y. Leung, "Large-eddy simulation of flow and pollutant transport in street canyons of different building-height-to-street-width ratios," *Journal of Applied Meteorology*, vol. 43, no. 10, pp. 1410–1424, 2004.

[78] F. Lien, E. Yee, and Y. Cheng, "Simulation of mean flow and turbulence over a 2d building array using high-resolution CFD and a distributed drag force approach," *Journal of Wind Engineering and Industrial Aerodynamics*, vol. 92, no. 2, pp. 117–158, 2004.

[79] S. A. Zaki, A. Hagishima, J. Tanimoto, and N. Ikegaya, "Aerodynamic parameters of urban building arrays with random geometries," *Boundary-Layer Meteorology*, vol. 138, no. 1, pp. 99–120, 2011.

[80] P. Kastner-Klein and M. W. Rotach, "Mean flow and turbulence characteristics in an urban roughness sublayer," *Boundary-Layer Meteorology*, vol. 111, no. 1, pp. 55–84, 2004.

[81] W. M. Rotach, R. Vogt, C. Bernhofer, E. Batchvarova, A. Christen, A. Clappier, B. Feddersen, S.-E. Gryning, G. Martucci, H. Mayer, V. Mitev, R. T. Oke, E. Parlow, H. Richner, M. Roth, Y.-A. Roulet, D. Ruffieux, A. J. Salmond, M. Schatzmann, and A. J. Voogt, "BUBBLE – an urban boundary layer meteorology project," *Theoretical and Applied Climatology*, vol. 81, no. 3, pp. 231–261, 2005.

[82] M. Kanda, A. Inagaki, T. Miyamoto, M. Gryschka, and S. Raasch, "A new aerodynamic parametrization for real urban surfaces," *Boundary-Layer Meteorology*, vol. 148, no. 2, pp. 357–377, 2013.

[83] M. Giometto, A. Christen, C. Meneveau, J. Fang, M. Krafczyk, and M. Parlange, "Spatial characteristics of roughness sublayer mean flow and turbulence over a realistic urban surface," *Boundary-Layer Meteorology*, pp. 1–28, 2016.

[84] C. Letchford, D. Lander, P. Case, A. Dyson, and M. Amitay, "Bio-mimicry inspired tall buildings: The response of cactus-like buildings to wind action at

Reynolds number of 10^4," *Journal of Wind Engineering and Industrial Aerodynamics*, vol. 150, pp. 22 – 30, 2016.

[85] Y. Shao and Y. Yang, "A scheme for drag partition over rough surfaces," *Atmospheric Environment*, vol. 39, no. 38, pp. 7351 – 7361, 2005.

[86] J. T. Millward-Hopkins, A. S. Tomlin, L. Ma, D. Ingham, and M. Pourkashanian, "Estimating aerodynamic parameters of urban-like surfaces with heterogeneous building heights," *Boundary-Layer Meteorology*, vol. 141, no. 3, pp. 443–465, 2011. [Online]. Available: http://dx.doi.org/10.1007/s10546-011-9640-2

[87] T. Oke, "Street design and urban canopy layer climate," *Energy and Buildings*, vol. 11, no. 13, pp. 103 – 113, 1988.

[88] J. H. Lee, H. J. Sung, and P.-Å. Krogstad, "Direct numerical simulation of the turbulent boundary layer over a cube-roughened wall," *Journal of Fluid Mechanics*, vol. 669, pp. 397–431, 2011.

[89] Z. Xie and I. P. Castro, "LES and RANS for turbulent flow over arrays of wall-mounted obstacles," *Flow, Turbulence and Combustion*, vol. 76, no. 3, pp. 291–312, 2006.

[90] J. Yuan and U. Piomelli, "Estimation and prediction of the roughness function on realistic surfaces," *Journal of Turbulence*, vol. 15, no. 6, pp. 350–365, 2014.

[91] D. R. Chapman, "Computational aerodynamics development and outlook," *AIAA J.*, vol. 17, no. 12, pp. 1293–1313, 1979. [Online]. Available: www.scopus.com

[92] U. Piomelli, "Wall-layer models for large-eddy simulations," *Progress in Aerospace Sciences*, vol. 44, no. 6, pp. 437–446, 2008.

[93] X. I. A. Yang and C. Meneveau, "Recycling inflow method for simulations of spatially evolving turbulent boundary layers over rough surfaces," *Journal of Turbulence*, vol. 17, no. 1, pp. 75–93, 2016.

[94] J. Smagorinsky, "General circulation experiments with the primitive equations: I. the basic experiment*," *Monthly weather review*, vol. 91, no. 3, pp. 99–164, 1963.

[95] M. Germano, U. Piomelli, P. Moin, and W. H. Cabot, "A dynamic subgrid-scale eddy viscosity model," *Physics of Fluids A: Fluid Dynamics (1989-1993)*, vol. 3, no. 7, pp. 1760–1765, 1991.

[96] D. K. Lilly, "A proposed modification of the Germano subgrid-scale closure method," *Physics of Fluids A: Fluid Dynamics (1989-1993)*, vol. 4, no. 3, pp. 633–635, 1992.

[97] C. Meneveau, T. S. Lund, and W. H. Cabot, "A lagrangian dynamic subgrid-

scale model of turbulence," *Journal of Fluid Mechanics*, vol. 319, pp. 353–385, 1996.

[98] A. Vreman, "An eddy-viscosity subgrid-scale model for turbulent shear flow: Algebraic theory and applications," *Physics of Fluids*, vol. 16, no. 10, pp. 3670–3681, 2004.

[99] D. You and P. Moin, "A dynamic global-coefficient subgrid-scale eddy-viscosity model for large-eddy simulation in complex geometries," *Physics of Fluids*, vol. 19, no. 6, p. 065110, 2007.

[100] Y. Zang, R. L. Street, and J. R. Koseff, "A non-staggered grid, fractional step method for time-dependent incompressible Navier-Stokes equations in curvilinear coordinates," *Journal of Computational Physics*, vol. 114, no. 1, pp. 18–33, 1994.

[101] R. Mittal and G. Iaccarino, "Immersed boundary methods," *Annu. Rev. Fluid Mech.*, vol. 37, pp. 239–261, 2005.

[102] T. S. Lund, X. Wu, and K. D. Squires, "Generation of turbulent inflow data for spatially-developing boundary layer simulations," *Journal of Computational Physics*, vol. 140, no. 2, pp. 233–258, 1998.

[103] L. Zheng, T. L. Hedrick, and R. Mittal, "A multi-fidelity modelling approach

for evaluation and optimization of wing stroke aerodynamics in flapping flight," *Journal of Fluid Mechanics*, vol. 721, pp. 118–154, 2013.

[104] V. Vedula, S. Fortini, J. Seo, G. Querzoli, and R. Mittal, "Computational modeling and validation of intraventricular flow in a simple model of the left ventricle," *Theoretical Computational Fluid Dynamics*, vol. 28, no. 6, pp. 589–604, 2014.

[105] E. Meinders and K. Hanjalić, "Vortex structure and heat transfer in turbulent flow over a wall-mounted matrix of cubes," *International Journal of Heat and Fluid Flow*, vol. 20, no. 3, pp. 255–267, 1999.

[106] J. Sadique, X. I. A. Yang, C. Meneveau, and R. Mittal, "Simulation of boundary layer flows over biofouled surfaces," in *22nd AIAA Computational Fluid Dynamics Conference*. American Institute of Aeronautics and Astronautics, 2015, p. 2616.

[107] B. McKeon, J. Li, W. Jiang, J. Morrison, and A. Smits, "Further observations on the mean velocity distribution in fully developed pipe flow," *Journal of Fluid Mechanics*, vol. 501, pp. 135–147, 2004.

[108] P. A. Monkewitz, K. A. Chauhan, and H. M. Nagib, "Self-consistent high-Reynolds-number asymptotics for zero-pressure-gradient turbulent boundary layers," *Physics of Fluids*, vol. 19, no. 11, p. 115101, 2007.

[109] H. M. Nagib and K. A. Chauhan, "Variations of von Kármán coefficient in canonical flows," *Physics of Fluids*, vol. 20, no. 10, p. 1518, 2008.

[110] R. T. Reynolds and I. P. Castro, "Measurements in an urban-type boundary layer," *Experiments in Fluids*, vol. 45, no. 1, pp. 141–156, 2008.

[111] K. A. Flack, M. P. Schultz, and J. S. Connelly, "Examination of a critical roughness height for outer layer similarity," *Physics of Fluids*, vol. 19, no. 9, 2007.

[112] J. M. Barros, E. K. A. Murphy, and M. P. Schultz, "Particle image velocimetry measurement of flow around barnacles immersed in a turbulent boundary layer," in 11^{th} *International Symposium on Particle Image Velocimetry, Santa Barbara, California*, 2015.

[113] H. Sakamoto and M. Arie, "Vortex shedding from a rectangular prism and a circular cylinder placed vertically in a turbulent boundary layer," *Journal of Fluid Mechanics*, vol. 126, pp. 147–165, 1983.

[114] S. Roh and S. Park, "Vortical flow over the free end surface of a finite circular cylinder mounted on a flat plate," *Experiments in Fluids*, vol. 34, no. 1, pp. 63–67, 2003.

[115] P. Catalano, M. Wang, G. Iaccarino, and P. Moin, "Numerical simulation of

the flow around a circular cylinder at high reynolds numbers," *International Journal of Heat and Fluid Flow*, vol. 24, no. 4, pp. 463–469, 2003.

[116] R. Pattenden, S. Turnock, and X. Zhang, "Measurements of the flow over a low-aspect-ratio cylinder mounted on a ground plane," *Experiments in Fluids*, vol. 39, no. 1, pp. 10–21, 2005.

[117] I. Castro and A. Robins, "The flow around a surface-mounted cube in uniform and turbulent streams," *Journal of Fluid Mechanics*, vol. 79, no. 02, pp. 307–335, 1977.

[118] K. B. Shah and J. H. Ferziger, "A fluid mechanicians view of wind engineering: Large eddy simulation of flow past a cubic obstacle," *Journal of Wind Engineering and Industrial Aerodynamics*, vol. 67, pp. 211–224, 1997.

[119] H. J. Hussein and R. J. Martinuzzi, "Energy balance for turbulent flow around a surface mounted cube placed in a channel," *Physics of Fluids*, vol. 8, no. 3, 1996.

[120] J.-Y. Hwang and K.-S. Yang, "Numerical study of vortical structures around a wall-mounted cubic obstacle in channel flow," *Physics of Fluids*, vol. 16, no. 7, 2004.

[121] M. Acarlar and C. Smith, "A study of hairpin vortices in a laminar boundary

layer. part 1. hairpin vortices generated by a hemisphere protuberance," *Journal of Fluid Mechanics*, vol. 175, pp. 1–41, 1987.

[122] R. Martinuzzi and M. AbuOmar, "Study of the flow around surface-mounted pyramids," *Experiments in fluids*, vol. 34, no. 3, pp. 379–389, 2003.

[123] M. M. AbuOmar and R. J. Martinuzzi, "Vortical structures around a surface-mounted pyramid in a thin boundary layer," *Journal of Wind Engineering and Industrial Aerodynamics*, vol. 96, no. 6, pp. 769–778, 2008.

[124] I. Castro, S. Vosper, M. Paisley, and P. Hayden, "Vortex shedding behind tapered obstacles in neutral & stratified flow," *Dynamics of Atmospheres and Oceans*, vol. 34, no. 2, pp. 145–163, 2001.

[125] T. Okamoto, M. Yagita, and S.-i. Kataoka, "Flow past cone placed on flat plate," *Bulletin of JSME*, vol. 20, no. 141, pp. 329–336, 1977.

[126] H. R. Spivey, "Shell morphometry in barnacles: quantification of shape and shape change in balanus," *Journal of Zoology*, vol. 216, no. 2, pp. 265–294, 1988.

[127] J. Zhou, R. J. Adrian, S. Balachandar, and T. Kendall, "Mechanisms for generating coherent packets of hairpin vortices in channel flow," *Journal of Fluid Mechanics*, vol. 387, pp. 353–396, 1999.

[128] R. L. Simpson, "Junction flows," *Annual Review of Fluid Mechanics*, vol. 33, no. 1, pp. 415–443, 2001.

[129] A. S. Thomas, "The unsteady characteristics of laminar juncture flow," *Physics of Fluids (1958-1988)*, vol. 30, no. 2, pp. 283–285, 1987.

[130] M. R. Visbal, "Structure of laminar juncture flows," *AIAA Journal*, vol. 29, no. 8, pp. 1273–1282, 1991.

[131] P. Klebanoff, W. Cleveland, and K. Tidstrom, "On the evolution of a turbulent boundary layer induced by a three-dimensional roughness element," *Journal of Fluid Mechanics*, vol. 237, pp. 101–187, 1992.

[132] P. S. Iyer and K. Mahesh, "High-speed boundary-layer transition induced by a discrete roughness element," *Journal of Fluid Mechanics*, vol. 729, pp. 524–562, 2013.

[133] J. Hunt, C. Abell, J. Peterka, and H. Woo, "Kinematical studies of the flows around free or surface-mounted obstacles; applying topology to flow visualization," *Journal of Fluid Mechanics*, vol. 86, no. 01, pp. 179–200, 1978.

[134] V. Dousset and A. Pothérat, "Formation mechanism of hairpin vortices in the wake of a truncated square cylinder in a duct," *Journal of Fluid Mechanics*, vol. 653, pp. 519–536, 2010.

[135] A. K. M. F. Hussain and W. C. Reynolds, "The mechanics of an organized

wave in turbulent shear flow," *Journal of Fluid Mechanics*, vol. 41, no. 02, pp. 241–258, 1970.

[136] A. E. Perry, W. H. Schofield, and P. N. Joubert, "Rough wall turbulent boundary layers," *Journal of Fluid Mechanics*, vol. 37, no. 02, pp. 383–413, 1969.

[137] W. Anderson and C. Meneveau, "Dynamic roughness model for large-eddy simulation of turbulent flow over multiscale, fractal-like rough surfaces," *Journal of Fluid Mechanics*, vol. 679, pp. 288–314, 2011.

[138] W. Anderson, P. Passalacqua, F. Porté-Agel, and C. Meneveau, "Large-eddy simulation of atmospheric boundary-layer flow over fluvial-like landscapes using a dynamic roughness model," *Boundary-Layer Meteorology*, vol. 144, no. 2, pp. 263–286, 2012.

[139] J. Yuan and U. Piomelli, "Estimation and prediction of the roughness function on realistic surfaces," *Journal of Turbulence*, vol. 15, no. 6, pp. 350–365, 2014.

[140] D. Chung, L. Chan, M. MacDonald, N. Hutchins, and A. Ooi, "A fast direct numerical simulation method for characterising hydraulic roughness," *Journal of Fluid Mechanics*, vol. 773, pp. 418–431, 2015.

[141] I. Wygnanski, F. Champagne, and B. Marasli, "On the large-scale structures in two-dimensional, small-deficit, turbulent wakes," *Journal of Fluid Mechanics*, vol. 168, pp. 31–71, 1986.

[142] X. I. A. Yang and C. Meneveau, "From rough wall topology to roughness hydrodynamic properties," *to appear in J. Phys. Conf. Ser.*, 2016.

[143] R. Macdonald, R. Griffiths, and D. Hall, "An improved method for the estimation of surface roughness of obstacle arrays," *Atmospheric Environment*, vol. 32, no. 11, pp. 1857–1864, 1998.

[144] F. Cadieux, J. Sadique, X. I. A. Yang, C. Meneveau, and R. Mittal, "Wall-modeled large eddy simulation of laminar separation bubble flows," in *46th AIAA Fluid Dynamics Conference*, 2016, p. 3189.

[145] M. P. Schultz, C. J. Kavanagh, and G. W. Swain, "Hydrodynamic forces on barnacles: Implications on detachment from fouling-release surfaces," *Biofouling*, vol. 13, no. 4, pp. 323–335, 1999.

[146] D. Jiang, W. Jiang, H. Liu, and J. Sun, "Systematic influence of different building spacing, height and layout on mean wind and turbulent characteristics within and over urban building arrays," *Wind Structures*, vol. 11, no. 4, pp. 275–289, 2008.

Vita

Jasim Sadique obtained his Bachelors in Mechanical Engineering from the National Institute of Technology Calicut and his Masters from the Indian Institute of Technology Kanpur. For his Masters research, he worked on large–eddy simulations of leading–edge separation bubble interacting with passing wakes. The aim was to characterize the flow and heat transfer characteristics of rotor–stator interactions in Turbomachinery. Following this, he joined the Department of Mechanical Engineering at the Johns Hopkins University for his PhD, under the guidance of Professor Rajat Mittal and Professor Charles Meneveau. His PhD research focused on understanding and parameterizing the effect of roughness element geometry and arrangement on turbulent boundary layer flows over macro–scale roughness elements. He has expertise in developing and implementing tools for high–fidelity simulations of turbulent flows over complex surfaces. He also has experience in developing simplified flow models that connect the rough wall topology to the surface drag. These tools have been used to study turbulent flows over surfaces of both engineering and geophysical interest.